MALDI IMAGING MASS SPECTROMETRY FOR SMALL MOLECULE QUANTITATION AND EVALUATION FOR MARKERS OF DRUG RESPONSE IN GLIOMAS

By

Sara L. Frappier

Dissertation

Submitted to the Faculty of the

Graduate School of Vanderbilt University

in partial fulfillment of the requirements

for the degree of

DOCTOR OF PHILOSOPHY

In

Chemistry

May, 2011

Nashville, Tennessee

Approved:

Dr. Richard M. Caprioli

Dr. Michael K. Cooper

Dr. Brian O. Bachmann

Dr. Reid C. Thompson

This work is dedicated to those that I call family.
I am nothing without each and every one of you.

“To change the world, Start with one step.” -Dave Matthews

ACKNOWLEDGEMENTS

This work would not have been possible without the financial support of the Vanderbilt University Chemistry Department, and the DOD Advanced Program in Proteomics W81XWH-05-1-0179.

I would like to thank my mentor, Richard Caprioli, for all of his guidance, and support throughout my graduate student career. I had somewhat of a unique path towards the completion of my degree and your patience and understanding allowed me to realize my potential and push through until the end. You have always encouraged me to look ahead with determination and keep the fire inside alive. This is invaluable advice that I will carry with me always in every aspect of life.

To each of my committee members, Michael Cooper, Brian Bachmann and Reid Thompson, thank-you for all of your input and enthusiasm to help progress this project to its successful completion. Each of you has provided me personal and professional guidance that has taught me a great deal and given me an intense desire to continue working in clinical research.

I must also acknowledge the many people I have had the pleasure of working with throughout my studies at Vanderbilt University. Thank-you to all of the past and present members of the Mass Spectrometry Research Center, you have not only been colleagues, you have been friends. I will always be proud to say that I am a member of the "Caprioli Crew" and the times we have shared together will not be forgotten.

To everyone that has become my family here in Nashville, words cannot express how grateful I am that I have each and every one of you in my life; Lindsey Roark, Lori and Blake McConnell, Nick Culton, Amber Wright, JT Meeks, Ashley Schneider and Lacey and Jacob Culton. Through the ups and downs that this journey has taken me on, you have all been there by my side. You have been there to celebrate my victories or hold my hand when things didn't always work out. You have kept me grounded and focused on what is truly important in this life.

To my true family, I am blessed to have you. Mamma and Daddy-O, you have always been an inspiration to me. Your example has shown me what it means to live a full and meaningful life; a life of honesty, dedication, love, hope, happiness and faith. Your endless support has made me into the person that I am today and I will always strive to make you proud. To my brothers, David and Rob, although distance separates us, I know that you always have my back. The comfort of this has helped me more than you could ever know. And to the rest of the army that is the Frappier family, only we can understand what it truly means to be a "Frap" and the overwhelming care and support that is provided from such a blessed and love-filled family. Thank-you to each and every one of you.

TABLE OF CONTENTS

Page

Chapter

Appendix

LIST OF TABLES

Table Page

LIST OF FIGURES

CHAPTER I

BACKGROUND AND OBJECTIVES

Background

Drug Discovery and Development

The driving force behind drug discovery and development is to connect the process of understanding a disease with bringing a safe and effective new treatment to patients. Scientists work to piece together the basic causes and biological intricacies of disease at the level of genes, proteins and cells. Out of this knowledge “targets” emerge which potential new drugs might be able to affect. Researchers work to validate these targets, discover a potential drug to interact with the chosen target, submit the compound through a series of clinical tests for safety and efficacy and gain approval so that the new drug can get into the hands of doctors and patients. The discovery and development of new medicines is a long, complicated process and takes an average of 10-15 years.[1, 2] The average cost to research and develop each successful drug is estimated to be $800 million to $1 billion.[3] This accounts for the thousands of failures that a company must go through before successfully producing a viable drug compound. For every 5,000- 10,000 compounds that enter the research and development (R&D) pipeline, ultimately only one receives approval. These numbers seem astronomical, but by developing a better understanding of the R&D process which is outlined in Figure 1, one can see why so many compounds don’t make it through the process and why it takes immense resources, the best scientific minds, highly sophisticated technology, interdisciplinary collaboration and complex project management to get one successful drug to patients.

Before any potential new medicine can be investigated, scientists must be able to understand the disease being treated. It is necessary to elucidate the underlying cause of the condition as well as how the genes are altered, how that affects the proteins they encode and how those proteins interact with each other in living cells. These changes directly relate to how the disease affects the patient. This knowledge is the basis for treating the problem and guides research for the discovery of new therapeutic compounds. Researchers from government, academia and industry all contribute to this knowledge base.[4] However, even with new tools and insights, this research takes many years of work and, too often, leads to frustrating dead ends. Thus, there is an ever present need for new technologies and methods to assist in understanding the underlying cause of a disease. Even if the research is successful, it will take many more years of work to turn this basic understanding of what causes a disease into a new treatment.

Once there is enough understanding of a disease, pharmaceutical researchers select a “target” for a potential new medicine. This “target” is usually a gene or protein involved with the disease that can interact with a drug compound. It is then, that large screening processes begin to look for a lead compound. Once a potential compound is identified initial Absorption, Distribution, Metabolism, Excretion and Toxicological (ADME/TOX) studies are performed. The pharmacokinetic and pharmacodynamic (PK/PD) tests are performed both in-vitro and in-vivo in what are known as the pre-clinical trials. The results for these analyses help scientists to understand what the drug does, how it works, as well as any side effects or safety issues.[5]

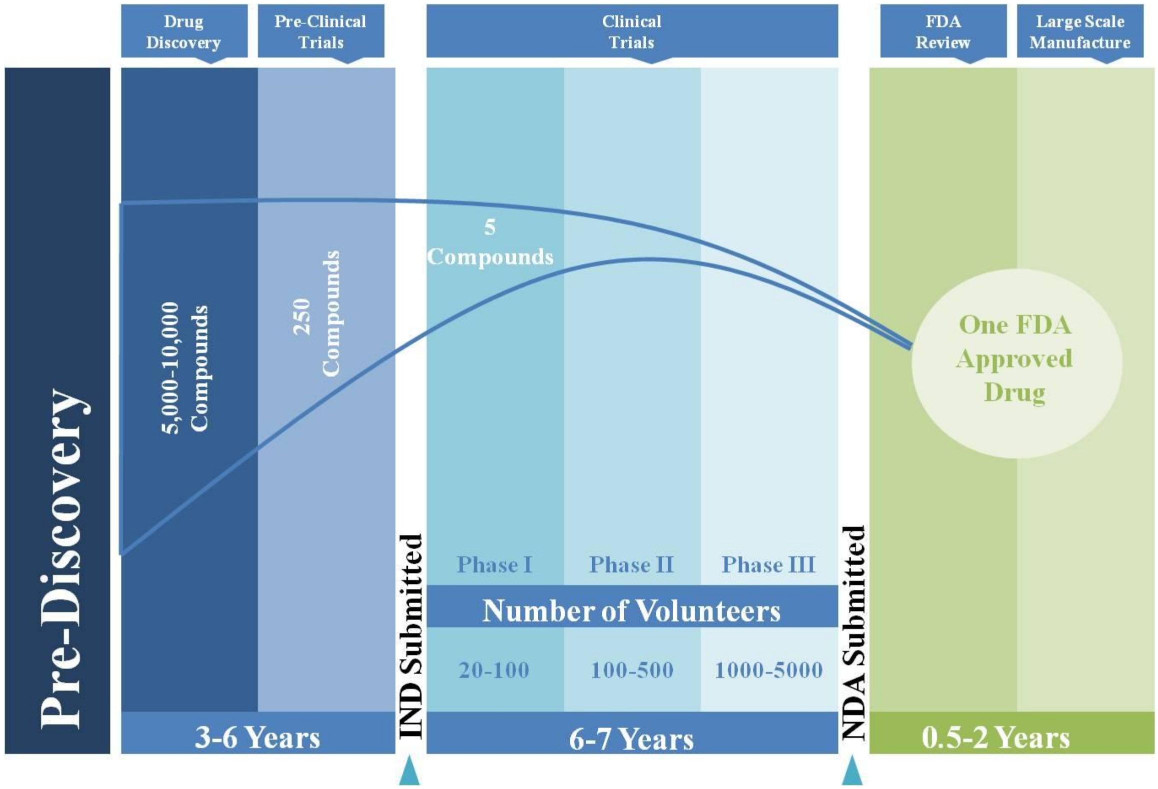

Figure 1: Overview of the drug discovery and development process. It can take upwards of 15 years and over 800 million dollars to develop just one FDA approved drug out of about 10,000 candidates. At all stages of the pre-clinical and clinical trials, advanced technologies, interdisciplinary interactions and cutting edge science are utilized.

After years of work, one to five molecules out of 5,000-10,000 will survive the pre-clinical trial and will be considered for clinical trials. Before a clinical trial can begin, an Investigational New Drug (IND) application is filed with the Food and Drug Administration (FDA). This report describes all the results of the pre-clinical trials, the drug's structure, mechanisms of action in the body and any known side effects. In addition to the IND application, the clinical trials must be approved by the Institutional

Review Board (IRB) and throughout the trials regular reports are monitored and submitted to both the FDA and IRB. [6]

The clinical trials consist of three phases. Phase I is a small initial test performed in 20-100 healthy volunteers to see if the compound is safe for use in humans. The ADME of the drug is studied as well as any side effects that result. Phase II trials focus on testing the effectiveness of the compound on the indicated disease. The trial includes 100-500 patients and evaluates if the drug is targeting the disease as well as establishes both dosing strength and dosing schedule. Phase III trials test a large group of patients to show efficacy and safety. At hundreds of sites across the United States and worldwide, 1,000-5,000 patients are administered the drug and monitored. [3, 7]

After clinical trials, a New Drug Application (NDA), which can be over 100,000 pages long, is filed with the FDA. The document contains all of the PK/PD results from the trials. After approval the drug goes into manufacturing and distribution and ongoing studies are maintained to continue monitoring the drug's performance.[8]

Throughout this long and complex process, one can identify numerous areas where cutting edge technologies, new methods and interdisciplinary collaborations can help to advance the understanding of human biology and disease. This can lead to numerous breakthroughs for developing new medications. Researchers face great challenges in understanding and applying these advances to the treatment of disease, but these possibilities continue to grow as our scientific knowledge expands and becomes increasingly more complete.

Mass Spectrometry (MS) has played a large role in these processes of developing new drugs in all aspects of the drug development process. MS has been used to characterize small molecule compounds, evaluate biomolecules for targets, protein identification, analytical detection and quantitation. It has been used in all stages of pre-clinical and clinical trials and there is room for growth of the technology's use in new and innovative ways.

Current Methods for Drug Quantitation

Before modern day MS, small molecule quantitation was achieved using high pressure liquid chromatography (HPLC) and ultraviolet (UV) detection. UV detectors measure the ability of chromaphores in compounds within a sample to absorb UV light. This can be accomplished at one or multiple wavelengths within the range or 190-400 nm. Most organic compounds can be measured by UV detectors.[9] However, this methodology suffered from lack of specificity and sensitivity. There are instances when a drug metabolizes but the metabolites retention time and detection are the same as the parent compound. Mass spectrometry has filled this need for both specificity and sensitivity in the quantitation of small molecules along with the ability to distinguish parent drug compound from its metabolites. Liquid chromatography tandem mass spectrometry (LC-MS/MS) is now the de facto technique for providing quantitation data for drug evaluation and submission for drug approval.[10]

The accepted way of performing MS quantitation is by using a mass spectrometer capable of MS/MS fragmentation. MS/MS used in conjunction with quantitation is commonly accomplished with a triple quadrupole or ion trap mass spectrometer. The reason MS/MS is required is because many compounds have the same intact mass. While many researchers use the first dimension of MS to perform quantitation, that technique again suffers from lack of specificity especially in very complex matrices. The second dimension of MS fragmentation in the majority of cases provides a unique fragment. The combination of the specific parent mass and the unique fragment ion is used to selectively monitor for the compound to be quantified. [11-14] However, while this technique offers specificity and sensitivity the protocols required for the analysis cause the loss of spatial information.

MALDI Imaging Mass Spectrometry

New advances in MS now provide the opportunity for investigative studies of molecular interactions in intact tissue, much like studies conducted decades ago with intact tissue for metabolic studies, but now with exquisite molecular specificity. In particular, matrix-assisted laser desorption/ionization (MALDI) imaging mass spectrometry (IMS) provides the investigator with the ability to analyze the spatial distribution of molecules directly in tissue specimens.

IMS can be used to localize specific molecules such as drugs, lipids, peptides and proteins directly from fresh frozen tissue sections with lateral image resolution down to 10 µm. Thin frozen sections (10-15 µm thick) are cut, thaw-mounted on target plates and subsequently an energy absorbing matrix is applied. Areas are ablated with an UV laser, typically having a target spot size of about 50 µm diameter, and give rise to ionic molecular species that are recorded according to their mass-to-charge (*m/z*) values. Thus, a single mass spectrum is acquired from each ablated spot in the array. Signal intensities at specific *m/z* values can be exported from this array to give a two-dimensional ion density map, or image, constructed from the specific coordinate location of that signal, and its corresponding relative abundance. For high resolution images, matrix is deposited in a homogeneous manner to the surface of the tissue in such a way as to minimize the lateral dispersion of molecules of interest. This can be achieved by either automatically printing arrays of small droplets or by robotically spraying a continuous coating. Each micro spot or pixel coordinate is then automatically analyzed by MALDI MS (Figure 2). From the analysis of a single section, images at virtually any molecular weight may be obtained provided there is sufficient signal intensity to record.

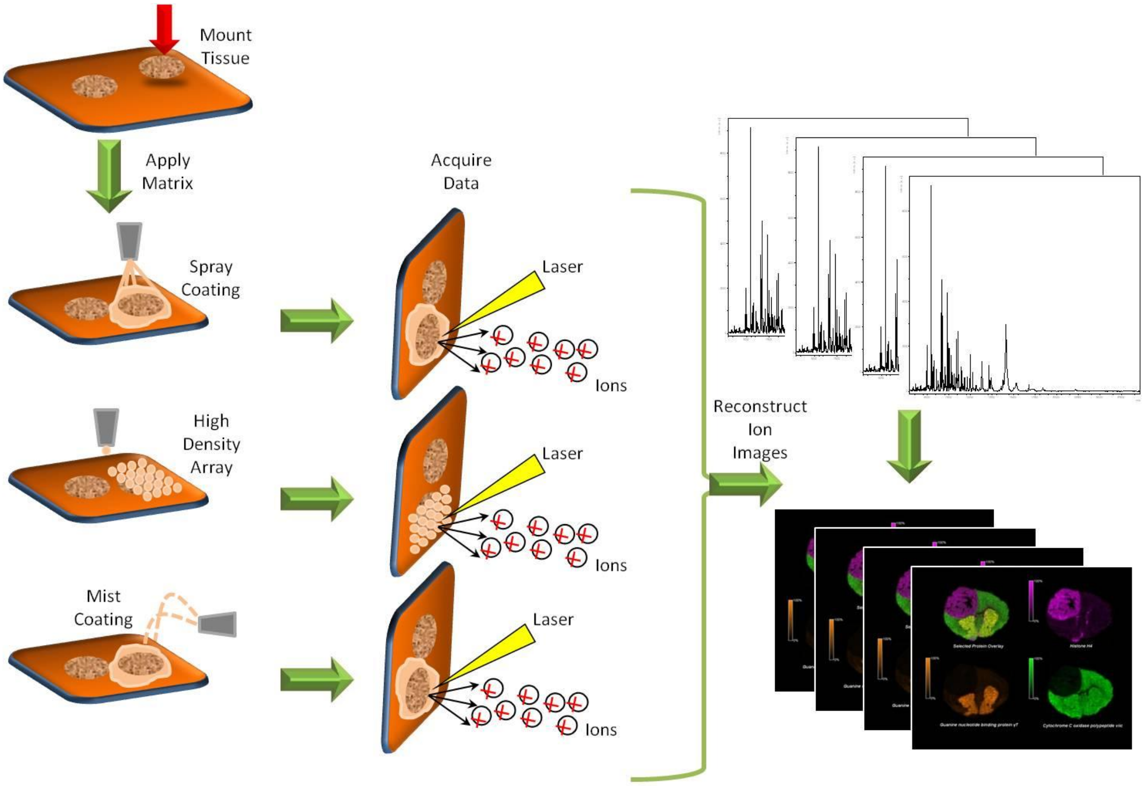

Figure 2: Cartoon schematic of a typical direct tissue imaging experiment. The figure demonstrates three types of matrix application; spray coating, high density droplet array, and mist coating. Subsequent image acquisition is shown for each technique.

One of the most compelling aspects of IMS is the ability to simultaneously visualize the spatial arrangement of hundreds of analytes directly from tissue without any prior knowledge or need for target specific reagents such as antibodies. IMS provides the ability to visualize post translational modifications and proteolytic processing while retaining spatial localization. Other MS techniques, such as secondary ionization mass spectrometry (SIMS), have also seen use for a variety of imaging applications.[15-17] One of the major advantages of SIMS is that it is capable of high resolution imaging (50-100 nm) for elements and small molecules (*m/z* <1000 Da). However, thus far, it has not been shown to be effective for the analysis of proteins and large peptides.

Instrumentation and Experimental Process

The mass spectrometry instrumentation best suited for the analysis of peptides and proteins directly from tissues is MALDI time-of-flight (TOF) technology. The ablation process directed by the focused laser beam together with the high frequency of the laser pulse renders this the favored ionization method for imaging. The duty cycle of a modern TOF analyzer is an ideal match for the pulsed laser process and also has the advantage of a theoretically unlimited mass range, high ion transmission efficiency, multiplex detection capability and simplicity in instrument design and maintenance.[18]

A typical analysis of proteins directly from tissue is described for illustrative purposes. Additional descriptions of a MALDI TOF MS can be found in other works.[19, 20] Two main experimental approaches may be used: profiling and imaging. Profiling involves analyzing discrete areas of the tissue sections and subjecting the resulting protein profiles to computational analysis. Typically, this uses 5–20 spots, each approximately 0.2–1 mm in diameter. These experiments are designed to make comparisons between representative areas on a single piece of tissue, such as normal healthy area and diseased area, or between two different specimens. Thus, in the 'profiling' mode, fine spatial resolution is not required. A sufficient number of areas must be sampled to gain statistical confidence in the results and this will vary depending on the specific experiment. On the other hand, high resolution imaging of a tissue requires that the entire tissue section is analyzed through an ordered array of spots, or raster, in which spectra are acquired at intervals that define the image resolution (e.g. every 50 µm in both the x and the y direction). 2D ion intensity maps, or images, can then be created by plotting the intensities of any signal obtained as a function of its x, y coordinates. The resulting images allow protein localization differences between and among samples to be rapidly assessed.

Tissues used for analysis should be frozen in liquid nitrogen immediately after resection to preserve the morphology and minimize protein degradation through proteolysis. The tissue is usually sectioned in a cryostat to give 10-12 µm thick sections and thaw-mounted onto an electrically conductive sample plate.[19] Sample plates include gold-coated or stainless steel metal plates and glass slides that have a conductive coating. The tissue may be gently rinsed with ethanol as a fixative and wash to remove lipids and salts. Alternatively, IMS compatible tissue staining protocols can be used in conjunction with the optically transparent glass slides, allowing correlation of IMS data with histological features of the same section by optical microscopy.[21]

MALDI IMS requires the application of energy absorbing matrix. This is typically a small organic molecule that co-crystallizes with the analytes of interest on the tissue surface. The matrix is capable of absorbing laser energy causing the analyte to desorb from the sample surface and ionize. The most commonly used matrices include 3,5-dimethoxy-4-hydroxy-cinnamic acid (SA), 2,5-dihydodroxybenzoic acid (DHB) and α-cyano-4-hydroxycinnamic acid (CHCA). (Figure 3) Solvent combinations and the matrix used will vary depending on the type of molecule and tissue being investigated.[19] A 50:50 (v/v) acetonitrile/water or ethanol/water mixture is generally recommended for use in tissue analysis. SA is an excellent matrix for the analysis of protein[19] and DHB and CHCA are primarily used for the analysis of peptides and lower molecular weight analytes.

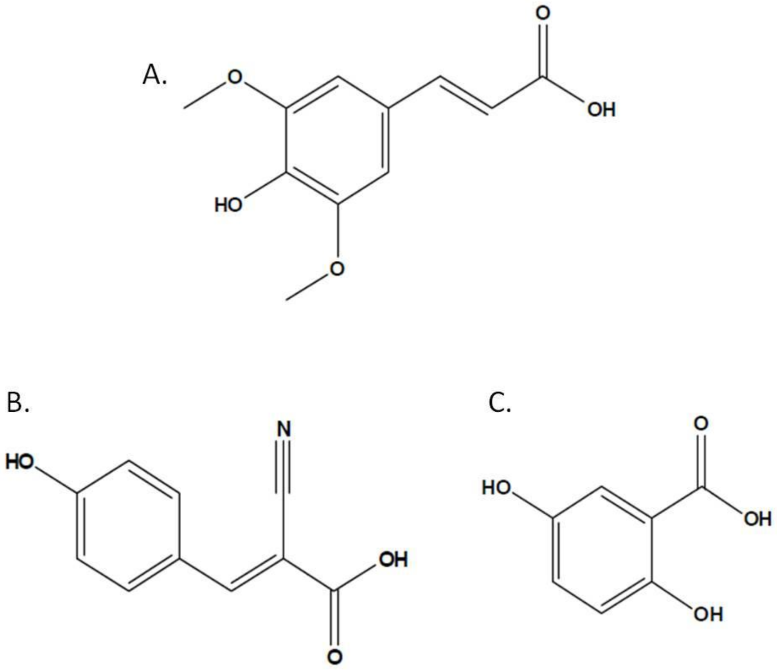

Figure 3: Structures of the common matrices used in MALDI MS analyses. A) 3,5-dimethyoxy-4-hydroxycinnamic acid (sinapinic acid, SA),
B) α-cyano-4-hydroxycinnamic acid (CHCA), and C) 2,5-dihydroxybenzoic acid (DHB).

For high resolution imaging, the matrix solution should be homogenously deposited across the tissue section in such a manner to avoid significant lateral migration of analytes. Currently, this is achieved by applying matrix solution to the tissue in either a spotted array or a homogenous spray coating.[19] A continuous and homogenous spray coating allows the highest spatial resolution, but densely spotted arrays show higher reproducibility and generally better spectra quality. A number of robotic spotting devices are commercially available and utilize acoustic,[22] piezoelectric,[23] inkjet printer,[24] and capillary deposition techniques[25]. Several robotic spray coating devices are also commercially available and utilize a mist nebulizing method[26] or a thermally-assisted spray method.[27]

Protein analysis is usually performed on a linear TOF instrument to achieve highest sensitivity. Ions formed and desorbed during the laser pulse are extracted and accelerated into the field free region of the TOF analyzer. Ions are usually detected by a multi-channel plate detector and the time of flight of the various ions is inversely proportional to their *m/z* values. This time measurement is then converted to *m/z* through appropriate calibration procedures. For the analysis of low molecular weight species, an ion mirror or reflectron can be used in the ion flight path to compensate for the initial velocity/energy distribution and improve resolution.[28]

Other analyzer combinations have been used with MALDI IMS including TOF-TOF,[23] orthogonal TOF and orthogonal Quadrapole-TOF (Q-TOF),[29, 30] ion mobility,[31] fourier transform ion cyclotron resonance (FTICR) [32, 33] and ion trap technologies.[34, 35] These additional tools have provided capabilities for protein identification, high mass resolution acquisition and the ability to detect small molecules such as drugs and metabolites.[23, 29-32, 34]

Applications of MALDI IMS

To date, considerable effort has been focused on finding molecular markers as early indicators of disease. MALDI IMS provides a means to visualize molecularly specific information while maintaining spatial integrity. For example, cancer progression is dependent on essential characteristics such as the presence of growth factors, insensitivity to growth-inhibitory signals, evasion of apoptosis, high replicate potential, sustained angiogenesis, and tissue invasion and metastasis.[36] Alterations in protein expression, proteolytic processing and post-translational modifications all contribute to this cellular transformation. IMS analyses of tissue sections reflect the overall status of the tissue, therefore, analyses of tissues in different states can reveal differences in the expression of proteins which otherwise could not be predicted. Thus, IMS has been used to image protein distributions in multiple types of cancer. Imaging analysis has been used to probe proteome changes in mouse breast and brain tumor.[37, 38] glioblastoma biopsies,[39] human lung metastasis to the brain,[40] and prostate.[37, 41] Identifying features that display differential expression patterns between cancerous and normal tissue can provide valuable insight into the molecular mechanisms, provide molecular diagnostic and prognostic signatures, and identify possible drug targets in implicated pathways.

In addition to the ability to assist in disease differentiation/diagnosis, the proteome signature of a tissue can also be used for determining the effects of drug/small molecule administration to an animal model or patient. Over the past decade, proteins have become principle targets for drug discovery and proteomics-oriented drug research has come to the forefront of activity in this area. Proteomics can play a major role in drug development including target identification, target validation, drug design, lead optimization, and pre-clinical and clinical development.[42] Due to the lengthy and complex drug discovery process,[43] it is essential to find ways to speed-up and streamline this process. With the early assessment of the distribution of a drug candidate in targeted tissues, IMS can greatly assist in the discovery and validation of processes related to drug ADME.[44, 45] For example, IMS can individually detect the presence and location of a drug and its metabolites in a label-free protocol, a significant advantage over other small molecule imaging techniques which typically require the addition of a radioactive tag to the molecule of interest such as in autoradiography. Another advantage of IMS is that it is capable of providing information on both the pharmacological and biological effects of a drug in that it can detect molecular features that may be markers of drug efficacy or toxicity. Other imaging techniques give little information on the molecular identity of these biological endpoints. Thus, IMS can monitor the analyte of interest and also the corresponding proteome response. An example of this is work performed in the discovery of transthyretin as a marker for Gentamicin-induced nephrotoxicity in rat.[46] Gentamicin-induced nephrotoxicity is seldom fatal and is usually reversible but often results in long hospital stays. Thus, there is great interest for finding potential markers of early toxicity and also to help elucidate the molecular mechanism. Investigators utilized MALDI IMS to determine differential protein expression within the rat kidney (cortex, medulla, and papilla), identified features of interest between dosed and control rat, and then applied downstream protein identification procedures. Transthyretin was significantly increased in the treated mouse kidney over control and these finding were validated with western blot and immunohistrochemistry.[46]

These same procedures can also be applied to whole-body animal tissue sections for a system wide analysis in a single experiment.[29] For whole-body sagittal tissue sections, using the same sample preparation and analysis conditions described for IMS experiments of tissues, exogenous small molecule signals found in various organs were detected and used to produce images of dosed rat sections (Figure 4). By expanding the capabilities of MALDI IMS to investigate multiple tissue types simultaneously across a whole-body tissue section distinct protein patterns as well as small molecule distribution can be identified and used to monitor whole-body system dynamics.

The molecular complexity of biological systems obviates the need for molecularly specific tools to elucidate proteomic events in both spatial and temporal distributions. One of the most effective ways to present such information is in the form of images, as demonstrated through Magnetic Resonance Imaging (MRI), Positron Emission Tomography (PET), and confocal microscopy. Similarly, images of the molecular composition of living systems will allow us to gain a more comprehensive view of biological processes and reveal complex molecular interactions. This approach will be vital in elucidating molecular aspects of disease, such as primary brain tumors, and also drug effectiveness by providing spatial and relevant time-based information.

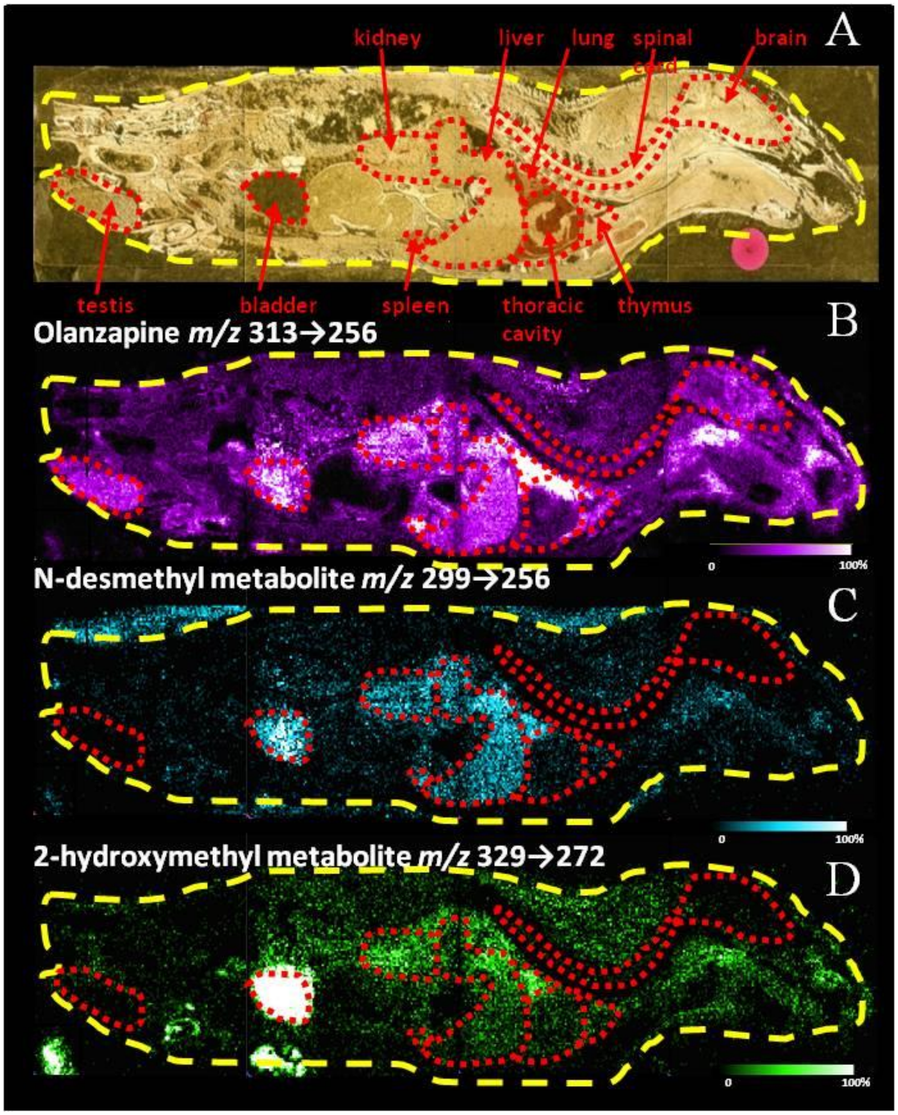

Figure 4: MALDI images of Olanzapine and it major metabolites in whole body rat tissues. A) Optical image of rat sagittal section across four gold MALDI target plates. B) Ion image of Olanzapine MS/MS ion 256. C) Ion image of N-desmethyl metabolite MS/MS ion 256. D) Ion image of 2-hydroxymethyl metabolite MS/MS ion 272. (Images courtesy of Dr. Sheerin K. Shahidi)

Primary Brain Tumors

In this study the above technology will be applied to primary brain tumors. Primary malignant brain tumors, which are tumors that start in the brain, account for 2 percent of all cancers in adults living in the United States (U.S.).[47] There are many types and subtypes of primary brain tumors. They include gliomas (which include astrocytomas, oligodendrogliomas, and ependydomas), meningomas, medullablastomas, pituitary adenomas, and central nervous system lymphomas.[47, 48] Figure 5A shows a photograph of an excised patient brain with a glial tumor. The upper left portion of the brain is consumed with the tumor mass. More recently the World Health Organization (WHO) classification has been expanded to include additional types of primary tumors such as angiocentric glioma, glialneuronal tumors, and atypical choroid plexus papillomas.[49] Brain tumors produce a variety of symptoms, including headache, seizure, and neurological changes, whose onset could progress gradually or could occur at a very rapid rate.

Diagnosis of brain tumors involves a neurological exam and various types of imaging tests. Imaging techniques include MRI, computed tomography (CT), and PET scan. Typically biopsies are performed as part of surgery to remove a tumor, but there are cases where it is performed as a separate diagnostic procedure.[47, 48] The standard approach for treating brain tumors is to reduce the tumor as much as possible using surgery, radiation treatment, or chemotherapy. Typically, such treatments are used in various combinations with each other. Survival rates in primary brain tumors depend on the type of tumor, patient age, functional status of the patient, and the extent of surgical tumor removal. Figure 5B displays some typical glial tumor diagnoses along with the average survival time for patients post surgery. In recent years, survival of the treatment of a (solid) neoplasm of the brain has dramatically increased. Survival for the higher graded tumors, as well as long term survival of younger patients, is also on the rise. Patients with benign gliomas may survive for many years,[50, 51] while survival in most cases of glioblastoma multiforme is limited to a few months after diagnosis if treatment is ignored. New molecularly targeted therapies are now coming to the forefront of research with the hopes of increasing survival and quality of life for patients at even a much better rate. Two of those therapies will be investigated in this study and are discussed in later chapters.

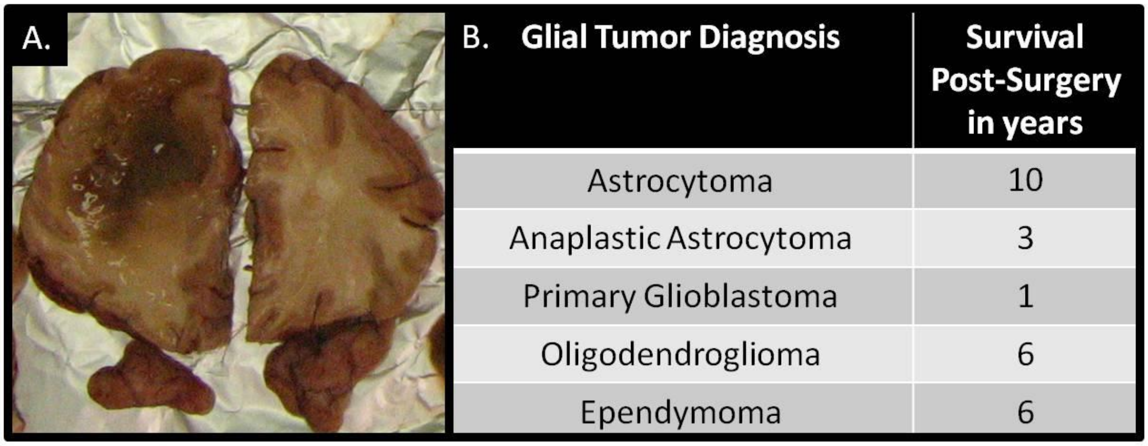

Glial Tumor Diagnosis	Survival Post-Surgery in years
Astrocytoma	10
Anaplastic Astrocytoma	3
Primary Glioblastoma	1
Oligodendroglioma	6
Ependymoma	6

Figure 5: Human glioma tumors. A) Photograph of an excised patient brain with a glioma. B) The WHO naming classification for types of gliomas along with patient survival post-surgery. The upper left portion of the brain is consumed with a tumor mass.

Biomarker Discovery

In recent years, clinical practice has shifted focus to the concepts of personalized medicine which includes the use of targeted molecular therapy. Toward this goal, biomarkers are providing early diagnosis of diseases and are helping physicians determine safe and effective medication dosages as well as new possible drug targets.[52] The National Institutes of Health (NIH) defined biomarkers as characteristics that are objectively measured and evaluated as indicators of normal biological processes, pathogenic processes, or pharmacologic responses to therapeutic interventions.[53] In a disease such as cancer the identification of a molecule or molecular signature that is accurately indicative of these processes will be of extraordinary benefit to clinicians and patients.[54] For these biomarkers to be put into clinical practice for the goal of personalized medicine, extensive research, testing and validation needs to be performed.

The main hypothesis driving the search for cancer biomarkers is the concept that organs secrete a specific set of proteins representing a molecular signature indicative of its physiological state.[55] Genetic mutation and other altered biological processes will affect the proteins that are secreted and expressed becoming a unique signature to a disease phenotype.[55] Detection and characterization of these molecular fingerprints provides a unique view into the biology associated with various disease states. The potential use of biomarkers for the early detection of cancer has compelled significant research in this field.[54, 56]

Another advantage of biomarkers is the potential to aid clinicians in selecting patients to undergo certain treatments. This research is conducted based on previous evaluations of treatment efficacy and safety from patients exhibiting a specific biomarker or group of markers. These markers may also be used to monitor response to treatment and disease progression.[57]

Numerous studies have been published describing the discovery of putative biomarkers using mass spectrometry.[25, 43, 58, 59] Although these studies established a trend-setting basis for mass spectrometry in biomarker research, they also initiated a controversial debate questioning the clinical validity of the obtained results. It needs to be noted that new potential biomarkers discovered through the proteomics process need to undergo a chain of discovery and identification, validation in clinical trials, and approval by regulatory agencies before they are implemented in clinical practice (Figure 6).[60]

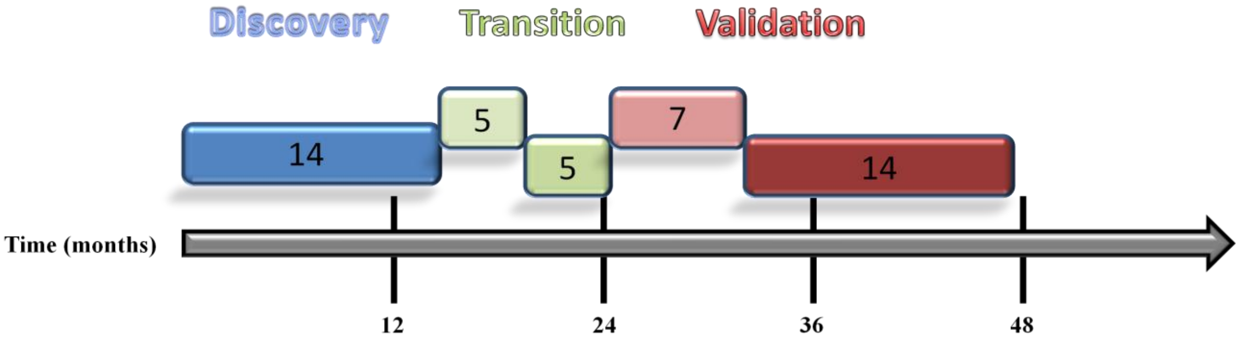

Figure 6: Developmental phases and estimated timeline for the discovery and validation of biomarkers.

Summary and Objectives

Drug discovery and development is a long and complex process and there is an ever present need for new technologies and methods to aid in making the procedures more efficient and cost effective. MS is already involved in almost every stage of the drug development process, from new chemical entities to formula determination to target profiling and preclinical work. It is even used in end stages of manufacturing and quality assurance and much research is focused on using MS for diagnostics. One can identify numerous areas where MALDI IMS could be implemented to assist in the monitoring of an administered drug and its metabolites, discover potential drug targets, assist in diagnosis and evaluate the effects of a treatment.

The goal of the research presented here is to implement MALDI IMS for the purpose of demonstrating its effectiveness and usefulness in the drug discovery and validation processes. Drug distribution can be evaluated as well as quantitative information obtained at localized points without losing spatial integrity due to homogenization processes. Pharmacodynamic effects will also be studied toward identifying possible features for biomarker validation that represent not only disease state, but which can be used as indicators of targeted molecular therapy treatment responses in glioma primary brain tumors.

Chapter II will address how with MALDI IMS it is possible to achieve small molecule quantitation directly from tissue sections without the need for additional sample treatment or separation techniques. Current methodologies do not have the capability of retaining spatial information related to the drug concentration and require laborious protocols involving homogenization and extraction techniques. The MALDI IMS quantitation methodology developed will provide a solution to the issues presented by LC-MS/MS methods. In addition, small molecule images will be obtained along with protein images to allow for the correlation of drug tissue distribution and therapeutic response within the same sample

The quantitation protocol has been applied to the investigation of two therapies under investigation for the treatment of Glioblastomas (brain tumors of glial cell origin) to determine the quantities of compound that reach the brain and tumor areas in mouse models. In addition to drug quantitation, the treatment effects on the proteome of the brain were investigated in relation to the amount of drug present. Chapter III focuses on the investigation of the molecularly specific therapy imatinib and Chapter IV explores the effects of the plant alkaloid cyclopamine on the gliomas. Future work will be discussed in Chapter V that demonstrates how the affected protein signals found in the mouse models can be related back to human tumor biopsies, demonstrating the feasibility of utilizing mouse models to discover protein signatures that can be used as indicators of therapy response. All of this work demonstrates the value that MALDI IMS has in the drug development process and the advantages that it can provide.

CHAPTER II

DRUG QUANTITATION PROTOCOL DEVELOPMENT

Overview

Typically analysis of small molecules by MS has relied on the use of liquid chromatography tandem mass spectrometry.[11-14] Information ranging from structural characterization to pharmacokinetic extraction studies can be obtained. These analytical evaluations provide vital information regarding the preclinical ADME properties of potential therapeutic compounds. In the pharmaceutical industry, distribution studies of drug candidates are performed to gain knowledge about the localization and accumulation of drugs in various tissues throughout an animal. While the LC-MS/MS technique proved invaluable for drug quantities in tissues, there is a loss of spatial information regarding drug distribution due to the necessity of homogenization methodologies prior to analysis. MALDI mass spectrometry can fill this information gap by providing drug distribution information with relatively easy sample preparation. Typically in the past, MALDI MS has been overlooked as a viable option for small molecule quantitative studies. Analysts have usually assumed that potential differences in ionization efficiency between analyte and internal standards and an inherent heterogeneity of the sample spot would limit MALDI MS as a quantitative technique.[61] However, with the introduction of automated spotters and newly developed protocols, the use of MALDI mass spectrometry for small organic molecule quantitation can become a reproducible and reliable analytical procedure. *The protocol developed here involving* *robotic sample preparation combined with automated MALDI mass spectrometry provides a viable method for quantitation of small molecules.*

Introduction

Issues with Quantitation

LC-MS/MS quantitation for tissue samples, while effective, still faces many issues that complicate the methodology. The first step of any quantitative tissue analysis usually involves that the tissue must be homogenized which causes the loss of any spatial information within the tissue. The next part of the process involves the extraction of the small molecule to be analyzed using a series of centrifugation steps, solvent washes and shaking, inversion or sonication. These processes can result in incomplete extraction, loss of the compound due to sticking or leeching into tube walls of the equipment used or ineffective sample transfer which would also affect the quantitation results. The LC process could also create inconsistencies in the results. Shifts or convoluted retention times due to changes in instrument parameters, interferences from other compounds and loss of the small molecule due to sticking on the column are all issues that could create fluctuations or inaccurate results. MALDI IMS can alleviate these issues while also performing the analysis with minimal sample preparation steps and an analysis time on the order of micro-seconds (µs) as opposed to minutes or even hours.

In the past, MALDI mass spectrometry was frequently not used for small molecule analysis because of chemical interference from the MALDI matrix in the mass range of a typical analysis (less than 1 kDa). However, the accepted way of performing mass spectral quantitation is by using a mass spectrometer capable of MS/MS fragmentation. MS/MS used in conjunction with quantitation is commonly accomplished with a triple quadrupole or ion trap mass spectrometer. The reason MS/MS is required is because many compounds have the same intact mass. Tandem mass spectrometry involves analyzing the product ions of a particular precursor ion. In the MALDI MS/MS instrument, the first mass analyzer acts as a mass filter by selectively allowing a narrow mass window (0.2 Da to 5 Da depending on the instrument), usually centered on the small molecule of interest, to continue on into the instrument, while preventing matrix molecules from entering, helping to eliminate the matrix interference that has stifled MALDI MS as a practical tool for small molecule analysis. The second process analyzes the specific product ions of the molecules of interest which serves as a specific fingerprint. Figure 7 shows the schematics of both a Q-TOF and a LTQ, two instruments used for MALDI MS/MS.

To assess changes in drug concentrations in a given tissue, pixel to pixel reproducibility must be high, that is, two pixels close together having the same drug concentrations should give the same spectra within acceptable standards. Although, this will vary from experiment to experiment, typically variations of ±30% or less are deemed acceptable. Factors that have a direct bearing on this aspect of the analysis include ionization efficiency of a given molecule, ion suppression effects, extraction efficiency of the matrix deposition process and the robustness and effectiveness of post acquisition processing. High pixel to pixel reproducibility can be achieved by careful attention to sample preparation and the matrix application steps. In addition, instrument parameters such as voltage settings and laser power must be kept constant within a given experiment.

A robotic matrix application device is invaluable in removing operator to operator variations.[29]

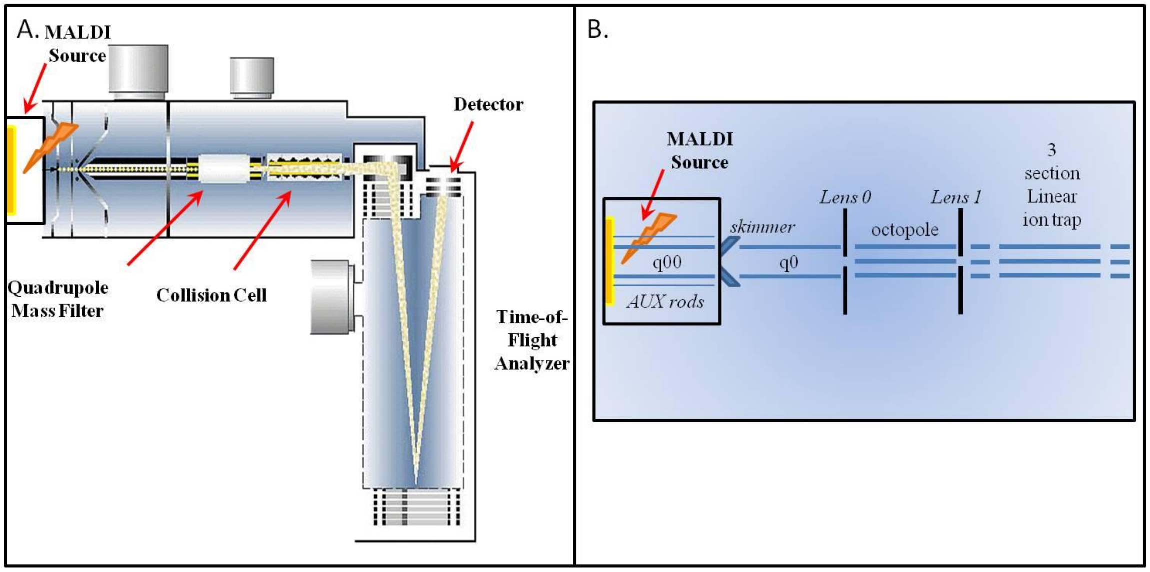

Figure 7: MALDI MS/MS instrument schematics. A) Schematic of the QStar XL (MDS Sciex, Concord, Canada) equipped with an oMALDI source (20 Hz 337 nm nitrogen laser) and a hybrid QqTOF mass analyzer B) Schematic of the MALDI LTQ XL (Thermo Scientific Inc.)

Importance of Internal Standards

An internal standard (i.s.) should be used when performing MS quantitation. An appropriate internal standard will control for extraction, sample introduction and ionization variability. An internal standard should be added at the beginning of the sample work-up and should be added at the same level in every sample including the standards and should also give a reliable MS response. The amount of the internal standard added needs to be well above the limit of detection but not so high as to suppress the ionization of the analyte. The best internal standard is an isotopically labeled version of the molecule you want to quantify. An isotopically labeled internal standard will have a similar extraction recovery, ionization response, and separation behavior as the analyte of interest.[62]

Results

Signal Depth

When acquiring small molecule data there a number of parameters that must be considered in order to accurately represent the amount of drug that is in the tissue. How many laser shots need to be acquired, how much of the matrix spot needs to be sampled spatially and how should the internal standard and the analyte desired be acquired from the same location. To begin investigating this, Olanzapine (OLZ) dosed tissue sections were cut and spotted with DHB matrix in 50% methanol spiked with 2 µM of d4-OLZ internal standard. Various positions across the matrix spots were analyzed collecting a spectrum every 45 laser shots. The data was then plotted comparing the area under the curve (AUC) for the MS/MS fragment (*m/z* 256) of the small molecule parent compound OLZ (*m/z* 313) versus the number of laser shots. As can be seen in Figure 8, the majority of the OLZ signal from the dosed tissue is acquired in the first 90 laser shots and then tapers off quite drastically with most signal for each position being entirely gone after 600 laser shots. Similarly, the d4-OLZ internal standard signal showed

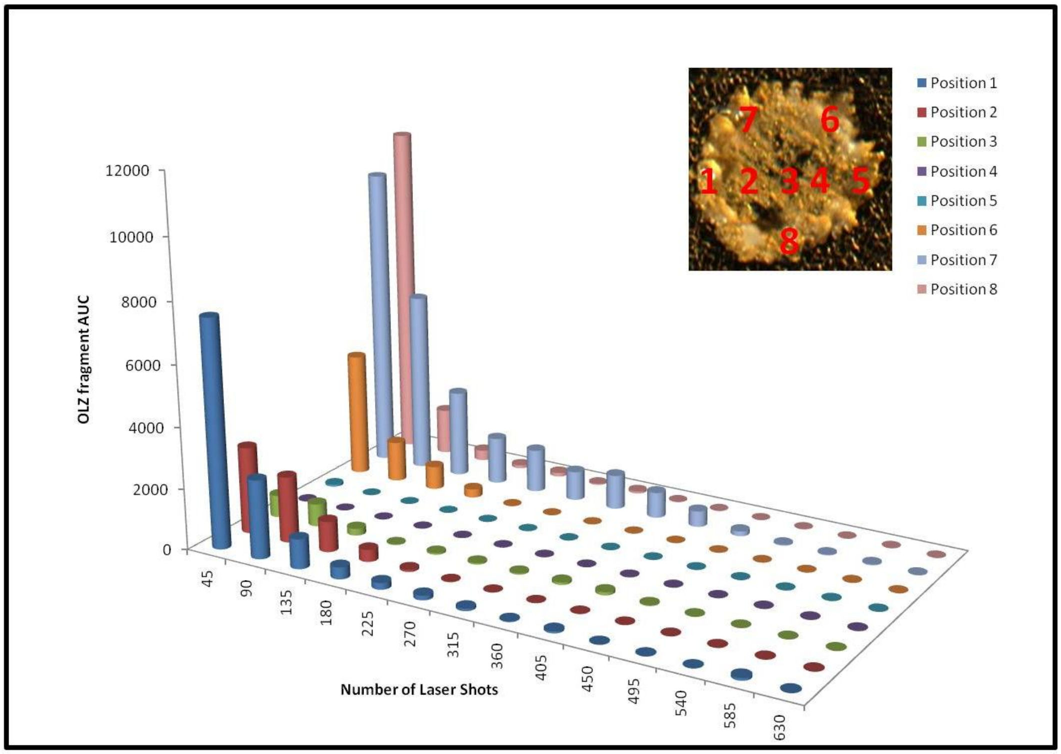

Figure 8: Major OLZ fragment (*m/z* 256) area under the curve plotted against the number of laser shots taken for each position across a DHB spot (approximately 250 µm diameter).

similar behaviors as displayed in Figure 9A. When looking at the major fragment of d4-OLZ (*m/z* 256) AUC again it is shown that the majority of the signal is acquired in the first 100 laser shots when spectra were taken every 45 laser shots. Looking at the data from spectra acquired every 15 laser shots (Figure 9B) it is seen that even within the 45 laser shot packet, the majority of signal is obtained in the first 15 laser shots and then decreases from there. This indicates that the first initial shots taken from a sample in small molecule analysis are critical if one wants to get an accurate representation of the

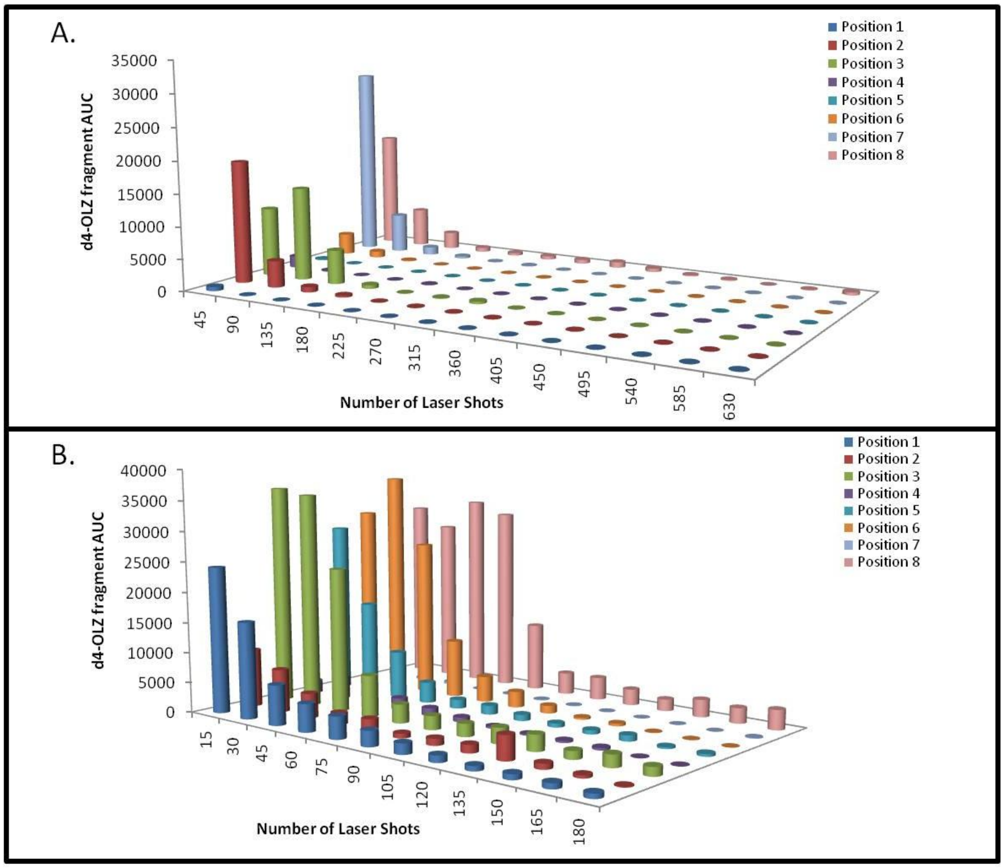

Figure 9: Major fragment (*m/z* 259) area under the curve for d4-OLZ plotted against the number of laser shots taken for each position across a DHB spot. A) Spectra acquired every 45 laser shots. B) Spectra acquired every 15 laser shots.

amount of drug present in a tissue. However, it is also necessary to collect beyond these first initial shots to obtain all the signal given by the drug.

Area Ablated Calculation

Looking at the spectra acquired from the various locations within the matrix spot, it is clearly seen that the crystallization of the matrix affects the drug signal. There are variances in drug signal across the matrix spots. This leads to the conclusion that one position within the matrix spot is not an accurate representation of the amount of drug present. It is necessary to evaluate multiple positions within a matrix spot. In order to determine how many positions need to be analyzed to represent the amount of drug in a given matrix spot, it must first be determined what area of the matrix spot is being sampled by the laser. By evaluating laser burn patterns in a thin layer of DHB (sublimed onto the target pate) the laser spot size dimensions can be determined. Laser spot size is dependent on the number of laser shots being taken in a particular location and the laser power used. For these experiments the laser power was kept constant at 20 µJ, which was found to be the laser power necessary to obtain small molecule signal from the DHB matrix spots. However, the number of laser shots taken at a particular location was varied. The previous experiments showed that a bulk of signal was acquired in the first 90 laser shots, thus a burn pattern was achieved by shooting at a laser power of 20 µJ for a total of 90 laser shots in the same spatial position (Figure 10A). This resulted in an elliptical burn pattern size of 136 x 16 µm giving a total ablated area of 1709 μm^2, while a burn pattern achieved by shooting for a total of 600 laser shots, which is the number of laser shots needed to ensure all the signal has been detected, was 153 x 31 µm giving a total ablated area of 3725 μm^2 (Figure 10B). Note that all laser burn pattern measurements were taken from no less than a total of ten spots and resulted in percent relative standard deviation (%RSD) values of less than 12%.

Looking at the laser burn areas from a micro-raster pattern it can be determined what spatial resolution will be required to ablate all of the matrix in a given area. Laser burn patterns were generated from a micro-raster of 50 µm x 4 positions within a spot and an overall spatial array of 300 x 300 µm using both 90 laser shots per position and

600 laser shots per position (Figure 10 C and D respectively). It is seen that the 90 laser shots per position in this micro-raster pattern does not ablate all of the matrix within the entire encompassed area, while the 600 laser shots per position condition does indeed ablate all of the matrix within the given area of the micro-raster. The total ablated area within the 600 laser shots per position condition is approximately 16650 µm^2. The area ablated by the laser needs to be taken into consideration when evaluating the quantity of a small molecule within a tissue so that the amount of sample that is analyzed can be known. In order to ensure that all of the signal is being obtained from a given area it is necessary to use 600 laser shots per position with a micro-raster of 50 µm across the matrix spot being analyzed. For a 250 µm matrix spot, a total of 14 micro-rasters at 50 µm need to be analyzed to ablate the whole spot. The sum of the intensities at each location can be taken and then added together to give the total intensity sum over the entire matrix spot. Thus, the investigator will know the total area sampled and the total intensity of the small molecule being investigated from any given evaluated area.

Tissue Dimension Calculations

In addition to knowing the total area that is being sampled the amount of tissue under that area needs to be known. This can be done by obtaining the mass of a brain section along with its total area so that the mass of the tissue under the matrix spot can be calculated. To do this, a total of ten sections of brain tissue at 12 µm thickness were cut and then immediately weighed on a microbalance. The total mass of the ten sections was then divided to obtain the mass of one thin tissue section. This experiment was repeated

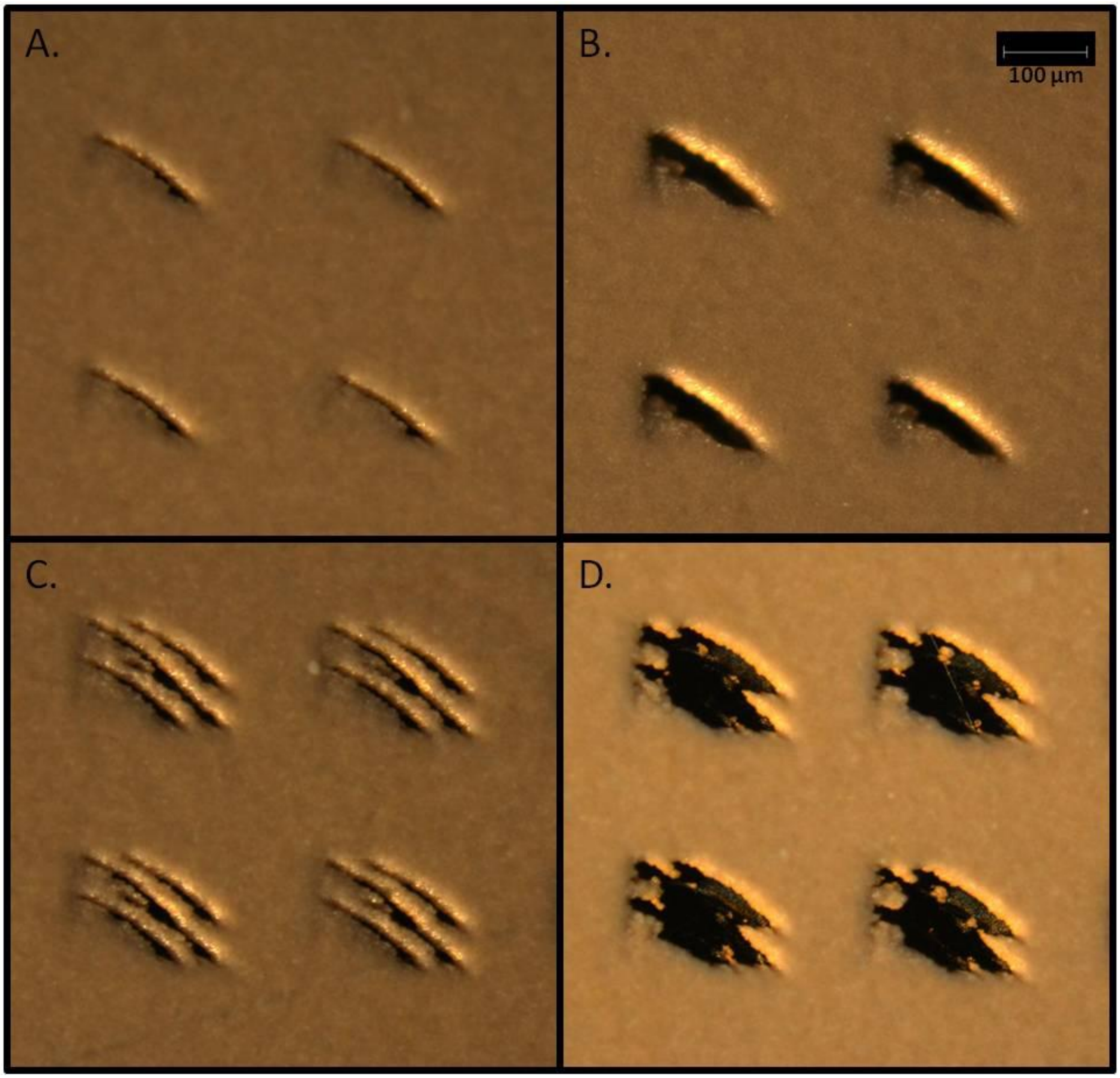

Figure 10: Laser burn patterns on a thin layer of DHB photographed at 10x magnification. All burn patterns were created with a laser power of 20µJ. A) 90 laser shots per position in a 300 x 300 µm array. B) 600 laser shots per position in a 300 x 300 µm array. C) 90 laser shots per position in a 50 µm micro-raster pattern (x4) in a 300 x 300 µm array. D) 600 laser shots per position in a 50 µm micro-raster pattern (x4) in a 300 x 300 µm array.

five times for each tissue type analyzed. A 12 µm rat brain section had an average mass of 1.02 mg with a RSD of 8%. To get the total tissue area, 12 µm brain sections were cut, thaw mounted onto microscope slides, stained with cresyl violet and then scanned on a flat bed scanner at 3200 dpi. The scanned images were imported into Adobe Photoshop so that the area could be calculated. The area of the rat brain section was 250 mm^2 with a RSD of 0.3%. Using these dimensional measurements it is possible to calculate the amount of tissue being sampled under any one given matrix spot.

Acquisition Methods

When using an internal standard it is important to evaluate the best way to acquire both signal for the analyte of interest to be quantified and the signal given by the internal standard to be used for normalization. Ideally, both signals will be acquired from the same spatial location within the tissue section to give the most accurate results. As can be seen by the signal depth experiments, the first shots of an acquisition are critical to obtain all of the drug signal within a location. When alternating acquisition of analyte of interest and internal standard this needs to be taken into consideration. Thus matrix spots with known concentrations of OLZ standard and d4-OLZ standard were analyzed using two methods. One method acquired internal standard (d4-OLZ) in the first 15 laser shots and then the analyte of interest (OLZ) in the next 15 laser shots alternating from there until 600 laser shots had been acquired at each location. The second method acquired OLZ spectra for the first 15 laser shots and then d4-OLZ spectra in the next 15 laser shots alternating until 600 laser shots had been acquired at each location. For each spot the total intensity sum was calculated for the OLZ and d4-OLZ standards and then the ratio of analyte/internal standard was calculated. Figure 11 shows the ratio results for the matrix spots revealing that there is no significant difference between the two acquisition

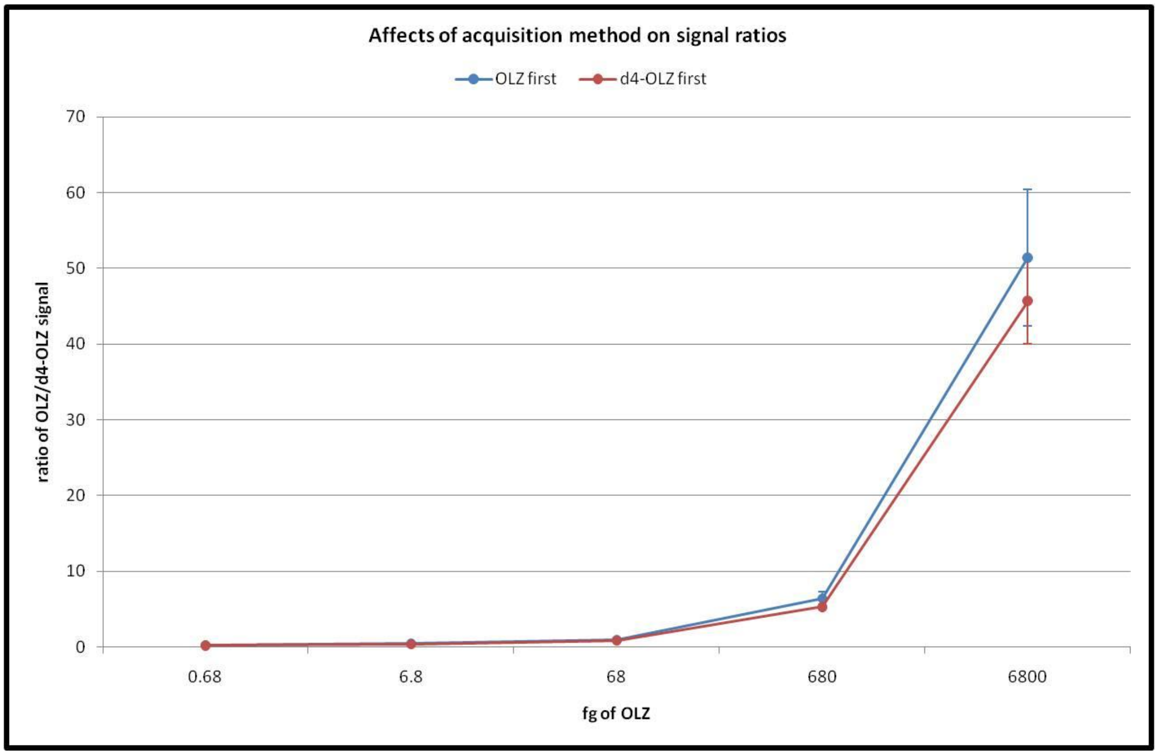

Figure 11: Effects of acquisition method on signal ratios detected from a dilution series of OLZ spiked matrix with 2 µM of d4-OLZ. The OLZ first series indicates that the first 15 laser shots were acquired for the OLZ major fragment then the next 15 laser shots were acquired for d4-OLZ major fragment, alternating until 600 laser shots were acquired. The d4-OLZ first series is d4-OLZ for the first 15 laser shots and then OLZ, alternating. The ratios collected by either method show no significant difference from each other.

methods. The ratios fit within the standard deviations of both acquisition methods and the percent difference was no higher than 15%.

Limits of Detection and Calibration Curves

The limit of detection (LOD) is usually defined as the lowest quantity or concentration of a component that can be reliably detected with a given analytical method. Intuitively, the LOD would be the lowest concentration obtained from the measurement of a sample (containing the component) that would be able to be discriminated from the concentration obtained from the measurement of a blank sample (a sample not containing the component).[63] [64] The parameters used here to determine the LOD are 3 standard deviations above the blank standard value.

A calibration curve is a method for determining the concentration of a substance in an unknown sample by comparing the unknown to a set of standard samples of known concentration. It is a plot of how the analyte signal changes with the concentration of the analyte. A line or curve is fit to the data and the resulting equation is used to convert readings of the unknown sample into concentration. In the instance of a linear fit :

$$\text{Signal} = \text{slope} \times \text{concentration} + \text{intercept}$$

Calibration curve standards of OLZ were added to matrix solutions to yield final concentrations of 100, 10, 1, and 0.1 ng/ml. A 2 µM concentration of d4-OLZ was also added to the matrix as an internal standard in each solution. For the analysis of OLZ, DHB in 50% methanol (MeOH) was used as the matrix. Using the Portrait™ 630, matrix spots were deposited onto tissue sections in known volumes. Knowing the volume of matrix standard deposited it is possible to calculate the amount of drug compound that was deposited onto the tissue within the matrix spot. For the standard curve the amount of drug within the matrix spots was 680, 68, 6.8 and 0.68 fg and a blank standard containing matrix only. As can be seen in Figure 12, the top panel shows a spectra taken from a blank matrix spot and shows no signal at *m/z* 256 where the OLZ MS/MS fragment would be, indicated by the red arrow. The bottom panel is a spectra taken from a matrix spot containing 680 fg of OLZ and shows a clear signal at *m/z* 256.

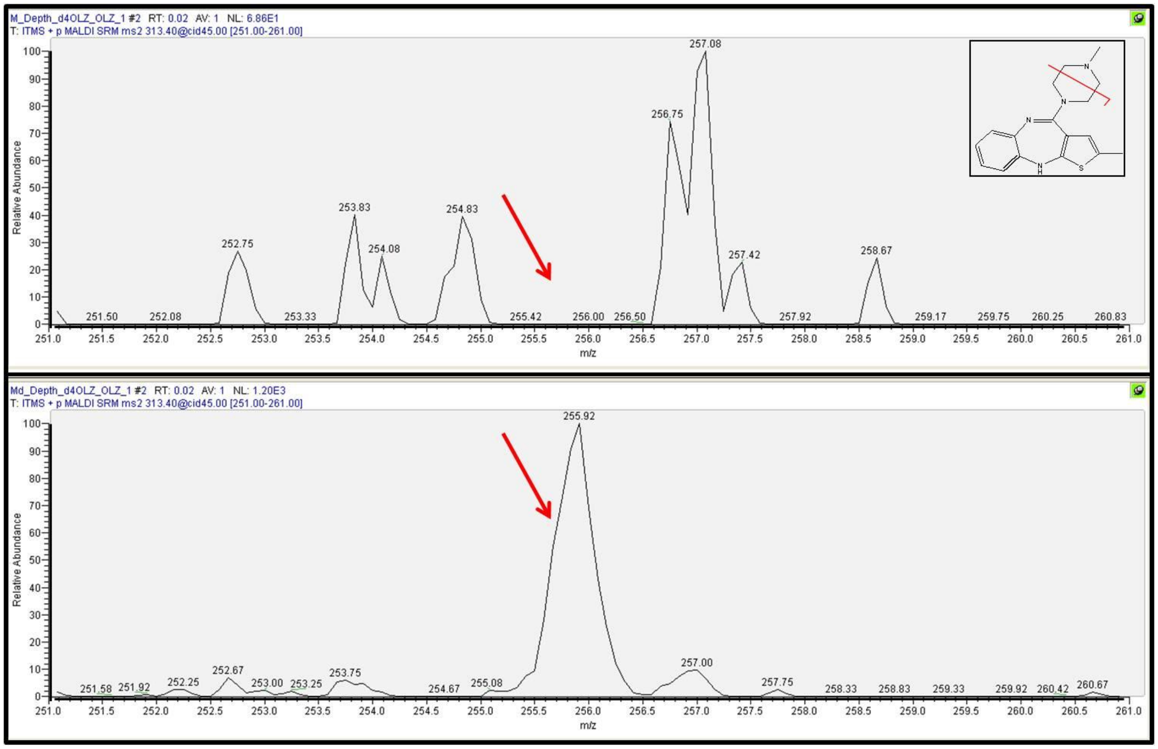

Figure 12: SRM spectra of olanzapine acquired on a MALDI LTQ A) Spectra taken from a matrix spot with no OLZ spike B) Spectra taken from a matrix spot containing 680 fg OLZ.

Using the acquisition methods described above, a total of ten matrix spots (140 positions) for each point on the OLZ calibration curve were analyzed and then the intensity ratios were averaged providing a RSD no higher than 20% and excellent linearity with an R^2 value of 0.9982 (Figure 13). From this analysis the LOD is above the analyte/internal standard ratio of 0.14 which equates to approximately 0.20 fg of OLZ within a 250 µm matrix spot.

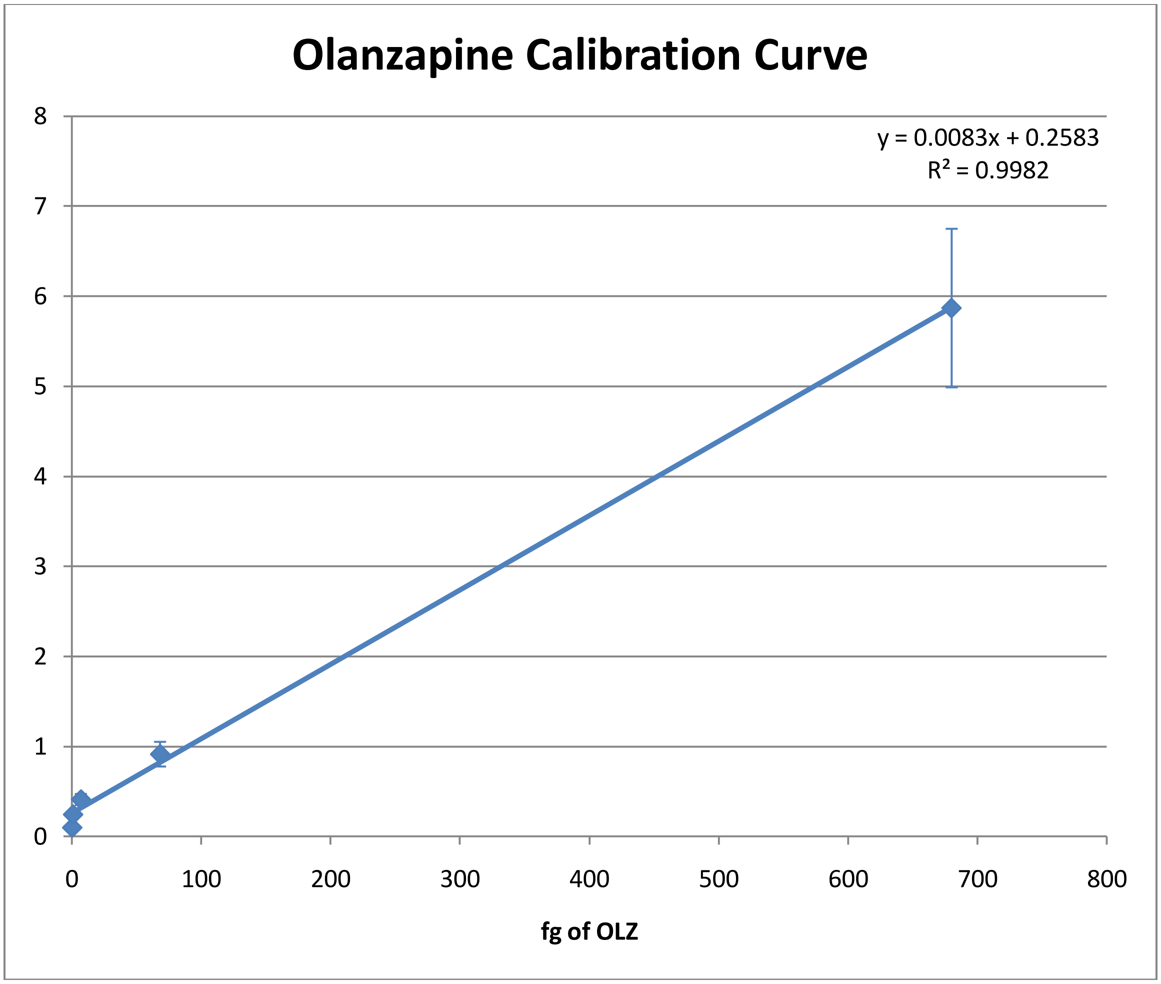

Figure 13: Calibration curve for OLZ showing ratios of OLZ/d4-OLZ signals against fg of drug in the matrix spots.

Discussion

Taking all of the information from the above experiments into consideration; it is now possible to outline a methodology for direct quantitation of small molecules from tissue using MALDI MS/MS. First dosed tissues need to be sectioned at a known thickness and the area of the section along with the section mass must be determined. The area ablated by the laser using experiment specific acquisition methods must also be determined. Using this information a simple ratio calculation can be performed to find the amount of tissue that is sampled within a specific location. For OLZ dosed rat brain the tissue section area was found to be 250 mm^2 and the tissue section mass was found to be 1.02 mg. The area sampled by the laser in one position acquiring a total of 600 laser shots at a laser power of 20 µJ is approximately 0.0035 mm^2. To find the amount of tissue sampled under one laser position the following equation was used: $250 mm^2/1.02 mg = 0.0035 mm^2/X mg$. From this calculation it was determined that $1.42x10^{-5}$ mg of tissue was sampled. A similar calculation was performed to determine the amount of tissue sampled under a 250 µm matrix spot. The matrix spot has an area of 49087 $µm^2$ which results in 5×10^{-4} mg of tissue sampled.

A calibration curve for the small molecule of interest must be acquired to provide an equation for determining how much of the small molecule substance is in the sample by comparing the unknown to a set of standard samples of known amounts. The dosed tissue sections were then cut at 12 µm and spotted with matrix (DHB, 40 mg/ml in 50% MeOH) spiked with an internal standard (d4-OLZ) and analyzed on the MALDI LTQ. For each matrix spot a total of 14 locations were analyzed to completely ablate all of the small molecule signal, taking 600 laser shots per location. A total of ten matrix spots were analyzed for each dosed tissue. Using in-house software (developed by Surendra Dasari) the total intensity sums were calculated for the OLZ signal and the d4-OLZ signal at each location. These totals were then used to get the ratio of OLZ signal over d4-OLZ signal within a matrix spot. The ratio values were plugged into the calibration curve's linear equation to result in the amount of drug present in each spot. Dosed tissue sections collected 2 hour (2h), 6 hour (6h) and 12 hour (12h) after a single dose of OLZ were analyzed and resulted in an average of 790 fg, 70 fg, and 15 fg respectively of OLZ compound. Dividing these values by the mass of the area sampled gave the average OLZ concentration taken from the analyzed matrix spots for each of the dosed tissues with an average RSD of 33%. At 2h post dose the OLZ concentration was 55.65 ng/mg, 6h post dose was 4.89 ng/mg and 12h post dose was 1.84 ng/mg.

To compare the OLZ concentration results, an LC-MS/MS extraction protocol was performed. The dosed tissues were homogenized, extracted and then analyzed on an ESI TSQ Quantum triple-quadrupole system. Using this methodology for the 2h, 6h, and 12h samples, the concentrations of OLZ were found to be 57.30 ng/mg, 3.74 ng/mg and 2.64 ng/mg respectively with an average RSD of 33%. Figure 14 displays the results for both the MALDI MS/MS analysis and the LC MS/MS analysis. It can be seen that the methodologies result in very similar concentrations for each of the dosed tissues. The 2h sample has a percent difference of 3, the 6h sample has a percent difference of 24 and the 12h sample has a percent difference of 13 (Table 1). This demonstrates that the MALDI MS/MS methodology developed here can be used to provide an accurate drug quantitation for dosed tissue sections with excellent reproducibility and low standard deviations.

In addition to the experiment descriptions provided in the material and methods section of this chapter a detailed step by step protocol is included in Appendix A that outlines the methodology developed to obtain absolute drug concentration directly from tissue sections using MALDI IMS.

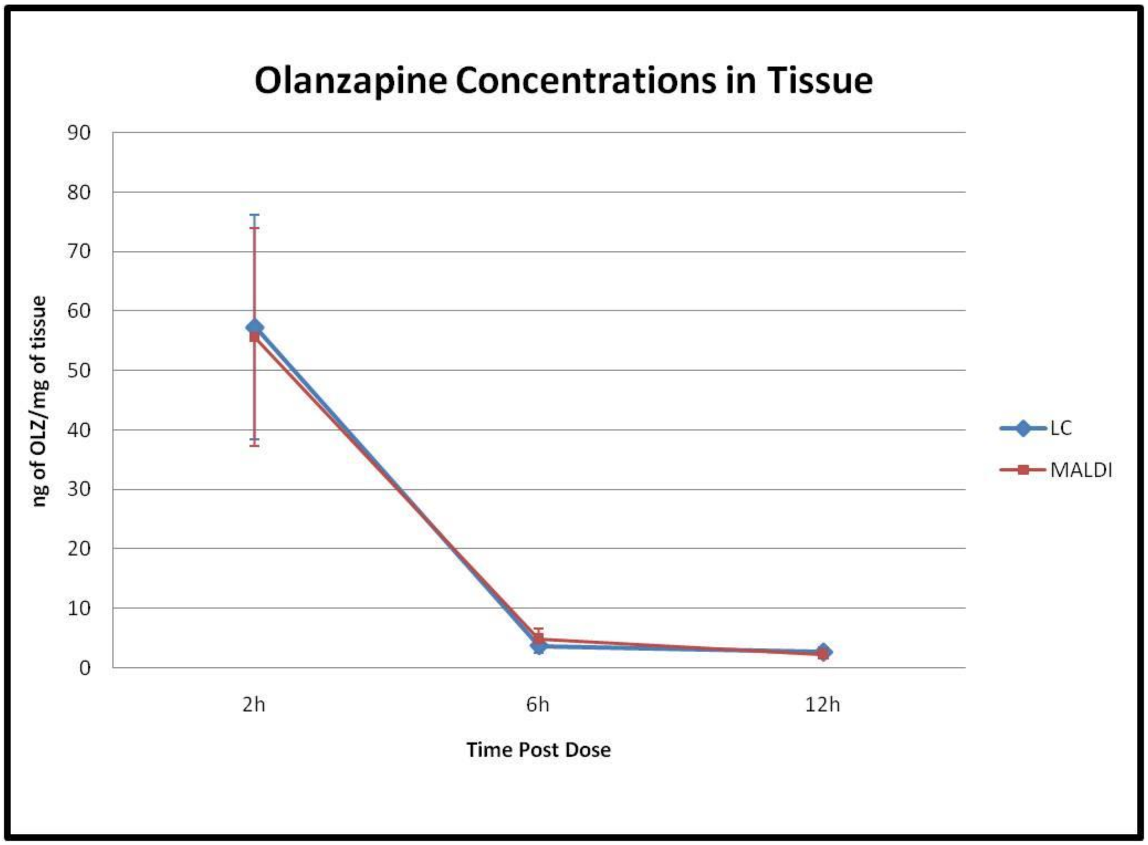

Figure 14: Comparison of MALDI IMS and LC-MS/MS quantitation methods for OLZ. Olanzapine concentration in ng of OLZ per mg of tissue as determined by LC-MS/MS and MALDI IMS experiments for each tissue sampled.

Table 1: Comparison of OLZ concentration values calculated with LC-MS/MS and MALDI-IMS methods

OLZ			
ng/mg	**2h**	**6h**	**12h**
LC*	57.30	3.74	2.64
MALDI*	55.65	4.89	2.30
% difference	3	24	13

*Average RSD=33%

Materials and Methods

Materials

The MALDI matrices, 3,5-dimethoxy-4-hydroxycinnamic acid (sinapinic acid, SA), α-cyano-4-hydroxycinnamic acid (CHCA), and 2,5-dihydroxybenzoic acid (DHB), were purchased from Sigma Chemical Co. (St. Louis, MO) along with sodium hydroxide and ammonium acetate. HPLC grade acetonitrile, methanol, and hexane were purchased from Fisher Scientific (Suwanee, GA). HPLC grade cyclohexane was purchased from Acros Organics (Geel, Belgium). Fischer 344 rats were purchased from Charles River Laboratory, Inc. (Wilmington, MA). Zyprexa tablets (OLZ) were obtained from the Vanderbilt University Hospital Pharmacy (Nashville, TN). All animal studies were approved by the Institutional Animal Care and Use Committee at Vanderbilt University.

Animal Dosing Methods

OLZ was administered per oral (p.o.) at pharmacologically relevant doses of 8 mg/kg to 10 week-old male Fischer 344 rats, which had fasted overnight prior to start of study. Animals were euthanized at 2h, 6h and 12h post-dose by isoflurane anesthesia followed by exsanguination via decapitation. Control and dosed brain, liver, and kidney were harvested and frozen in powdered dry ice.

Signal Depth Methods

Fresh frozen tissue sections at 12 µm thickness were collected at -20 ºC using a Leica CM3050s cryomicrotome (Leica Microsystems, Inc., Germany) and thaw-mounted to gold-coated MALDI target plates. Sections were acquired for Olanzapine dosed rat brain. Target plates were stored in a dessicator until analysis. Matrix solution was made fresh at 40 mg/ml DHB in a 50% methanol solution and spiked with 2 µM of d4-olanzapine. The matrix solution was spotted onto the tissue sections on the Portrait™ 630 (Labcyte Inc.) depositing a total of 6.8 nl (40 passes, 1 drop/pass, 170 pl/drop) in a 300 µm x 300 µm spatial resolution array. Photos were acquired for the spotted tissue sections using an Olympus BX50 microscope (Olympus Optical Co, LTD. Tokyo, Japan,) fitted with a Micropublisher 3.3 camera (QImaging, Canada) at 10x magnification. Once spotting was completed the plates were allowed to dry in the dark for a minimum of 15 minutes before being introduced into the MALDI LTQ XL (Thermo Scientific Inc.). Spectra were acquired across the array in a total of 7-14 locations per matrix spot to get an accurate representation of the signal distribution across the entire area. At each position spectra were acquired at 45 laser shot intervals (3 µscans/step, 15 laser shots/µscan) or at 15 laser shot intervals (3 µscans/step, 5 laser shots/µscan) with a 20 µJ laser energy. Spectra were acquired at the same absolute x and y coordinate location until no signal was detected. Spectra were introduced to in-house software designed by Surendra Dasari (Frappienator) to export the absolute x and y coordinates along with the total signal intensity for a specific m/z for each spectra acquired and the information was put into an excel spreadsheet for further statistical analysis.

Area Ablation Calculation Methods

A gold coated MALDI target was covered with a thin layer of DHB matrix by sublimation using an in-house built sublimination chamber. Once coated the plate was introduced into the MALDI LTQ XL (Thermo Scientific Inc.) for laser spot size analysis. The laser was positioned over an area of the plate with the DHB matrix and then fired at specified laser powers and raster patterns typically used for acquiring data. The plates were then taken to an Olympus BX50 microscope (Olympus Optical Co, LTD. Tokyo, Japan,) fitted with a Micropublisher 3.3 camera (QImaging, Canada) at 10x magnification and pictures were acquired at 10x magnification. Using the microscope software, Image-Pro Plus, the dimensions of the laser spot burn patterns were measured to determine the size of the laser spots.

Tissue Dimension Calculation Methods

Fresh frozen tissue sections at 12 µm thickness were collected at -20 ºC using a Leica CM3050s cryomicrotome (Leica Microsystems, Inc., Germany). One section was thaw mounted to a glass slide while ten subsequent sections were collected on a previously weighed piece of wax coated weigh paper. The ten sections were immediately weighed on a micro balance to get their mass. The weight of the weigh paper was subtracted from the total mass. This process was repeated five times for each tissue evaluated and the average mass of a tissue section was calculated. The sections on the slides were stained with cresyl violet and cover slipped. The stained slides were allowed to dry and then images were acquired on a flat bed scanner at 3200dpi next to a measurement slide. The images were imported into Adobe Photoshop software. Using the marquee tool make a rough selection of the area of interest. Open the color range tool. Using the Select Drop Down Menu and select Color Range. Once the dialogue box is open, make sure the radio dial box is checked selection and the selection preview is set to Black Matte. Hold down the shift button and select the various color regions needed for area calculation. Use the Fuzziness toolbar by sliding to the right to adjust until all areas to be used for the calculation are selected without any unwanted areas showing in the preview window. Finalize the selection by clicking OK. Now that the area has been selected it is necessary to find the number of pixels within the selection. This can be done using the Histograms, located in the palates toolbar on the right hand side of the screen. Make sure the view is in expanded mode and the show statistics button is also selected. Number of pixels can be found in the lower left hand corner of the statistics display. Occasionally the histrogram will show an error icon indicating that it needs to be refreshed to calculate the pixels with uncached data. Do this by clicking the refresh button in the upper right hand corner of the histogram dialogue box. This must be done to ensure that an accurate pixel count is obtained. Take note of the number of pixels selected. In order to convert the number of pixels into actual units, it is necessary to find the number of pixels within an object in the image for which the actual real life dimensions are known. Using the marquee tool, select the area of known dimensions as accurately as possible. Go back to the Histograms box and obtain the number of pixels. Now you can use the information to convert the number of pixels to physical units. Divide the number of pixels within the unknown area of interest by the number of pixels within the area of known dimensions. Multiply by the known dimension. This results in the exact physical measurement for the area of interest.

Limits of Detection and Calibration Curve Methods

A dilution series of OLZ stock solutions was made in 100% methanol and stored at -20°C until use. The series spanned six orders of magnitude (1 ng/ml, 10 ng/ml, 100 ng/ml, 1000 ng/ml, 10,000 ng/ml, 100,000 ng/ml) to allow for accurate limit of detection determination. From these stock solutions a standard series was made by adding known amounts into already prepared matrix (DHB 40 mg/ml, 50 % methanol: 50% water). One hundred µl of the appropriate stock was added to 900 µl of matrix to make the following dilution series: 0.1 ng/ml, 1 ng/ml, 10 ng/ml, 100 ng/ml, 1,000 ng/ml and 10,000 ng/ml. To each solution the appropriate internal standard was added to a 2 µM concentration.

Fresh frozen tissue sections at 12 µm thickness were collected at -20 ºC using a Leica CM3050s cryomicrotome (Leica Microsystems, Inc., Germany) and thaw-mounted to gold-coated MALDI target plates. Sections were acquired for Fisher 344 rat brain. Plates were put into a dessicator to dry for a minimum of 60 minutes. After drying, the plates were spotted with the standard spiked matrix dilution series on the acoustic reagent multi-spotter (Portrait™ 630, Labcyte Inc.) 6.8 nl per spot (40 passes, 1 drop/pass, 170 pl/drop) in a 300 µm x 300 µm spatial array resulting in a 20 x 10 spot array for each standard solution. The plates were allowed to dry in the dark for 15 minutes before being introduced into the MALDI LTQ XL (Thermo Scientific Inc.) where spectra were acquired. The acquisition method used a 50 µm raster at 14 different positions across the matrix spot, 2 scan events (one for the analyte, one for the internal standard) alternated for a total of 40 scan events per position, 3 µscans per scan event, 5 laser shots per µscan at a laser power of 20 µJ.

Dosed Tissue Analysis

Fresh frozen tissue sections at 12 µm thickness were collected at -20 ºC using a Leica CM3050s cryomicrotome (Leica Microsystems, Inc., Germany) for each OLZ dosed brain. Plates were put into a dessicator to dry for a minimum of 60 minutes. After drying, the plates were spotted with DHB matrix (40 mg/ml, 50% MeOH) spiked with 2 µM of d4-OLZ as an internal standard on the acoustic reagent multi-spotter (Portrait™ 630, Labcyte Inc.) 6.8 nl per spot (40 passes, 1 drop/pass, 170 pl/drop) in a 300 µm x 300 µm spatial array resulting in a 20 x 10 spot array. The plates were allowed to dry in the dark for 15 minutes before being introduced into the MALDI LTQ XL (Thermo Scientific Inc.) where spectra were acquired. The acquisition method used a 50 µm raster at 14 different positions across each matrix spot, 2 scan events (one for the analyte, one for the internal standard) alternated for a total of 40 scan events per position, 3 µscans per scan event, 5 laser shots per µscan at a laser power of 20 µJ.

Drug Quantitation Using LC-MS/MS

The extraction protocols used here were modeled after published protocols of OLZ quantitation from dosed tissues.[65-67] For each tissue being evaluated a piece of the tissue was cut and then weighed with a minimum of 100 mg used, this was done in triplicate. Once the tissue was weighed it was homogenized with water, 1 ml for every 100 mg of tissue used, and 3 µg of the internal standard being used. The tissue was homogenized thoroughly until uniform by visual inspection and then the liquid was transferred to a test tube using a Pasteur pipet. A 1:1 dilution of sodium hydroxide was added to the tube and the solution was vortexed to pH the solution. For the extraction, ten ml of cyclohexane was added to the test tube and then mixed by inversion for two hours. The mixture was then centrifuged for 30 minutes at 3500 rpm. The organic layer was removed and transferred into a scintillation vial which was then dried under Nitrogen gas at 37 °C. Samples were reconstituted in 300 µl of 10mM ammonium acetate in 50% acetonitrile and then transferred to autosampler vials. Standard curves were prepared by spiking a control homogenate with the OLZ standard, which covered a concentration range of 1-1000 ng/g.

Samples were analyzed on an ESI TSQ Quantum triple-quadrupole system (Thermo Scientific, Waltham, MA) equipped with an autosampler (set at 4 ºC) and HPLC system. A C12 Synergi MAX-RP 150 x 2 mm column (Phenomenex, Torrance, CA) was used with a fast gradient run of mobile phase A (5:95 acetonitrile:0.5% acetic acid in water, 10 mM ammonium acetate) to mobile phase B (95:5 acetonitrile:0.5% acetic acid in water, 10 mM ammonium acetate).

Acknowledgements

Dr. Surendra Dasari and Dr. David Tabb developed the in-house software (Frappienator) used to export the intensities from the MALDI LTQ XL data.

CHAPTER III

ANALYSIS OF IMATINIB TREATED GL26 MURINE CELL XENOGRAFTS

Overview

Glioblastoma multiforme (GBM) is the most common type of malignant primary brain tumor with over 10,000 new cases diagnosed each year in the United States.[68] Glioblastomas account for approximately 60 to 70% of malignant gliomas, anaplastic astrocytomas for 10 to 15%, and anaplastic oligodendrogliomas and anaplastic oligoastrocytomas for 10%; less common tumors such as anaplastic ependymomas and anaplastic gangliogliomas account for the rest.[68] Despite current methods of therapy including surgery, radiation and chemotherapy the median survival for GBM is only 12-18 months. However, with recent progress in understanding the molecular pathways of this disease it is becoming possible to generate new and better therapies for treatment of GBM. Malignant transformation in gliomas is the result of sequential accumulation of genetic aberrations and deregulation of growth factor signaling pathways. Targeted therapies have been developed against these pathways.[69] Targeted therapy may provide greater specificity toward tumor cells with potentially less toxicity than conventional chemotherapy. The success of these agents in other systemic cancers demonstrates their potential in tumors with well-defined molecular targets.[70, 71] Even though the complexity of the molecular abnormalities in GBMs and the redundancy of the signaling pathways make it unlikely that single agents will achieve great success, there has been significant interest in this approach.

Inhibition of deregulated protein kinases by small molecule drugs has evolved into a major therapeutic strategy for the treatment of human malignancies. Knowledge about direct cellular targets of kinase-selective drugs and the identification of druggable downstream mediators of oncogenic signaling are relevant for both initial therapy selection and the nomination of alternative targets in the event that molecular resistance emerges. Protein kinases are critical regulators in human cancer and play major roles in tumor cell proliferation, migration and survival. Aberrant kinase activity has been identified as a major factor contributing to disease progression in various human malignancies. The targeted inhibition of protein kinases has therefore emerged as a major therapeutic approach and fueled the development of various kinase-selective drugs, such as cell-permeable small molecule inhibitors, with the potential to address currently unmet medical needs in cancer therapy.

In this project, we now seek to detect the quantitative distribution of the targeted molecular therapy Imatinib (IMAT) and to define the biological mechanisms that govern the ability of molecular targeted therapies to induce death of tumor cells in the brain. The results of these studies will assist us in improving and validating future molecular targeted therapies for malignant brain tumors.

Introduction

PDGF in Gliomas

Tyrosine kinases are a group of protein kinases critical to signal transduction pathways involved in cell proliferation, growth, survival, adhesion, motility and differentiation. The group includes receptor tyrosine kinases (RTKs) which are transmembrane proteins containing an extracellular binding domain that binds ligands and an intracellular kinase domain that activates intracellular signaling pathways. Platelet derived growth factor (PDGF) is a member of this family and induces cellular growth, proliferation and differentiation by activating intracellular signaling mechanisms via platelet derived growth factor receptor (PDGFR).[72] PDGF consists of a dimer of two polypeptide chains, A and B with a 60% homology. They can assemble as a heterodimer (PDGF-AB) or homodimers (PDGF-AA or PDGF-BB). The receptors are membrane glycoproteins expressed in several tissue cells and consist of two subunits α and β encoded by two different genes.[73, 74] There are also more rare forms of PDGF being C and D.[75] All forms of PDGF and PDGFR have been found to be overexpressed in human brain tumors such as menigiomas, astrocytomas, oligodendrogliomas, medulloblastomas, and ependymomas and are associated with the more malignant tumors.[72, 74, 75] Because of the numerous genetic and physiological alterations observed in human glioma the importance of PDGF signaling is still not fully understood. But PDGF autocrine loops are thought to both initiate and sustain the transformed phenotype of glioblastoma cells.[76] This notion has experimental support. Glioma-like tumors can be induced in mice after overproduction of PDGF in mouse brain. Also, some glioma-derived cell lines have been blocked by interference with PDGF receptor signaling.[77]

Imatinib

Imatinib is a small molecule drug used for the treatment of some cancers. It is known to inhibit PDGFR-α, PDGFR-β, Bcr-Abl, c-Fms, and c-kit tyrosine kinases.[78] As described in the previous section dysregulated PDGFR kinase activity has been linked to a variety of cancers, including glioblastoma. [72, 74, 75] IMAT has been shown, in animal models, to enhance the antitumor effects of chemotherapeutic agents due to inhibition of PDGFR phosphorylation and therefore may have potential efficacy as an adjuvant therapy.[79] The mechanism of action is thought to be growth delay through growth arrest in the G_0-G_1 phase rather than inducing apoptosis. IMAT inhibits the autocrine PDGFR stimulation which leads to decreased cell population.[76, 79]

Use of Animal Models

In order for scientists to fully understand how cancers develop, spread through the body and discover new and effective ways of diagnosis and treatment, it is necessary to carry out research on live animals. Animal studies are essential to understand the complexities of the biological processes that are involved in cancer within living organisms. They are also required before any trials for new drugs can begin in humans. While the use of nonhuman animal models is a common component of biomedical research, the role of animal models in research, its scientific and ethical justification and legal regulations and policies need to be considered before any project can begin.[80, 81] Approval and animal protocols must be submitted and approved by the Institutional Animal Care and Use Committee (IACUC).[82] Careful consideration also needs to be taken to ensure that the animal model selected will biologically represent the disease or condition that you are investigating.

When designing a MALDI IMS experiment it is important to select the proper small animal model. In the early phases of drug discovery and development, therapeutic candidates cannot be administered to humans, and therefore, predictions about the PK/PD properties have to be made from an *in vivo* animal model. The two most common species include rats and mice, which have different metabolic rates and pathways; hence providing vastly different metabolite and distribution information. In general, rats are used for PK/PD studies due to their similarity to human pathways to determine the ADME of an administered pharmaceutical. In other cases, mice may be preferred, since many more models of disease are available in mice rather than rats.[83] Taking all of this into consideration a syngenic mouse GL26 glioma model was chosen. It has been shown that GL26 experimental murine gliomas share most characteristic histological features with human gliomas.[84]

Results

Animal Implantation and Drug Dosing

To start the study two sets of mouse implantations and drug dosing were done. One set was used to evaluate the effects of chronic dosing of the imatinib. For this set of experiments 25 mice were implanted with GL26 cultured tumor cells and tumor growth was allowed to occur for 12 days. (Extra mice were implanted to take into account any casualties.) On day 12 the IMAT treatments began and continued for six days. Group one was the control group dosed once a day for six days with saline solution (p.o.). Groups two through five were dosed once a day with 100 mg/kg IMAT (p.o.) for 1 day (1d), 2 days (2d), 4 days (4d) and 6 days (6d) respectively. Twenty-four hours after the final dose the mice were sacrificed, the brains were excised, immediately flash frozen in liquid nitrogen and stored at -80 °C.

The second set of mice was to evaluate the effects of a single imatinib dose over time. Five groups of five mice each were evaluated for a treatment response. 30 mice were implanted with GL26 murine tumor cells and tumor growth was allowed to occur for 12 days. (Extra mice were implanted to take into account any casualties.) On the 12th day mice were given a single dose of 100 mg/kg IMAT (p.o.) and then sacrificed in groups according to the time point they would represent. Groups were sacrificed 2 hours (2h), 6 hours (6h), 12 hours (12h) or 24 hours (24h) after the administration of the IMAT dose. Control mice were sacrificed 24 hours after a dose of saline solution (p.o.). The brains were excised and immediately flash frozen in liquid nitrogen and stored at -80 °C.

Drug Detection and Quantitation

When deciding to use a treatment for a particular disease, one of the most important things to investigate is whether or not the compound is getting to the area that needs to be treated. To this end, the distribution of IMAT was determined in tumor bearing mouse brain tissues to elucidate if the drug was penetrating through the Blood Brian Barrier (BBB) or the Blood Tumor Barrier (BTB). The BBB is the bottleneck in brain drug development and is the single most important factor limiting the future growth of neurotherapeutics.[85]

Sections for analysis were cut on a cryostat at 12 µm and then prepared for MALDI IMS accordingly by applying DHB matrix with d8-IMAT internal standard using a Portrait™ 630 (Labcyte Inc). All sections were analyzed on a MALDI LTQ XL

(Thermo Scientific, Inc.) monitoring the major collision induced fragment of IMAT at *m/z* 394.1. To display the images, the data was input into Biomap and then normalized to the d8-IMAT internal standard by taking the ratio of the IMAT signal over the d8-IMAT signal at each location. IMAT signal was detected very strongly from the tumor area of the mouse brain with much less signal coming from the normal brain tissue (Figure 15). The MALDI images are shown in the grey boxes and below are the scanned images of Hemotoxylin and Eosin (H&E) stained serial sections of mouse brain tissue. These images show that the IMAT is penetrating into the brain mainly in the tumor region.

Various tissue types can have different ionization effects, so to determine if the image results were an effect of differing ionization efficiencies standard solutions were analyzed on both the normal and tumor tissue types. DHB matrix was made in 50% methanol with 2 µM of d8-IMAT as an internal standard. IMAT standard was then spiked into aliquots of the matrix resulting in concentrations of 10000 ng/ml and 1000 ng/ml. The spiked matrix was spotted on both the tumor bearing portion of a non-dosed brain and also the non-tumor bearing areas of the tissue resulting in matrix spots that contained 68000 fg of IMAT and matrix spots with 6800 fg of IMAT. Spectra were acquired from each of the spots and the intensities were recorded. There was not a significant increase or decrease in the control or tumor regions intensities for the IMAT or d8-IMAT signals and no significant differences of the IMAT/d8-IMAT ratios. The percent difference between standard intensity ratios from the tumor and normal regions was below 5%. Table 2 shows the IMAT/d8-IMAT ratio averages taken from the matrix spots containing either 68000 or 6800 fg of IMAT. Both the tumor and normal regions show the same ionization efficiency for the IMAT signal. These results indicate that the signal differences seen between the tumor and normal areas of the dosed brain images are not due to a difference in ionization effects of the tissue but are true differences in the amount of IMAT present in the tissues.

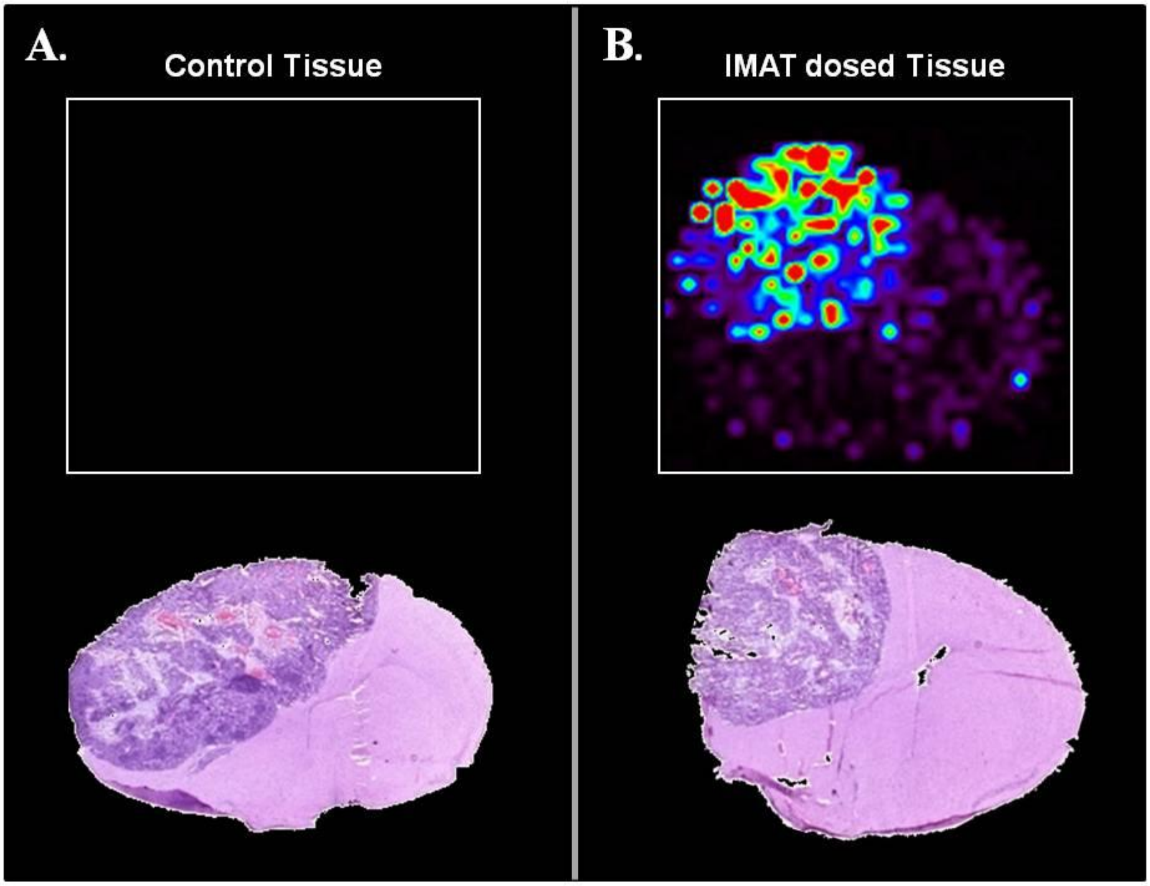

Figure 15: IMAT images taken on a MALDI LTQ XL monitoring for CID fragment *m/z* 394.1. A) A tumor bearing mouse brain dosed with a saline solution. The grey box contains the MALDI image and below is an H&E stained section of the mouse brain. B) A tumor bearing mouse brain dosed with IMAT. The grey box contains the MALDI image and below is an H&E stained serial section of the mouse brain.

MALDI images were acquired for each of the brains within the respective dosing groups. For the acutely dosed mice it can be seen that the IMAT signal is strong at 2h post dose in the tumor regions and is at its highest concentration 6h post dose. From there the amount of detected IMAT decreases at the 12h and 24h post dose time-points as

Table 2: IMAT/d8-IMAT signal ratios taken from standards spotted on tumor and normal tissues within a mouse brain

	68,000 fg of IMAT	6,800 fg of IMAT
Normal	22.29 ± 0.69 %RSD=3.12	2.69 ± 0.07 %RSD=2.64
Tumor	21.19 ± 0.91 %RSD=4.32	2.66 ± 0.10 %RSD=3.78
% Difference	4.9	1.1

seen in Figure 16. For the chronically dosed samples the amount of detected IMAT is relatively constant in the normal regions of the brain tissue but there is an increase of IMAT signal in the tumor region after 4d and 6d of continued treatment shown in Figure 17.

With the images providing a qualitative assessment for the amount of IMAT present in each of the dosing groups, experiments needed to be performed to quantitatively assess the absolute IMAT concentration in the brain tissues. This was accomplished by following the MALDI quantitation protocol developed in Chapter II and outlined in Appendix A. First 12 µm sections were collected from each brain and weighed on a microbalance immediately following sectioning. A 12 µm GL26 implanted brain section had an average mass of 0.64 mg with an 8% RSD. Brain sections were then stained and scanned using a flatbed scanner at 3200 dpi to provide images for tissue area

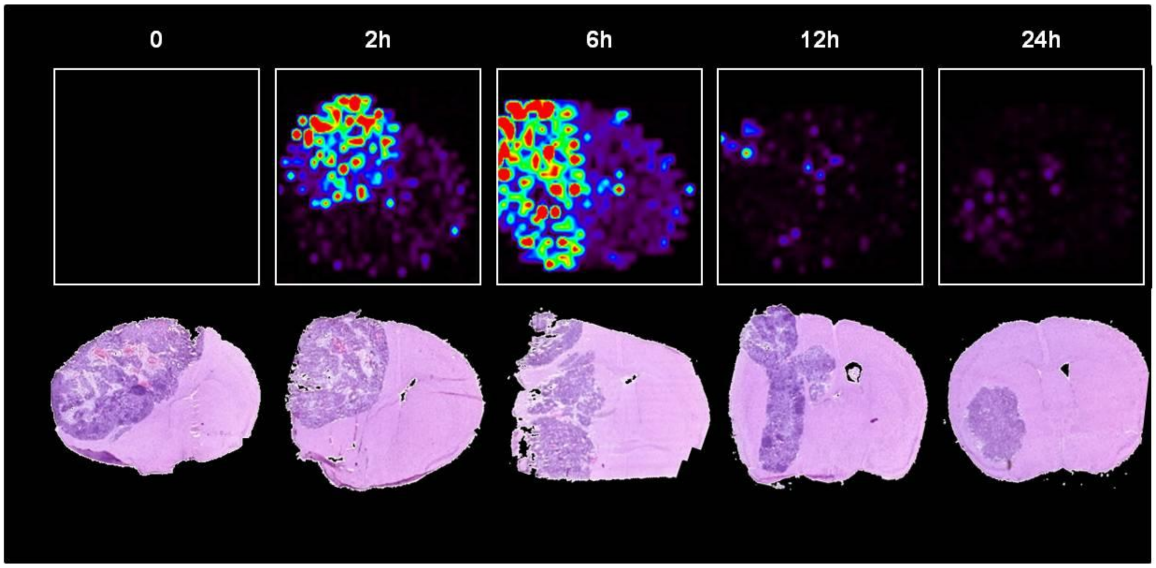

Figure 16: Imatinib images for the acutely dosed mouse brain samples. The top-most row shows the imatinib distribution for a representative brain at each acute time-point (images acquired on the Thermo MALDI LTQ). The bottom row displays the H&E stained section for the representative brains.

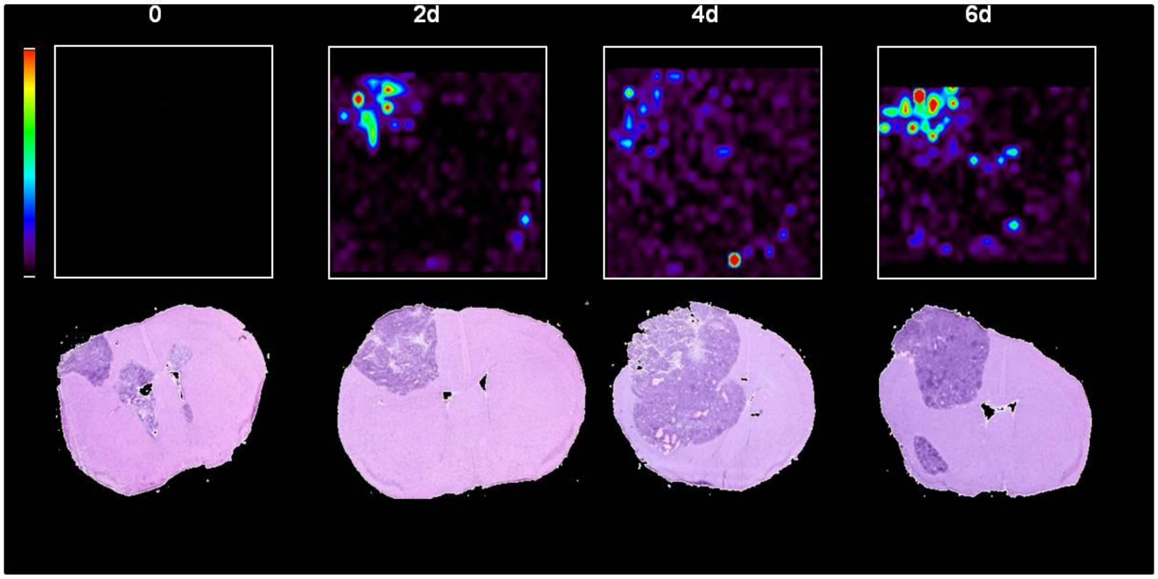

Figure 17: Imatinib images for the chronically dosed mouse brain samples. The top-most row shows the imatinib distribution for a representative brain at each chronic time-point (images acquired on the Thermo MALDI LTQ). The bottom row displays the H&E stained section for the representative brains.

calculation. The images were imported into Adobe Photoshop and the area of a 12 µm GL26 implanted brain section was determined to be 62.37 mm^2 with a 0.6% RSD. The area of the laser to be used for spectra acquisition was determined to be 0.0035 mm^2 (Chapter II) and using this information the amount of tissue sampled within one laser position can be calculated: 62.37 mm^2/0.64 mg = 0.0035 mm^2/ X mg. The amount of tissue sampled is $3.59x10^{-5}$ mg. Next, a calibration curve of IMAT was constructed. Matrix solutions were spiked with IMAT to yield final concentrations of 100, 10, 1, 0.1 ng/ml along with 2 µM of d8-imatinib as the internal standard. Using the Portrait™ 630, matrix was deposited onto non-dosed brain tissue sections in known volumes resulting in 680, 68, 6.8 and 0.68 fg of IMAT along with a blank standard of matrix only with internal standard. Spectra were acquired from each of the spots, using 600 laser shots per position and 14 positions per matrix spot. This totaled 140 different laser positions for each standard due to the fact that ten matrix spots per calibration standard were analyzed. For each matrix spot the total signal of the IMAT and the d8-IMAT was summed using in-house software (Frappienator) and the ratio of IMAT/d8-IMAT was taken. The ratios for each calibration standard were plotted and a linear fit was calculated. Each point on the curve had a RSD no higher than 25% and the curve had excellent linearity with an R^2 value of 0.9996 as shown in Figure 18. From this curve, the LOD of imatinib with this acquisition method by MALDI, was determined to be approximately 20 ng/g of tissue.

IMAT dosed tissue sections were cut for each brain and spotted with DHB in 50% methanol spiked with 2 µM of d8-IMAT as an internal standard. From each dosed section 140 positions were analyzed totaling 5600 spectra for each brain. The average ratio of IMAT/d8-IMAT signal was taken for each time-point and plugged into the

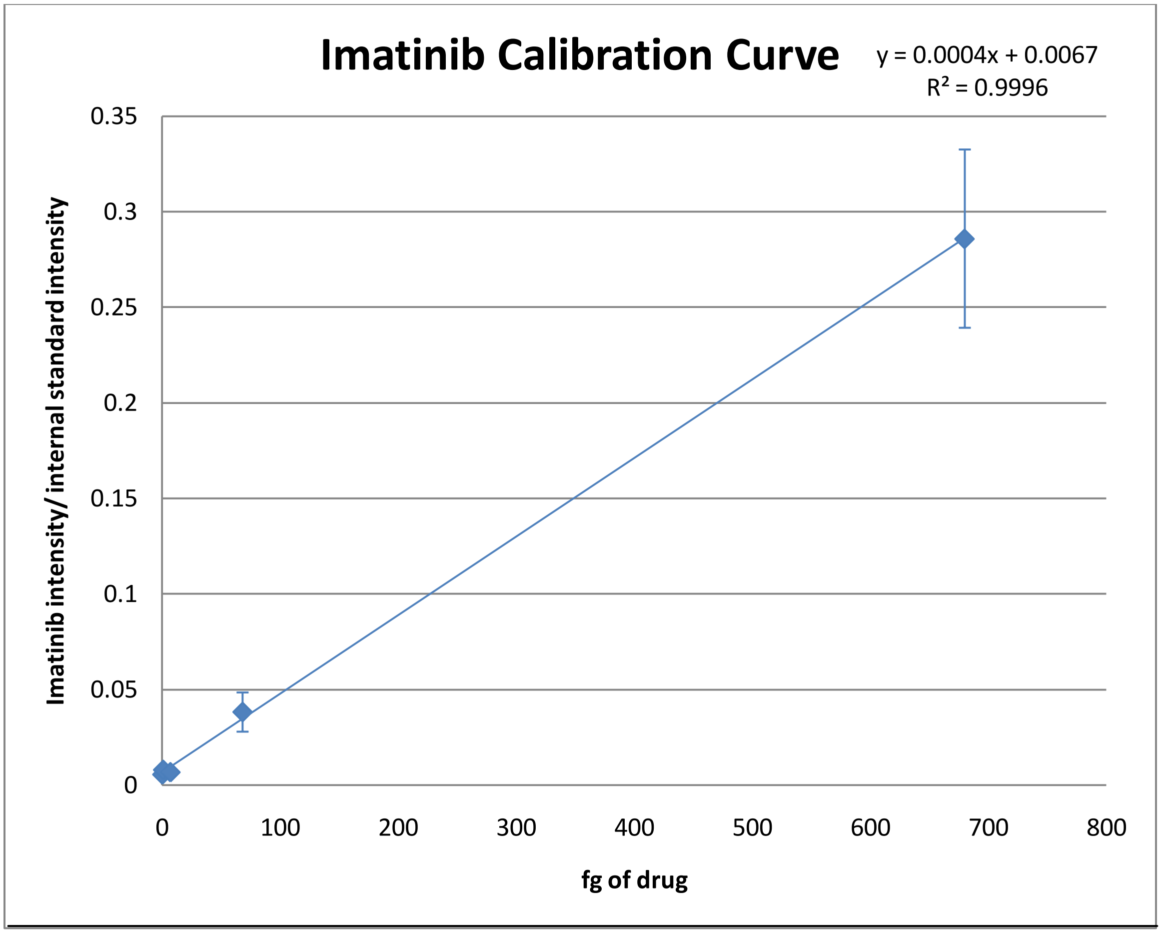

Figure 18: Imatinib Calibration Curve obtained using MALDI IMS Methods

calibration curve equation to calculate the average amount of IMAT present in fg. Dividing this value by the amount of tissue sampled gives the IMAT concentration for each of the dosed tissues in ng of IMAT within 1 g of tissue. Table 3 shows the concentration values calculated for the 2h, 6h, 12h, 24h, 2d, 4d and 6d mice in both the tumor and normal regions of the brain. Results show good reproducibility with a RSD no higher than 15% for the normal tissue samples analyzed. The tumor tissue region showed a bit more variability with an RSD no higher than 30%. This is most likely due to the

Table 3: Imatinib concentrations calculated by MALDI-IMS Methods

ng/g	2h	6h	12h	24h	2d	4d	6d
Normal	595.35	773.90	546.84	496.72	499.42	514.27	496.38
% RSD	6	8	3	2	9	15	6
Tumor	12255.82	53826.45	6936.43	546.59	572.20	1940.11	1651.40
% RSD	32	27	36	9	6	27	4

fact that the tumor bearing area of the brain is much more heterogeneous than the normal area. Gliomas are known to be heterogeneous both phenotypically and genotypically.[86-88]

Traditional drug quantitation techniques requiring homogenization and extraction followed by analysis on a LC-triple quadrapole system were also performed on the tissues. The calibration curve for this experiment was constructed using an IMAT concentration range from 10 to 3000 ng/ml and the response curve was generated using a weighted (1/x) least-squares linear regression model. The measurement of IMAT was linear with respect to concentration across a minimum of three orders of magnitude with an R^2= 0.9992. The LOD for imatinib was 1 ng/ml of tissue homogenate. The recovery of imatinib extraction was estimated to be around 80% as demonstrated in previous studies.[89, 90] Samples of tissue from both tumor and normal tissues of the brain for each dosing group were prepared and then analyzed. Using the response curve, average imatinib concentrations were found for each dosing group and are shown in Table 4. As with the MALDI results, the RSD for the normal samples was around 15% and the tumor samples around 30%, again speaking to the higher heterogeneity of the tumor tissue.

Table 4: Imatinib concentrations calculated by LS-MS/MS Methods

ng/g	**2h**	**6h**	**12h**	**24h**	**2d**	**4d**	**6d**
Normal	542.31	710.48	401.92	355.26	240.54	357.12	361.32
% RSD	11	6	14	16	8	16	16
Tumor	6099.49	11632.86	1492.48	243.34	377.72	733.95	570.20
% RSD	33	5	9	35	15	6	11

The quantitation results for both the MALDI and the LC methods were plotted on a line graph for comparison. Figure 19 shows the IMAT concentrations in ng/g (ng of IMAT per g of tissue) for the acutely dosed mouse groups, 2h, 6h, 12h and 24h. The blue trace represents the results obtained by LC-MS/MS and the red trace represents the results obtained by MALDI-IMS. The tumor tissue results are plotted on a graph separately (top graph) from the normal tissue results (bottom graph). The values calculated using the MALDI method are higher in all instances than the values calculated using the LC method with a percent difference between the two methods as low as 30% for the tumor samples and 8% for the normal samples. Figure 20 shows the IMAT concentrations in ng/g (ng of IMAT per g of tissue) for the mice dosed chronically, 1d, 2d, 4d, and 6d. The tumor (top graph) and normal (bottom graph) results are plotted separately with the blue trace representing the LC-MS/MS results and the red trace representing the MALDI-IMS results. Here again the MALDI results are all higher than those of the LC results. Across all of the samples the average percent difference between the two methods is 40% with the results from the MALDI being higher in all instances. Looking at the plotted data, the MALDI and LC results follow the same trends of drug concentration across the different dosing groups.

Proteome Response Study

In order to evaluate for a pharmacodynamic response to the imatinib presence in the tumor bearing portion of the brains, each brain was imaged by MALDI-TOF MS. Standard MALDI imaging preparation steps were employed to get the samples ready for analysis. Samples were cut on a cryostat, thaw mounted onto target slides, dried and then matrix application was performed on a Portrait™ 630 spotter before imaging on a Bruker Autoflex TOF MS. Three sections were analyzed for each brain and sample acquisition was randomized to eliminate bias. Serial sections were cut for each brain and stained according to a standard cresyl violet staining protocol. These stained sections were

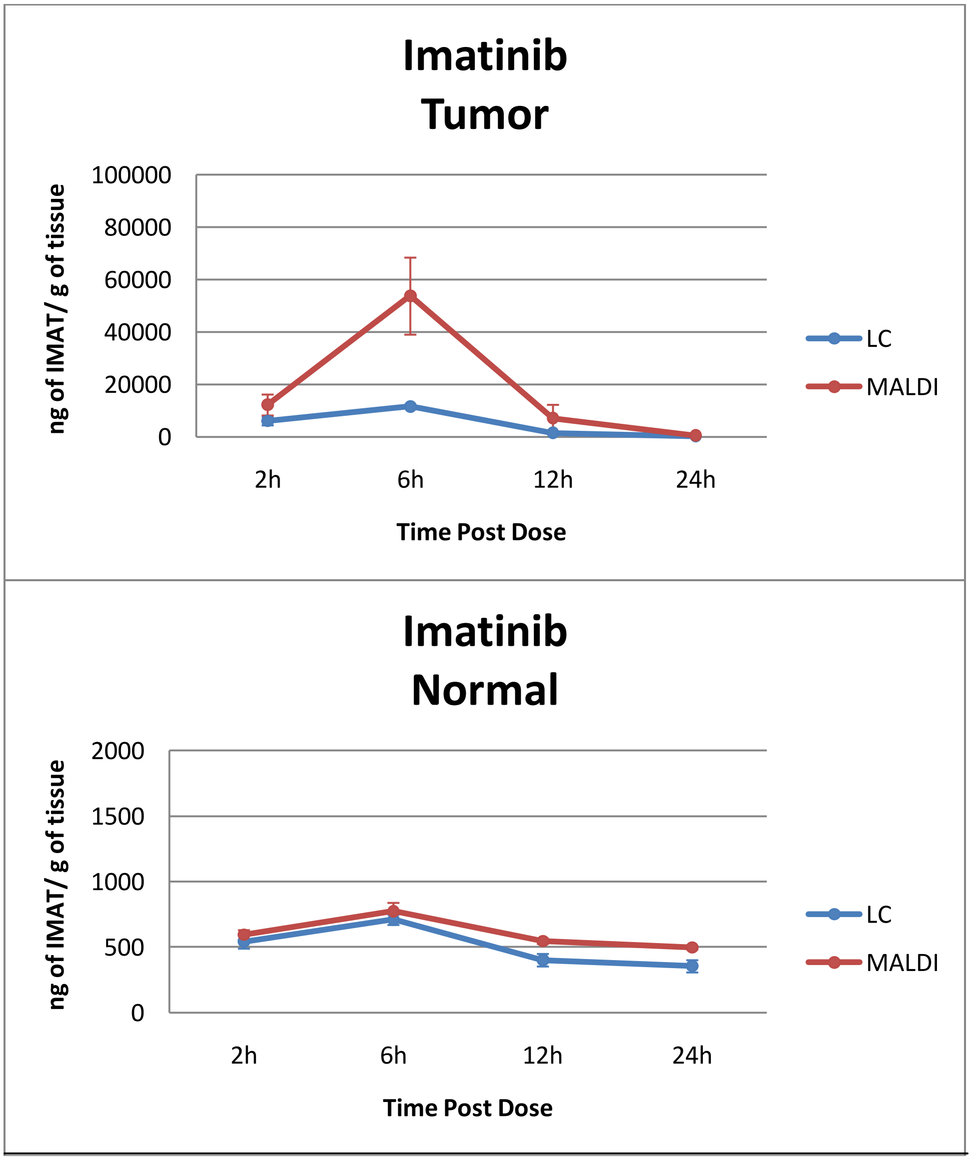

Figure 19: Imatinib quantitation results in ng/g for the acutely dosed mice. The blue trace represents the results obtained by LC-MS/MS methods. The red trace represents the results obtained by MALDI-IMS methods. The graph on top shows results for the tumor tissue and the graph on the bottom shows results for the normal tissue.

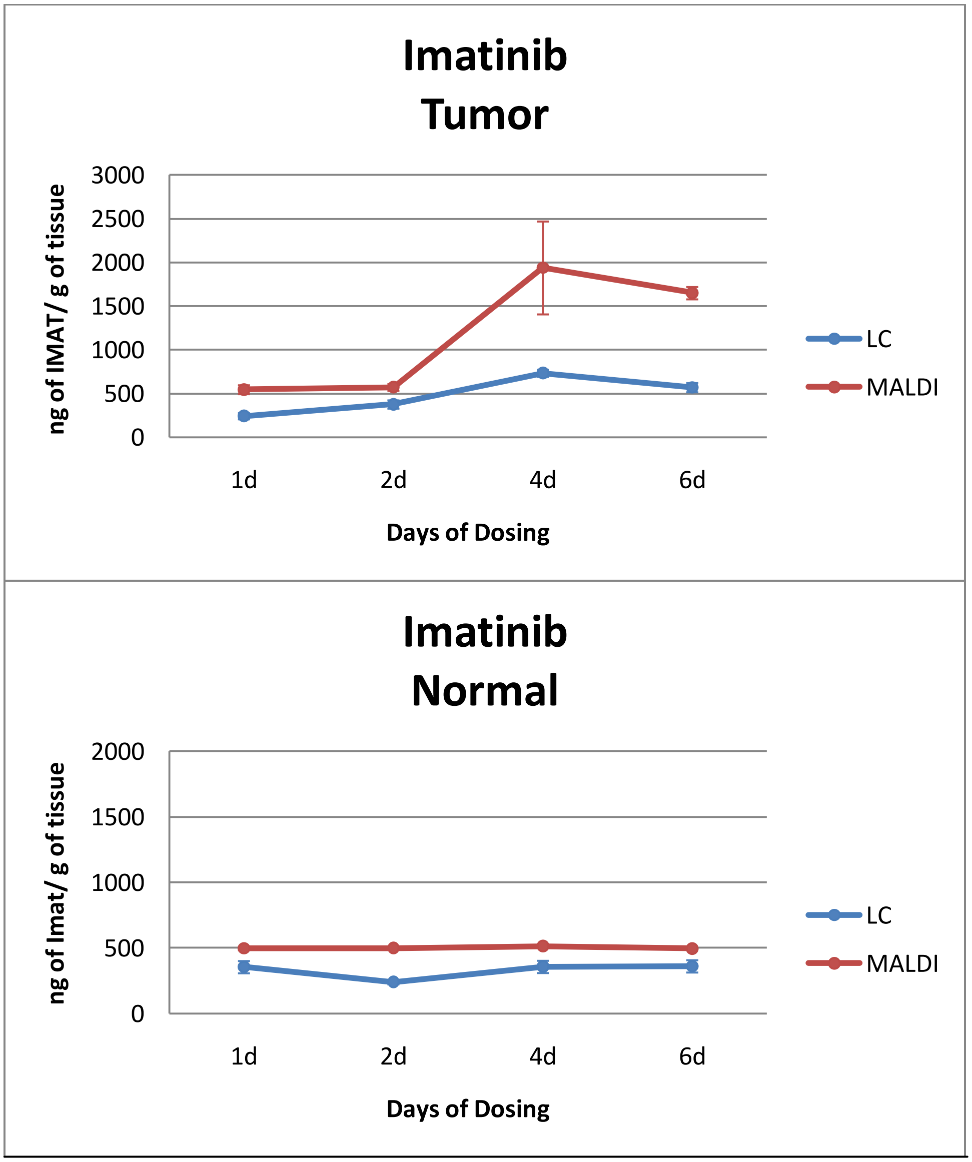

Figure 20: Imatinib quantitation results in ng/g for the chronically dosed mice. The blue trace represents the results obtained by LC-MS/MS methods. The red trace represents the results obtained by MALDI-IMS methods. The graph on the top shows results for the tumor tissue and the graph on the bottom shows results for the normal tissue.

scanned on a Mirax Scanner (Carl Zeiss MicroImaging) and the images were saved. After acquisition of the MALDI images it was possible to import, co-register and overlay the stained image with the MALDI image and optical image of the spotted section using Flex Imaging software (Bruker Daltonics, Germany). This allowed for the visualization of all the MALDI images and for spectra from specific regions in the brain to be selected and saved into separate folders for further processing and statistical analysis. With the assistance of a neuro-oncologist, the tumor bearing areas of the brain tissue were identified and spectra from these areas were extracted. Figure 21 shows the co-registration and spectra selection process.

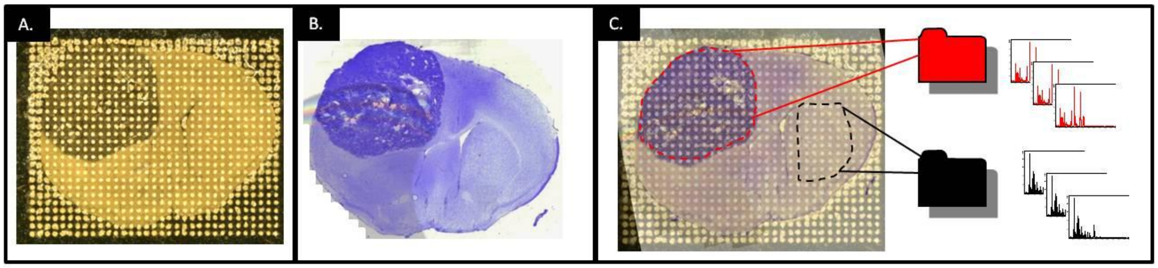

Figure 21: Workflow for extracting regions of spectra from an image data set. A) Optical image of a matrix spotted brain section B) Scanned image of a cresyl violet stained serial brain section C) Co-registrated overlay of the optical and stained image. Red outlined areas indicate where spectra were selected from the tumor region of the brain and put into a folder. Black outlined areas indicate where spectra were selected from the normal region of the brain and put into a folder. These folders of spectra then underwent spectral processing procedures and statistical analysis.

MALDI IMS analysis was performed on a total of 40 brains, with three sections being imaged for each brain. This resulted in 120 sections analyzed and approximately 10,000 spectra acquired. From each brain section 15 or more spectra were selected from the tumor region so that there were a minimum of 45 spectra representing each brain and 225 spectra representing each dosing group.

All spectra were processed using ClinPro Tools, commercially available software from Bruker Daltonics (Germany). Once the spectra had undergone baseline subtraction, smoothing, normalization, realignment and peak picking the data for each spectrum was exported collectively into a feature table (a list of each m/z value and its corresponding intensity value for each spectrum). Using these feature tables, various analyses and statistical tests were performed to evaluate the protein changes that occurred with respect to amount of IMAT present.

The feature tables generated from ClinPro Tools were put into the program MiniTab® (MiniTab Inc., State College, Pennsylvania) to create interval plot of each m/z value as its analyte signal progressed from the dosing group with low drug concentration to the dosing group with the most IMAT presence. Figure 22 shows example interval plots for *m/z* 4195 and 14422. These plots provided a visual inspection of the *m/z* trends as a result of drug concentration. Once imported into MiniTab® and interval plots had been reviewed, one-way analysis of variance (ANOVA) statistical analysis was computed for each *m/z*. An ANOVA algorithm tests the hypothesis that the means of several populations are equal. A one-way ANOVA can be used to tell you if there are statistically significant differences among the level means. The null hypothesis for the test is that all population means (level means) are the same. The alternative hypothesis is that one or more population means differ from the others. ANOVA measures two sources of variation in the data and compares their relative sizes using the F-statistic finding the variance between the groups in relation to the variation within the groups. A

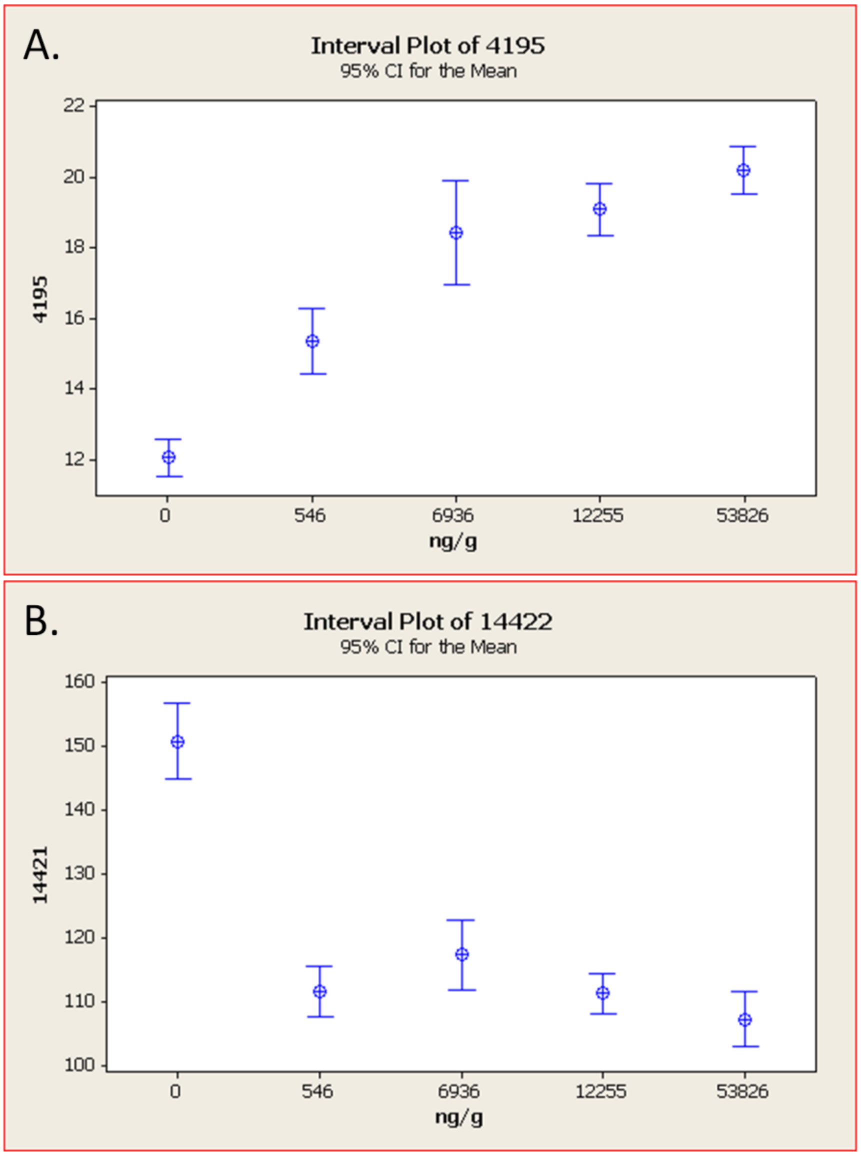

Figure 22: Example Interval Plots created in the MiniTab® software program. A) Interval Plot of *m/z* 4195 demonstrating an increase in signal intensity going from no IMAT presence in the samples to a high concentration of IMAT in the samples. B) Interval plot of *m/z* 14422 demonstrating a decrease in signal intensity going from low to high IMAT concentrations.

large F-value is evidence against the null hypothesis and means more difference between groups that within. The p-value computed denotes the probability that the variation for that group is random. For all experiments a p-value less than 0.05 is considered statistically significant.

Since the ANOVA output only verifies that differences are present between the dosing groups, it does not indicate how these differences are occurring. Differences could be randomized among the dosing groups, or there could be patterns showing a significant increase or decrease associated with IMAT concentration presence. To verify in what order the changes were occurring, the software program Significance Analysis of Microarrays (SAM, Stanford University, California) was used. Two by two comparisons were made between each of the dosing groups in order of least IMAT concentration to most IMAT concentration using a simple t-test for all of the *m/z* values that showed a validated significant ANOVA score.

SAM is a statistical technique for finding significant features proposed by Tusher, Tibshirani and Chu.[91] It uses repeated permutations of the data to determine if the expression of any features is significantly related to the response. The cutoff for significance is determined by a tuning parameter delta, chosen by the user based on the false positive rate. One can also choose a fold change parameter, to ensure that the identified feature change meets a pre-specified amount. The results of these comparisons were used to show which features demonstrated a consistent significant increase in signal in response to IMAT concentration or a significant decrease in signal in response to IMAT concentration. These results were again visually confirmed with the interval plots for each *m/z* value as well as individual spectral analysis from the average traces for each dosing group. Figure 23 shows an overlay of average spectra representing each IMAT treatment group. Inset zoom plots of the spectra show examples of features that either increase or decrease as a result of the IMAT concentration in the tissue.

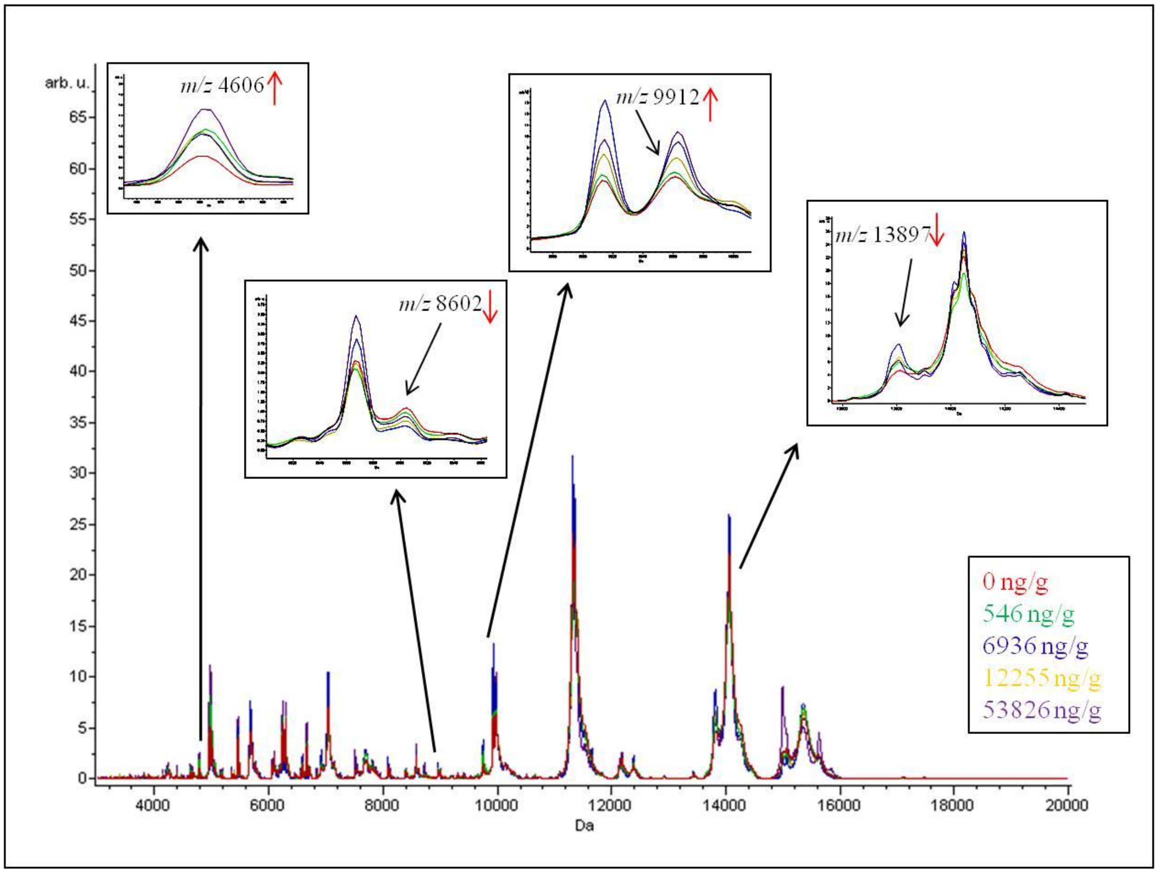

Figure 23: Overlay of average protein spectra from each treatment group at varying concentrations of IMAT. Examples of statistically significant features across the mass range are displayed in the zoom plots with trends indicated by the red arrows next to the *m/z* values.

The statistical methodologies resulted in 99 *m/z* values being found to have either a positive or negative correlation with the IMAT concentration in the brains and 43 of these features showed a significant difference as early as 2h after drug administration across the mass range of (4-30 kDa) as shown in Table 5.

Table 5: Statistically significant features affected by IMAT presence

m/z	**Trend**	**Fold Change**	**SAM score**	**ANOVA p-value**	**ANOVA F Score**	**ANOVA R-Sq**	**AUC**
4195	up	1.7	9.8	< 0.005	48.67	16.54	0.90
4445	up	1.4	3.8	< 0.005	6.09	2.42	0.70
4606	up	2	7.5	< 0.005	17.54	6.67	0.76
4682	up	1.4	7.7	< 0.005	30.07	10.91	0.85
4710	up	1.5	4.6	< 0.005	17.17	6.54	0.85
4768	up	2.1	6.4	< 0.005	14.29	5.5	0.69
4901	up	1.4	4.5	< 0.005	13.41	5.18	0.76
4965	up	1.8	7.7	< 0.005	22.81	8.5	0.73
5143	up	1.6	5.5	< 0.005	16.09	6.15	0.72
5172	up	2.2	6	< 0.005	18.77	7.1	0.71
5445	up	1.4	8	< 0.005	25.71	9.48	0.83
6345	down	1.2	-2.9	< 0.005	41.20	14.37	0.78
6547	up	1.5	7.6	< 0.005	31.99	11.53	0.84
6574	up	1.5	10.7	< 0.005	39.98	10.92	0.91
7108	down	1.3	-7.2	< 0.005	47.15	16.11	0.78
7750	down	1.2	-7.5	< 0.005	64.87	20.9	0.63
7793	up	1.2	6.1	< 0.005	22.18	8.28	0.85
7829	up	1.4	4.1	< 0.005	10.78	4.31	0.75
7858	up	1.3	4.2	< 0.005	18.88	6.76	0.74
7891	up	1.4	5.2	< 0.005	21.26	7.97	0.73
7933	up	1.9	5.9	< 0.005	28.,23	10.31	0.80
8602	down	1.2	-5.3	< 0.005	38.48	13.55	0.66
9071	up	1.3	3.1	< 0.005	18.24	6.92	0.68
9203	up	1.2	3.1	< 0.005	4.40	1.62	0.70
9534	up	1.4	3.2	< 0.005	7.26	2.87	0.73
9638	up	1.2	3.3	< 0.005	17.60	6.69	0.71
9701	up	1.5	5.5	< 0.005	18.38	6.97	0.79
9740	up	1.8	11.9	< 0.005	23.32	8.68	0.92
9777	up	1.2	3.8	< 0.005	32.36	11.65	0.68
9912	up	1.3	7.2	< 0.005	28.20	9.94	0.77
10256	down	1.3	-6.5	< 0.005	19.27	6.9	0.60
10640	up	1.3	3.5	< 0.005	17.06	6.5	0.70
10953	up	1.6	5.7	< 0.005	37.72	13.32	0.74
11309	down	1.2	-7.6	< 0.005	36.72	13.01	0.50
11337	down	1.2	-8.6	< 0.005	56.83	18.47	0.57
11517	down	1.7	-21.7	< 0.005	107.82	30.52	0.96
11841	down	1.3	-5.7	< 0.005	27.19	9.97	0.62
12203	down	1.3	-7.9	< 0.005	69.88	22.16	0.66
12285	down	1.4	-7.7	< 0.005	50.20	16.98	0.75
13897	down	1.3	-8.7	< 0.005	42.31	14.07	0.83
14053	down	1.1	-4.1	< 0.005	8.75	3.44	0.57
14422	down	1.4	-10.8	< 0.005	47.17	16.12	0.73

For the table the first column lists the *m/z* values that were found to be significant followed by the trend up or down relative to the increasing amount of IMAT presence in the second column. The third column lists the fold change which represents the maximum change found between the two group extremes in the data set; between the samples with no IMAT presence and the samples with the maximum amount of IMAT presence in the tissues. This value was calculated by the SAM analysis along with a SAM score which is shown in column four. The score assigned to each m/z value was based on the change in expression relative to the standard deviation of repeated measurements. It is the standardized change in expression. A positive SAM score means that there is an increase of the signal going from group one to group two, the opposite is true for a negative SAM score.

The next three columns list the results from the ANOVA test. The p-value computed denotes the probability that the variation for that group is random. For all experiments a p-value less than 0.05 was considered statistically significant. The F-Score represents the results from the F-statistic stating that there was more difference between groups that within the groups. A larger F-Score indicates a stronger confidence. The ANOVA R-sq is often referred to as the coefficient of determination and is a measure of the 'goodness of fit' of the regression model. If R-sq equals zero, then there is no linear relationship between the dependent and independent variables; if R-sq equals 1, the relationship is perfect and all values of the dependent and independent variables lie on a straight line.

The AUC values listed in the final column were obtained from a Receiver Operating Characteristic (ROC) curve for each peak. It is an evaluation of the discrimination quality of a peak. The area under the ROC curve (AUC), measures discrimination, which is the ability of the test to correctly classify two groups. In this instance the AUC is the score between the samples with the least IMAT concentration and the samples with the most IMAT concentration. Thus, the AUC measures the ability of a particular *m/z* to discriminate the two groups. The closer the area is to 0.5, the less useful the test is, and the closer it is to 1.0, the better the test is. This test was performed in the ClinProTools (Bruker) software.

MALDI IMS produces mass specific data of the intact protein species; however, the *m/z* alone is often not sufficient to positively identify the protein, as the biologically active protein may have undergone post-translational modifications. Robust protein identification is routinely achieved through protein separation/isolation, proteolytic digestion, sequencing of peptides by LC MS/MS, and matching the peptides to genome-based protein databases. The MALDI peaks confidently identified using these strategies are shown in Table 6. The molecular weight (MW) and corresponding protein identifications are listed along with the percent coverage, modifications, SwissProt Identification number, the number of peptides identified, peptide residues sequenced, and the protein trend as affected by the concentration of IMAT present.

Discussion

From the image data it can be determined that the IMAT is getting to the tumor, crossing the BTB, but there is substantially less IMAT penetrating into the normal, non-invaded, parts of the brain through the BBB. In previous studies it has been shown that the permeability of the BTB is greater than that of the BBB.[92, 93] BBB and BTB

Table 6: Protein Identifications for tumor implanted mouse brains treated with imatinib

	Protein Name	**% coverage of unprocessed precursor**	**Modifications (amino acid chain)**	**Swissprot Primary Accession Number**	**Number of Peptides**	**Peptide Residues covered**	**Trend**
4964	Thymosin beta-4	38	*(8-50)	P20065	1	27-45	up
6546	40S ribosomal protein S29	19	(2-56)	P62274	5	34-40, 49-56	up
7829	cAMP-dependent protein kinase inhibitor alpha	48	(2-76)	P63248	2	21-58	up
7890	Guanine nucleotide binding protein G(1)/G(S)/G(0) subunit gamma-13	13	*(2-67)	Q9JMF3	2	45-54	up
9202	Cytochrome c oxidase subunit 7A2	25	*(2-83)	P48771	2	34-56	up
9637	Cytochrome b-c1 complex subunit 8	54	(2-82)	Q9CQ69	3	11-25, 49-71, 74-82	up
9911	Acyl-CoA-binding protein	34	*(2-87)	P31786	5	34-53, 73-83	up
10255	ATP synthase subunit f	24	*(2-88)	P56135	2	17-39	down
10639	Protein S100-B	15	*(2-92)	P50114	2	7-21,	down
10952	Protein S100-A111 (Calgizzarin)	16	(2-98)	P50543	2	8-18, 51-57	up
11336	ATP synthase subunit g	36	*(2-103)	QPCPQ8	3	12-24, 36-54, 96-103	down
11516	cytochrome c, somatic	32	*(2-105)	P62897	5	29-39, 40-56, 93-100	down
11840	FK506-binding protein 1B	23	*(1-108)	Q9Z212	2	2-14, 59-72	down
12202	Snrpf protein	17	(1-112)	Q6NZQ3	2	92-99, 100-112	down
13896	Small nuclear ribonucleoprotein D3	13	*(2-126)	Q91VM2	3	55-64, 70-78	down
14052	Beta-synuclein	37	(1-133)	Q91ZZ3	5	33-84	down
14421	Bol A like protein 1	26	*(1-137)	Q9D8S9	3	22-37, 40-52, 77-85	down

***acetylated N-terminus (+42 Da)**

permeability measured by quantitative autoradiography (QAR) shows that the BTB has a K_i value of 12 while the K_i value of the BBB averages at 3. (The K_i value is the unidirectional transfer constant (µl/g/min) of a [^{14}C] labeled tracer.)[92] In another study brain metastasis uptake of ^{14}C-paclitaxel and ^{14}C-doxorubicin was generally greater than normal brain.[93] There is general agreement that most chemotherapy agents achieve only relatively low concentrations in the normal central nervous system, that the blood-brain barrier is variably disrupted in malignant brain tumors, and that the concentration of chemotherapy drugs in the brain adjacent to tumor is intermediate between concentrations achieved in brain tumors versus normal brain. Average drug concentrations in brain adjacent to tumor are lower than those within brain tumors[94] This difference in BTB and BBB permeability would explain why the IMAT signal is much stronger in the tumor region of the brain. This is also supported by a study that shows the IMAT can reach significant intratumoral concentrations in patients with glioblastoma multiforme and a disrupted BBB.[95]

The IMAT shows no signal in the control tissues, very high signal at 2h and then reaches its most intense at 6h. Following that at 12h and 24h the signal decreases. It has been shown that IMAT is rapidly absorbed after oral administration with peak plasma concentrations between 2h-6h having maximum plasma concentrations of 0.921 ± 0.095 μg/ml (mean ± S.D., n = 4).[96] Following that the terminal elimination half life was determined to be 13.5 ± 0.9 h.[96] IMAT is extensively distributed into tissues and highly protein bound, predominantly to albumin and α1-glycoprotein (AGP).[97] The image results correspond to the previous studies of IMAT absorption with highest signal intensities between 2h and 6h then drastically decreasing at 12h and 24h. In the chronic dosed tissues there is little signal in the 1d, 2d, and then increased signal in the 4d and 6d samples indicating there is an additive effect of the IMAT with chronic treatment. By continually taking a drug a steady-state of the drugs concentration can be reached and this is optimal for maximum efficiency of the treatment. It takes somewhere between 5 and 6 half-lives for a drug to reach steady state.[98] With the half-life of IMAT being around 12h it would be expected that by day 6 the IMAT presence in the brain has reached its steady state concentration.

Using the newly developed MALDI-MS/MS methods (Chapter II), the absolute concentration of the IMAT in the brain tissues was able to be calculated. When compared to the results obtained with the LC-MS/MS results there is an average percent difference of 40% with the MALDI results consistently higher in every instance. Part of the difference is most likely due to the fact that the recovery of the LC IMAT extraction was around 80%, so there is drug lost through the extraction process. There could have also been drug lost as a result of the IMAT sticking to the HPLC column during analysis. Another explanation could be that for the LC method, the entire tissue section analyzed is homogenized thereby averaging the entire tissue's drug concentration for the sample. For the MALDI, the spatial integrity is maintained, and the spots selected for analysis each receive their own IMAT concentration calculation and thus could represent areas of higher concentration locally than the average of the entire tissues concentration. Despite the higher concentrations calculated by the MALDI-IMS method, the trends of concentration from dosing group to group remains the same for both the MALDI and LC results.

Detection and identification of changes in the proteome of glioma as a result of targeted molecular therapies provides invaluable insights into the drug's activity. Typically, the proteins affected by IMAT administration are not extensively known. Many drug effects occur primarily when the blood level of the drug is either going up or down. When the drug reaches a steady state, these effects can be attenuated or completely absent. Therefore the most drastic changes will be seen in the samples with most varied levels of IMAT present as within the acutely dosed sample set.

A number of protein signals were found to have either increased or decreased signal intensities as a result of the IMAT presence. A group of these proteins are found to be involved in the mitochondrial electron transport chain (ETC). Cytochrome *c* oxidase subunit 7a2 (part of complex IV) and cytochrome b-c1 complex subunit 8 (part of complex III) were found to have an increase in intensity as the concentration of IMAT increased, while cytochrome *c* and ATP synthase subunits f and g (parts of complex V) had a decrease in intensity. Adaptive response to agents that challenge cellular homeostasis involves important changes in mitochondrial function. Given their crucial role in cell physiology, mitochondria are among the first responders to various stressors.[99]

The ETC or respiratory system occurs in the cristae of the mitochondria, where a series of membrane associated complexes, cytochromes and coenzymes, mediate biochemical reactions to produce ATP. These cytochromes and coenzymes remove electrons from the donor, NADH, and pass them to a terminal electron acceptor, O_2 via a series of redox reactions. The reactions create a proton gradient across the mitochondrial inner membrane, resulting in the transmembrane proton gradient used to make ATP via ATP synthase in oxidative phosphorylation.[100] The process of electron transport consists of four complexes. Complex I, which consists of NADH dehydrogenase (synonym: NADH-ubiquinone oxidoreductase), removes two electrons from NADH and transfers them to the carrier, ubiquinone. Simultaneously, Complex I moves four protons across the membrane to produce a proton gradient later used to generate ATP through oxidative phosphorylation. Complex II, which consists of succinate dehydrogenase, funnels electrons into the quinone group by removing electrons from succinate and transferring them via FAD to the quinone. Complex III (cytochrome *bc1* complex) removes two electrons from the quinone and transfers them to two molecules of cytochrome *c*, a water-soluble electron transporter located on the outer surface of the membrane. Simultaneously, Complex III moves two protons across the membrane, producing a proton gradient consisting of four total protons. When electron transfer is somehow hindered in Complexes I and III, there is a tendency for premature electron leakage to oxygen, resulting in the formation of superoxide. Complex IV, consists of cytochrome *c* oxidase. It is responsible for removing four electrons from the four molecules of cytochrome *c* and transferring them to O2, producing two molecules of water. Simultaneously, it also moves four protons across the membrane, producing a proton gradient. Finally, this proton gradient is utilized by the ATP synthase complex, also known as complex V to make ATP via oxidative phosphorylation.

The changed intensities of the proteins associated with the ETC can possibly be explained by evaluating the mechanisms of resistance to RTK inhibition such as antiapoptotic mechanisms. The mechanisms of resistance to RTK inhibition have not been fully elucidated, but is has been shown that tumor cells unresponsive to EGFR inhibitors are characterized by reduced induction of apoptosis. [101] Furthermore, while IMAT dramatically increases apoptosis in BCR-ABL–positive chronic myelogenous leukemia and in gastrointestinal stromal tumors, it does not induce apoptosis when administered to glioblastoma cells either in vitro or in vivo, even at high concentrations.[76, 102] Antiapoptotic mechanisms that render glioma cells resistant to cytotoxic agents (chemotherapy and radiotherapy) may also modulate their response to targeted therapies such as RTK inhibitors.[103]

A recent study into the chemoresistance of temozolamide (TMZ) showed that there were changes involving ETC. They explored changes in paired patient samples both before and after TMZ treatment. They found that complex II, III, and IV activities increased significantly ($p = 0.0005$) along with a significant decrease in complex I and V activity.[104] Considering that the cytochrome *c*/complex III molar ratio is the minimum needed for complex III activity[105, 106] an increase in complex III activity will likely decrease the pool of cytochrome *c* available for release from the mitochondrion to initiate apoptosis. This would explain why after the administration of IMAT there is an increase in the subunits associated with complexes III and IV of the ETC and a decrease in the cytochrome *c* and ATP synthase subunits (complex V) intensity in the tumor samples shown here. With this information, targeted experiments to elucidate the exact function of these proteins and how they could possibly be linked to treatment resistance and anti-apoptotic functions after administration of IMAT in gliomas can be investigated.

S100B is another protein that is affected by IMAT presence. There is a decrease in S100B protein intensity as the IMAT concentration increases in the tumor areas. S100B is a Ca^{2+}-binding protein of the EF-hand type that is abundantly expressed in astrocytes and has been implicated in the regulation of several intracellular activities, including proliferation and differentiation. S100B might contribute to reduce the differentiation potential of cells of the astrocytic lineage and participate in the astrocyte activation process in the case of brain insult and in invasive properties of glioma cells. Astrocytes represent the brain cell type with the highest expression of S100B. Levels of

S100B also increase in gliomas, raising the possibility that the protein might have a role in glioma pathophysiology.[107, 108] Studies have demonstrated that inhibition of S100B production in glial cells is correlated with at least three phenotypic changes: (a) a more flattened cellular morphology; (b) an alteration in cytoskeletal organization at the level of the microfilament network; and (c) a decrease in cellular growth rate.[109] Results obtained with two distinct antisense methods support the conclusion that S100B has important roles in regulation of glial cell morphology, cytoskeletal structure, and cell proliferation. Thus, a decrease in S100B intensity could indicate that IMAT mechanisms inhibit S100B and therefore create a decrease in the tumors cellular growth rate.

Another affect of increased IMAT concentration in the tumor tissue was a decrease in beta-synuclein intensities. β-synuclein is a synuclein protein found primarily in brain tissue and is seen mainly in presynaptic terminals. β-synuclein is predominantly expressed in the neocortex, hippocampus, striatum, thalamus, and cerebellum.[110] The γ-synuclein protein has been found to be abnormally expressed in a high percentage of tumor tissues of cancer types, including liver, gastric, lung, prostate, cervical *etc*.[111] and α-synuclein has been implemented in a number of neurodegenerative disorders.[112] Synucleins have also been found to be expressed highly in glial tumors[113] and although their exact function is not yet known they are known to be involved in cellular functions including synaptic plasticity, neurofilament organization, control of dopamine homeostasis and vesicular transport.[114]

Many other identified proteins were also affected by the IMAT concentrations although not all of the functions in glioma tissues have been completely elucidated. Small nuclear ribonucleoprotein D3 intensities are decreased at high concentrations of

IMAT in tissue. Small nuclear ribonucleoprotein particles have been shown to have an integral role in pre-mRNA splicing.[115] Global aberrant alternative pre-mRNA splicing has been indicated as an epigenetic phenomenon in cancer and specifically independent. *In silico* genome-wide assessments have identified genes expressing particular splice isoforms more frequently in glioma than in normal brain.[116] BolA like protein 1 has a decreasing intensity at high concentrations of IMAT. The BolA-like proteins seem to be involved in cell proliferation or cell-cycle regulation, but the molecular function is still unknown.[117] Acyl CoA binding protein shows an increase in intensity and is known to bind medium- and long-chain acyl-CoA esters with very high affinity and may function as an intracellular carrier of acyl-CoA esters. *In vitro* and *in vivo* experiments suggest that it is involved in multiple cellular tasks including modulation of fatty acid biosynthesis, enzyme regulation, regulation of the intracellular acyl-CoA pool size, donation of acyl-CoA esters for β-oxidation, vesicular trafficking, complex lipid synthesis and gene regulation.[118]

In summary, the MALDI MS data obtained in this study were able to provide 43 molecular features associated with IMAT concentration in the brain tumors. Correlating IMAT distribution to proteome response in the brain MALDI MS analyses provided a means to directly correlate drug distribution with pharmacological response and provided insight into the concentration-effect relationship. Further work needs to be performed to determine the identity of all the molecular features altered in order to rationalize the biological significance of these proteins. Evaluating some of the proteins already identified, many molecular processes including ETC, proliferation, cell cycle regulation and pre-mRNA splicing have been found to be affected by the administration of IMAT.

Additional experiments can delve further into these functions and provide more information on the efficacy of IMAT, reveal additional drug targets, and help elucidate the mechanisms of the drug action on the brain tumors. Additionally, the MALDI-IMS techniques provide a rapid, reproducible method to find the IMAT drug concentrations in tissue while maintaining spatial integrity.

Materials and Methods

Materials

The MALDI matrices, sinapinic acid and 2,5-dihydroxybenzoic acid, tissue staining chemicals cresyl violet acetate, hemotoxylin and eosin, and ammonium acetate were purchased from Sigma Chemical Co. (St. Louis, MO). Acetic acid, HPLC grade acetonitrile, ethanol, methyl-tert-butyl ether (MTBE) and MeOH were purchased from Fisher Scientific (Suwanee, GA). Trifluoroacetic acid (TFA) and hydrochloric acid (HCl) was purchased from Burdick and Jackson (Muskegon, MI). Dulbecco's Phosphate-Buffered Saline (D-PBS), Dulbecco's modified eagle medium (DMEM), fetal calf serum, penicillin-streptoycin, Tissue Protein Extraction reagent (TPER), phosphate buffer solution (PBS), tricine gels, reducing agent, See Blue, Novex Tricine SDS Running Buffer, trypsin, 0.05% with EDTA and Colloidal Blue Staining kit were purchased from Invitrogen (Carlsbad, CA). Trypsin gold was purchased from Promega (Madison, WI). Imatinib was acquired from the Vanderbilt Research Pharmacy in 100 mg tablets (Nashville, TN). Imatinib and d8-imatinib were provided as their mesylate salts by Dr. Jeremy Norris (Protein Discovery, Knoxville, TN). GL26 murine glioma cells were acquired from Vanderbilt University (Dr. Moneeb Etesham's laboratory, Nashville, TN). C57BL/6NCr female mice were purchased from Charles River Laboratories (Wilmington, MA). Animal sedatives xylazine, ketamine, and buprenorphine were purchased from Lloyd laboratories (Shenandoah, Iowa).

Cell Culturing

Cryogenically frozen GL26 murine glioma cells were obtained from the Neurology Department Brain Tumor Bank at Vanderbilt University. The cells were thawed and then placed in DMEM containing 10% fetal calf serum, and 1% penicillin-streptomycin. Aseptic cell culturing technique as described[119] was employed to continue the cell line growth and cells were maintained in humidified incubators gassed with 5% carbon dioxide. Prior to injection, GL26 cells were harvested, washed twice in PBS, counted, and adjusted to 100,000 cells per µl of DPBS in an eppendorf tube.

Tumor Implantation

From their time of arrival at the animal facility, each animal was housed undisturbed to acclimate to the new environment for a period ranging from 1-3 days. Food, Purina 5001 rodent diet, and water were provided *ad libitum* to animals upon arrival and throughout the study. After the acclimation period, animals were taken to the procedure room for survival surgery to implant the GL26 murine tumor cells intracranially. The survival surgery involved the establishment of intracerebral brain tumors in the mice. To achieve this, animals were first anesthetized. For administration of the anesthesia the animals were held by hand while the brief injection was made directly above the hind limb on the underbelly of the animal (intraperitoneal injection) of 200 µl (0.019 ml/g of weight) of a mixture of xylazine (2.2%) and ketamine (6.5%). After administration the animals were immobilized in a stereotactic frame, and received an intracranial injection (2 µl, approximately 200,000 cells) of the GL26 brain tumor cells (resuspended in DPBS) into the brain. This necessitated the placement of a midline incision in the scalp followed by creation of a burr hole (using a high-speed dental drill) in the skull at the site 2.5 mm lateral to bregma where the tumor injection was to take place. Tumor cells were injected at a depth of approximately 2.5 mm below the surface of the skull. The injection was done very slowly (1 µl/min), and then the needle was left in place for 2 min before removal to avoid liquid reflux. The syringe was removed and the scalp incision was closed with wound clips. All techniques were performed using sterilized instruments and the wound was created and closed using aseptic procedure. In the postoperative period it was expected that these techniques impart pain on the animal. To address this, animals received a subcutaneous injection of buprenorphine (0.05 - 1.0 mg/kg) prior to the animal waking up from anesthesia. They then received an additional injection of buprenorphine 8-12 hours after the first injection due to the possibility of further postoperative pain. Animals were placed on a thermal blanket during surgery to ensure maintenance of body temperature and were kept under a physiological heat lamp after surgery while they were recovering from anesthesia. Following recovery, animals were placed back in their cages, returned to the vivarium, and monitored daily for signs of infection or distress. After ten days, once the scalp incision had healed, the wound clips were removed.

Animals were monitored daily for a period ranging from 15-20 days to allow for tumor growth to occur. After this period select animals that had been designated for drug dosing were handled and received a non-toxic and physiologically relevant dose of drug as determined by the experiment being performed.

Operative mortality will likely occur within 48-72 hours of surgery; these animals will be removed from the analysis. As a 10-12.5% mortality has been reported using this procedure, one additional animal per treatment group per experimental replicate was implanted.

Drug Dosing

Imatinib was obtained from the Vanderbilt Research Pharmacy in the form of a 100 mg tablet. These are the same tablets that patients would receive if prescribed IMAT. Tablets were dissolved in water at a pH=4 (water made acidic with the addition of HCl) resulting in a 10 mg/ml drug solution. IMAT is readily soluble at acidic pH values (≤ 5). The solution was vortexed for five minutes to ensure that the entire quantity of IMAT was dissolved. The IMAT solution was stored at -4 °C for no longer than 48 hours before fresh solution was made. The drug placebo administered was water at pH=4 (made acidic with the addition of HCl).

For oral gavage the animal was held by hand while tipping the head up to allow the insertion of the oral gavage blunt tipped needle into the mouth and down toward the stomach. Once the needle was in place approximately 300 µl of the drug solution (resulting in a 100 mg/kg dose) were administered to the animal. After administration the needle was slowly removed from the mouth and the animal was immediately released.

Tissue Preparation and MALDI Imaging

After all dosing had been completed the animals were taken to be sacrificed. Each animal was put under anesthesia, (110 mg/kg Ketamine and 10 mg/kg Xylazine) through intraperitoneal injection as a single dose followed by spine dislocation and immediate decapitation. Brain tissues were excised from the C57/BL/6 mice using sterile dissection techniques and immediately flash frozen in liquid nitrogen. All tissues were kept at -80 °C until further use.

Frozen brain tissues were mounted onto a cryostat chuck with OTC. Tissue was trimmed until an even sagittal section was acquired at Interaural 10.6 mm, Bregma 1.6 mm, where the corpus callosum has started to join at the mid-line of the brain. From this position tissue sections (12 µm) were collected, one for protein analysis, a serial section for IMAT analysis and a serial section for H&E staining. Sections for protein and IMAT analysis were mounted onto gold-coated MALDI targets while the sections for staining were thaw mounted onto charged glass microscope slides.

For cresyl violet staining, 0.5% cresyl violet was made by adding 2.5 g of cresyl violet acetate to 250 ml of distilled water and 1.5 ml of acetic acid. The solution was stirred for 20 minutes and then filtered. After sections had been mounted onto the charged glass slides, they were dipped briefly, approximately 5 seconds, into water. The slides were then dipped into the 0.5% cresyl violet for 45 seconds, rinsed briefly with water and rinsed with 100% ethanol for 20 seconds. Slides were then placed into Xylene for 5 minutes followed by cover-slipping with cytoseal.

For H&E staining, slides were dipped in a series of solutions to re-hydrate, dehydrate and stain the tissue sections. 30 seconds in 95% ethanol. 30 seconds in 70%

ethanol. 30 seconds in Milli-Q water. 2 minutes in hematoxylin solution (deep purple; stains nuclear contents). 20 seconds in Milli-Q water. 30 seconds in 70% ethanol. 30 seconds in 95% ethanol. 1 minute in eosin solution (pink; stains cytoplasm). 30 seconds in 95% ethanol. 30 seconds in 100% ethanol. 2-2.5 minutes in Xylene. To cover-slip, dry the back of the microscope slide and around the tissue section with a Kimwipe to get rid of excess xylene. Put 1-3 drops of cytoseal on the tissue section and then place a coverslip over area. Make sure to get rid of air bubbles and let the cytoseal dry until hardened.

MALDI targets were placed into a desiccator for at least an hour to dry. To prepare sections for imatinib imaging a matrix solution of DHB (40 mg/ml, 50% MeOH) was prepared with 2 µM d8-imatinib as the internal standard. Sections were spotted on the Portrait (Flyby 1 drop 40 repeats) at 300 µm x 300 µm spatial resolution. All IMAT images were acquired on a MALDI-LTQ XL. The MALDI target with sections designated for protein analysis was reagent washed (70% reagent alcohol for 30 seconds, 70% reagent alcohol for 30 seconds, 100% reagent alcohol for 15 seconds, air dried). The surface of the sections were then seeded with finely ground SA. Fresh SA matrix solution was made in 60% acetonitrile 40% water 0.02% TFA. The sections were spotted using the Portrait (Flyby 1 drop 30 repeats) in a 300 µm x 300 µm array. The MALDI target was scanned and sections were imaged on an Autoflex (Bruker Daltoniks).

Data Pre-Processing

Data analysis generally lies in two categories; pre-processing and statistical analysis. It is important to assess reproducibility of the mass spectra so that variations in peak intensities can be correlated to biological endpoints. The pre-processing step reduces the experimental variance between spectra through the removal of background, normalization of the peak intensity to the total ion current, and peak alignment algorithms. Normalization of the spectra minimizes variation arising from day to day instrument fluctuations, differences in matrix crystallization across tissue sections, and changes in sample preparation and chemical properties of the underlying tissue [120]. Various algorithms are employed for all of the spectra processing steps; baseline subtraction, smoothing, peak alignment, normalization and peak picking. Ion images are generated directly from these processed data sets.

For each image acquired, the corresponding stained serial section was co-registered and with the assistance of a neuro-oncologist the spectra from the tumor bearing regions were exported. Spectra from each section were kept together in separate folders. These folders were then input into ClinPro Tools where the imported spectra were processed with the following parameters; 1200 Resolution, data reduction factor of 5, Top Hat baselining with 10% Minimal Baseline Width, Savitsky Golay Smoothing enabled at 2 width 10 cycles, recalibration 2000 ppm max peak shift with 20% match to calibrate peaks excluded not recalibratable spectra, from m/z range 4000-20,000, and null spectra exclusion. Once spectra were imported into ClinPro Tools and processed, peak selection was performed (peak picking on total avg spectrum, SN=2, 0% relative threshold to the base peak) and peak list feature tables were output.

Protein Identification

Tissues were homogenized in TPER supplemented with protease inhibitors. For each extract, a Vydac C8 polymeric reversed-phase column (3.2 x 150mm) fractionated 300 g of protein solution (96 min linear gradient from 2-90 plate). During separation, a liquid handling robot moves the transfer capillary sequentially into each of the 96 wells at 1 min intervals. To identify wells containing proteins of interest in an automated process, 0.2 L was removed from each well, mixed with SA matrix, and analyzed by MALDI-MS (Bruker Autoflex). Fractions containing *m/z* values of interest were run on a gel (10-20tricine) and bands of interest were excised and digested with trypsin gold (Promega; Madison, WI). In solution trypsin digest was also performed on fractions which contained m/z values of interest. A non-linear quadrupole high capacity trap (Bruker HCT Plus) was used to analyze digested proteins. The peptides were separated on a packed capillary column, with C18 resin (Monitor C18, 5 m; Column Engineering, Ontario, CA), using a linear gradient (5MS/MS spectra were initially analyzed by searching the mouse International Protein Index database using Sequest software). Protein IDPicker software (David Tabb and Bing Zhang laboratories in the Vanderbilt University Medical Center department of Biomedical Informatics) was then used to determine the probability that a protein had been correctly identified, based on the available peptide sequence evidence.

Drug Quantitation Using LC-MS/MS

Standards of IMAT and d8-IMAT were prepared as stock solutions in methanol. Calibration standards were made by adding the stock solutions to control brain tissue homogenate to yield final concentrations of 3000, 1000, 500, 100, 25, 10, 1 ng/ml.

Tissue specimens were homogenized with PBS in a ratio of 1:4 (mg/µl) using a glass homogenizer until uniform by visual inspection. A minimum of 30 mg of tissue was used to prepare the homogenate, which was then transferred to eppendorf tubes before being centrifuged at 3000 g for ten minutes. Fifty microliters of the supernatant was combined with 25 µl of internal standard (d8-imatinib, 1000 ng/ml) and then the protein was precipitated by adding 250 µl of acetonitrile/ethanol/acetic acid (90/10/0.1) with mixing by inversion for 20 minutes. Samples were then centrifuged at 4000 g for ten minutes to remove the precipitant. After centrifugation, the supernatant was transferred to glass autosampler tubes and dried in a vacuum centrifuge for two hours at 40 °C and then reconstituted in 75 µl of 50% methanol containing 0.05% ammonium acetate.

Chromatographic separation was performed using a Waters XTerra RP® C18 reverse phase column (2.1 x 100 mm, 5 µm particle) with a column heater (50 °C) and autosampler (4 °C) on an HPLC system. The system was held at 90% MeOH for two minutes then a linear gradient of MeOH and water, both with 0.5% ammonium acetate was increased from 20% to 90% MeOH over two minutes and held at 90% MeOH for two minutes before the column was then washed with a solution containing 70% acetonitrile, 20% MTBE and 10% water of the course of five minutes, going from 0 to 100% over two minutes and maintaining at 100% for three minutes. The system was then returned to initial conditions over two minutes and equilibrated for two minutes before beginning the next run. The total run time was 14 minutes per sample at a flow rate of 0.5 ml/min. Ten microliters of sample were injected using a 10 µl PEEK loop and subsequently analyzed on an ESI TSQ Quantum triple-quadrupole system (Thermo Scientific, Waltham, MA).

Acknowledgements

Dr. Michael Edgeworth assisted with the GL26 mouse implantation and dosing along with the pathological determination of tumors in the stained images. Dr. Moneeb Ehtesham provided the use of the animal surgical room. Larry Pierce provided the cryo-frozen GL26 cells. Deming Mi assisted with the statistical analysis.

CHAPTER IV

ANALYSIS OF CYCLOPAMINE TREATED DIRECT HUMAN GLIOMA CELL IMPLANTED MOUSE XENOGRAFTS

Overview

Despite recent advances in therapeutic techniques, the prognosis for patients with malignant brain tumors remains grim. The lethality of this disease process stems in part from the highly invasive nature of these tumors. Microscopic nests of tumor cells intersperse themselves with normal brain tissue, often at significant distance from the main tumor mass. Due to their large number and varied location, current treatment strategies are unable to specifically eliminate these tumor reservoirs in their entirety, leading to eventual tumor recurrence.

One possible means of targeting disseminated tumor within the brain is the use of targeted molecular therapies. It has previously been demonstrated that targeted molecular therapies are capable of directly or indirectly inducing tumor-cell death in various cancer models. The previous chapter investigated one of these therapies (IMAT). These findings point to the potential that MALDI IMS technologies are useful in evaluating treatment of malignant brain tumors.

Little is currently understood regarding the biological pathways and mechanisms that govern the effects of these molecular compounds on tumor cells. The elucidation of these pathways will be critical in order to better understand and optimize this highly promising therapeutic strategy for brain cancer. *In this project, we now seek to detect the quantitative distribution of the targeted molecular therapy cyclopamine and to define the biological mechanisms that govern the ability of molecular targeted therapies to induce death of tumor cells in the brain.*

Introduction

Sonic Hedgehog Pathway in Gliomas

Sonic Hedgehog (Shh) is a member of the Hedgehog (Hh) family of secreted glycoproteins, which affect the development of many organs and cell groups. In mammals, there are three known Hh family members; Sonic, Desert and Indian Hh. They are involved in the development of many tissues and organs, including skin, lung, brain, bone and blood. Shh is the most widely expressed.[121, 122] In the central nervous system, Hh signaling is critical for early ventral patterning of the neural tube along the entire neuroaxis and later on for the development of the dorsal brain, including that of the cerebellum and neocortex.[123, 124] Hh acts by inhibiting a 12-pass transmembrane protein called Patched1 (Ptc1) which normally inhibits a 7-pass transmembrane protein called Smoothened (Smo). Activating Smo sends a signal intracellularly through intricate mechanisms by a complex of proteins, to ultimately lead to the action of the zinc finger Gli transcription factors.[125] When this pathway is activated or maintained inappropriately, various tumors can develop, including those in skin, muscle and brain. Numerous studies have now shown that Shh signaling is essential for glioma cancer stem cell self-renewal and cancer stem cell-initiated brain tumor growth.[121, 125-127] Inhibition of the hedgehog pathway however, kills these cancer stem cells and can prevent cancer from growing and developing which could lead to a very effective stem cell targeted therapy for gliomas.

Cyclopamine

Cyclopamine (CYC) is a teratogen that has been isolated from the lily Veratrum californicum. It is a member of the steroidal jerveratrum alkaloids. CYC was originally given its name due to the birth defects it caused in sheep giving them one eye. Much interest in CYC has developed, owing to its ability to inhibit the Shh pathway resulting in the inhibition of tumor growth and tumor progression.[128-131] CYC acts by targeting Smo, which inhibits its activity in the absence of Ptc1, thereby turning off the Hh pathway and stopping the malignancy growth source.

Direct Human Cell Xenograft Animal Models

Typically animal models used in the investigation of cancer involve the transplantation of mouse or rat tumor cells into a host of the same species and strain.[132, 133] Growth of human (xenogeneic) tumor cells can be achieved using immunodeficient (nude or SCID) mice to prevent rejection.[134, 135] Most transplantable tumors are established subcutaneously but more complex models may involve orthotopic transplantation at appropriate primary sites.[136] There is an increasing trend to establish xenograft tumors directly from human cancer stem cells, to avoid artificial selection of cells in tissue culture and changes in gene expression and phenotype, which this may induce.[137-139] These transplants may better model the principal cancer under investigation, by more accurately representing the tumor architecture, heterogeneity, expression of certain targets and response to therapy.[140] Glioma cells are known to undergo phenotypic and genotypic transformation in culture, however tumor stem cells derived directly from primary glioblastomas have extensive similarities to normal neural stem cells and recapitulate the genotype, gene expression patterns, and in vivo biology of human glioblastomas.[141]

Results

Animal Implantation and Drug Dosing

To begin the study, a series of mouse implantations with human tumor cells and sub sequential drug dosing was performed. Nod-scid immunodeficient mice were used and orthotopically implanted with glioma tumor stem cells derived directly from human biopsy tissue. The cells were never subjected to culture and were obtained by homogenizing the tumor samples directly, dissociating with papain, and passing the homogenate through a 40 μm filter. Cells were labeled with a CD133/1 antibody cross-linked to magnetic nanoparticles and subjected to immunomagnetic cell separation using the EasySep Magnetic Selection Kit.[130] Three primary tumor specimens were used to result in the following xenografts, an anaplastic ganglioglioma (X-302-AG), a high-grade astrocytoma (X-312-HGA) and a primary glioblastoma multiforme (X-406-GBM). Recapitulation of malignant glioma pathological features was observed and included infiltrative growth, invasion of the corpus callosum to the contralateral hemisphere and pleomorphic nuclei with mitotic figures.[130] When compared to the GL26 murine cell implantation, which shows a very large mass with a clearly defined brain tumor barrier (Figure 24A), the primary tumor xenografts show a much more infiltrative and disperse growth of the tumor cells throughout the entire brain. The human transplanted cells were visualized by anti-human nuclear immunohistochemistry (Figure 24B).

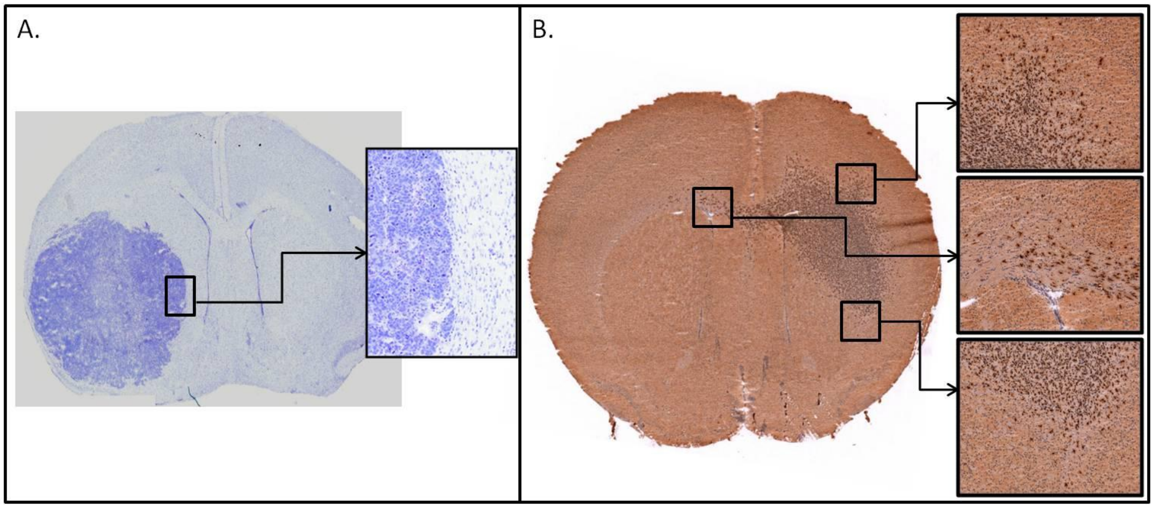

Figure 24: Visualization of tumor cell growth in mouse brain sections. A) A C57BL/6NCr mouse brain section implanted with GL26 tumor cells stained with cresyl violet. There is a very large bulk tumor mass with a very definitive brain tumor barrier which can be seen clearly in the inset frame. B) A NOD/SCID mouse brain section implanted with primary tumor AG-02 cells stained with anti-human nuclear immunohistochemistry. The tumor cells show a very infiltrative and disperse growth pattern throughout the brain. The inset frames show magnified sections of the brain where the invading tumor cells are visualized as the darker stained cells against the surrounding areas of the normal brain tissue.

For each of the xenograft lines three mice were injected with CYC every 12 hours at a dose of 50 mg/kg totaling 100 mg/kg each day. This was done for five days. Three additional mice from each line were dosed in the same manner using vehicle (Veh) only to serve as the control. For the X-302-AG xenograft model additional mice were dosed. Mice were dosed to result in some that were dosed 50 mg/kg/day (CYC 50), 100mg/kg/day (CYC 100) or 150 mg/kg/day (CYC 150). All mice were sacrificed five hours after their final dose of CYC and the brains were excised, flash frozen in liquid nitrogen and stored at -80°C until further use.

Drug Detection and Quantitation

In order to visualize the distribution and quantitate CYC in the brain tissue, MALDI IMS was performed on 12 µm thick brain sections spotted with CHCA (20 mg/ml, 50% acetonitrile). Prior to the quantitation and imaging experiments an initial analysis of CYC standard (*m/z* 412) on the MALDI LTQ XL revealed that there was an extensive fragment profile with daughter ions at m/z 394, 377, 335, 321 and 213 (Figure 25). Various matrix/solvent combinations were tried and they all revealed interfering peaks with the parent *m/z* and also with the major fragment peak of the CYC at *m/z* 394. Due to this matrix interference, the other fragment peaks were used to monitor the drug distribution in the tissue.

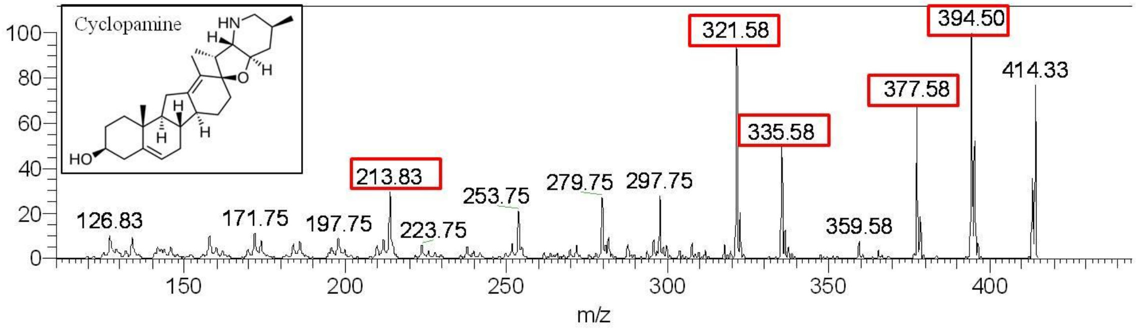

Figure 25: MALDI MS/MS spectra of cyclopamine taken on a MALDI LTQ XL showing major fragment peaks at *m/z* 394, 377, 335, 321 and 213. These peaks can be selected to monitor the spatial location of the compound in tissue sections. The inset box shows the structure of the parent compound with a molecular weight of 411.

Using the MALDI small molecule quantitation protocol developed in Chapter II, the tissue sections from X-302-AG mouse brains were analyzed. First, 12 µm sections were collected from each brain and weighed on a microbalance immediately following sectioning. A 12 µm Nod/Scid mouse brain section had approximately the same weight as a C57Bl/6NCrl mouse brain section (Chapter III) weighing 0.68 mg with a RSD of 4%. Brian sections were then stained and scanned using a flatbed scanner at 3200 dpi to provide images for the tissue area calculation. The images were imported into Adobe Photoshop and the area of the section was determined to be 62.44 mm^2 with a RSD of 0.2% which was approximately the same area as the C57Bl/6NCrl mouse brain sections. In Chapter II the area of the laser spot was found to be 0.0035 mm^2, so the amount of tissue sampled within one laser position was calculated from the equation: 62.44 mm^2/0.68 mg = 0.0035 mm^2/X mg. The amount of tissue sampled was 3.81 x 10^{-5} mg.

A calibration curve for CYC was constructed by spiking CHCA (20 mg/ml 50% acetonitrile) with CYC standard to yield final concentrations of 6800, 680, 68, 6.8 and 0.68 fg along with a blank matrix control. All solutions were spiked with 2 µM of jervine (JERV), which served as the internal standard for the experiments. Spectra were acquired from each of the spots, using 600 laser shots per position and 14 positions per matrix spot. This totaled 140 different laser positions for each standard due to the fact that 10 matrix spots per calibration standard were analyzed. For each spot the total signal intensity was summed for both the CYC and JERV using in-house software and the ratio of CYC/JERV was calculated. The ratios for each calibration standard were plotted and a linear fit was calculated. Each point on the curve had a RSD no higher than 27% and the curve had excellent linearity with an R^2 value of 0.9999 (Figure 26).

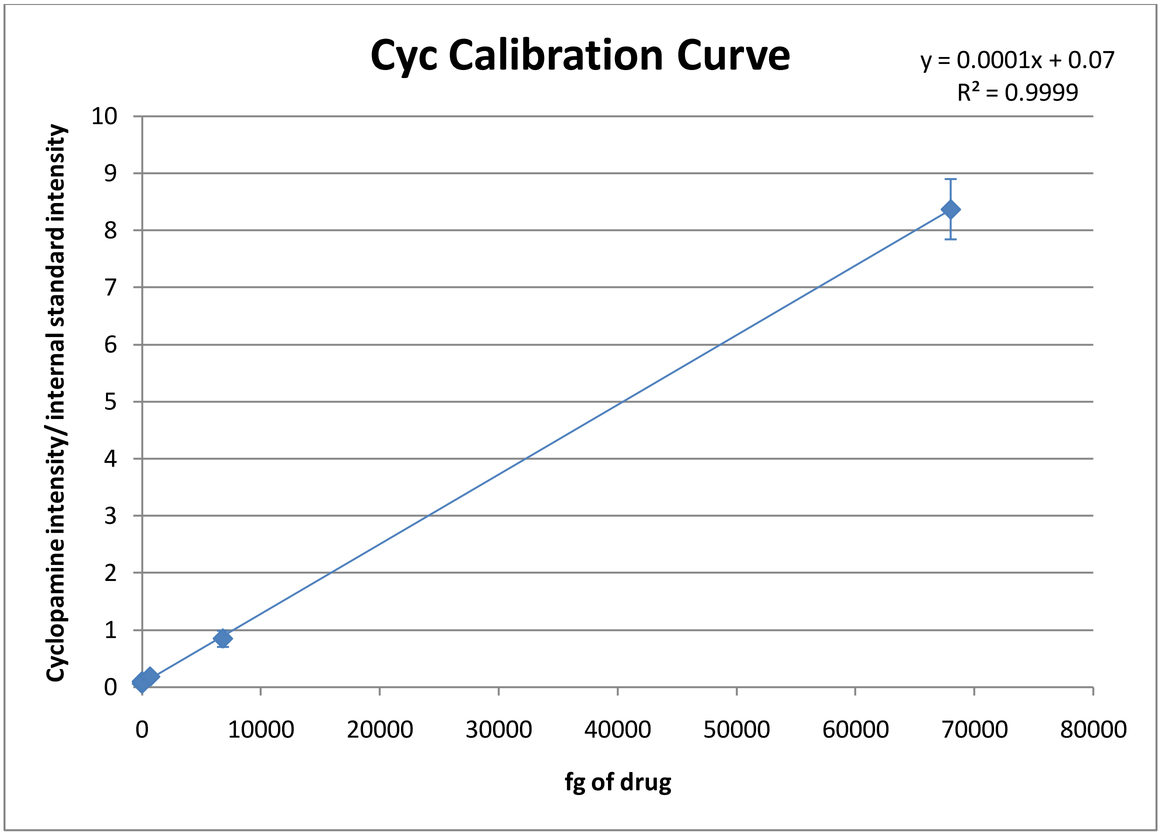

Figure 26: Cyclopamine Calibration Curve constructed using MALDI IMS methods

From this curve the LOD of cyclopamine with this acquisition method by MALDI was determined to be approximately 1650 ng/g of tissue.

Tissue sections for the Veh, CYC 50, CYC 100 and CYC 150 X-302-AG mice were cut at 12 µM. The sections were spotted with CHCA in 50% Acetonitrile spiked with 2 µM JERV internal standard. Due to the infiltrative nature of the tumor cells within the brain, matrix spots were analyzed from various regions in the brain to get a representation of the amount of drug present in the tissue. A total of ten matrix spots were analyzed for each tissue with 14 positions per spot totaling 140 positions for each brain. The ratio of total CYC signal intensity over total JERV signal intensity was calculated and plugged into the calibration curve equation to calculate the amount of CYC present in fg. The amount of CYC was divided by the amount of tissue sampled to provide the CYC concentration for each tissue analyzed in ng of CYC within 1 mg of tissue. The Veh and CYC 50 tissue samples were below the limits of detection and therefore the concentration of CYC were unable to be calculated by the MALDI method. However, the CYC 100 tissues had a concentration of 2937 ng/g with a RSD of 26.7% and the CYC 150 tissues had a concentration of 12333 ng/g with a RSD of 15.1% (Table 7).

Table 7: Comparison of cyclopamine concentrations calculated by both LC-MS/MS and MALDI-IMS methods.

CYC ng/g	**CYC 50**	**CYC 100**	**CYC 150**
LC	688	2998	8051
LC RSD	3.2	6.2	3.7
MALDI	below LOD	2937	12333
MALDI RSD		26.7	15.1
% difference		2	35

For comparison, traditional drug quantitation techniques involving homogenization and drug extraction followed by analysis on a LC-triple quadrapole system were performed. The calibration curve for this experiment was constructed using a CYC concentration range from 0.1 -1000 ng/ml and the response curve was generated. A representative calibration equation, $y = 0.025x + 0.006$ ($R^2 = 0.9917$) was calculated using a weighted ($1/x^2$) least squares linear regression model. Samples of brain tissue from the Veh, CYC 50, CYC 100 and CYC 150 X-302-AG mice were analyzed and using the response curve, average CYC concentrations (ng of CYC per g of tissue) were calculated for each dosing group (Table 7). The Veh tissue contained no CYC, the CYC 50 tissue had a concentration of 688 ng/g, the CYC 100 tissue had a concentration of 2998 ng/g, and the CYC 150 tissue had a concentration of 8051 ng/g of cyclopamine as calculated by the LC-MS/MS methods. All concentration calculations had an RSD less than 6.5%. Comparing the quantitation results from both the MALDI and the LC-MS/MS methods reveals a close similarity for the CYC 100 and CYC 150 samples with percent differences of 2% and 35% respectively.

To obtain images of the CYC distribution in the X-302-AG brains, 12 µm sections were cut and spotted with CHCA (20 mg/.ml, 50% acetonitrile) spiked with 2 µM JERV as an internal standard. All images were acquired on the MALDI LTQ XL and visualized using ImageQuest software (Thermo Scientific Inc.). Three transitions were monitored to evaluate CYC resulting in images for *m/z* 377, 335 and 321. As can be seen in Figure 27, there is some background signal in the Veh mice and the signal in the CYC 50 samples is below the LOD. However, in the CYC 100 samples some signal starts to become visible above the background and in the CYC 150 samples there is clearly CYC signal as represented at all three *m/z* values monitored. This is consistent with the quantitation results. The bottom row in the figure show a representative H&E stained brain section for each dosing group.

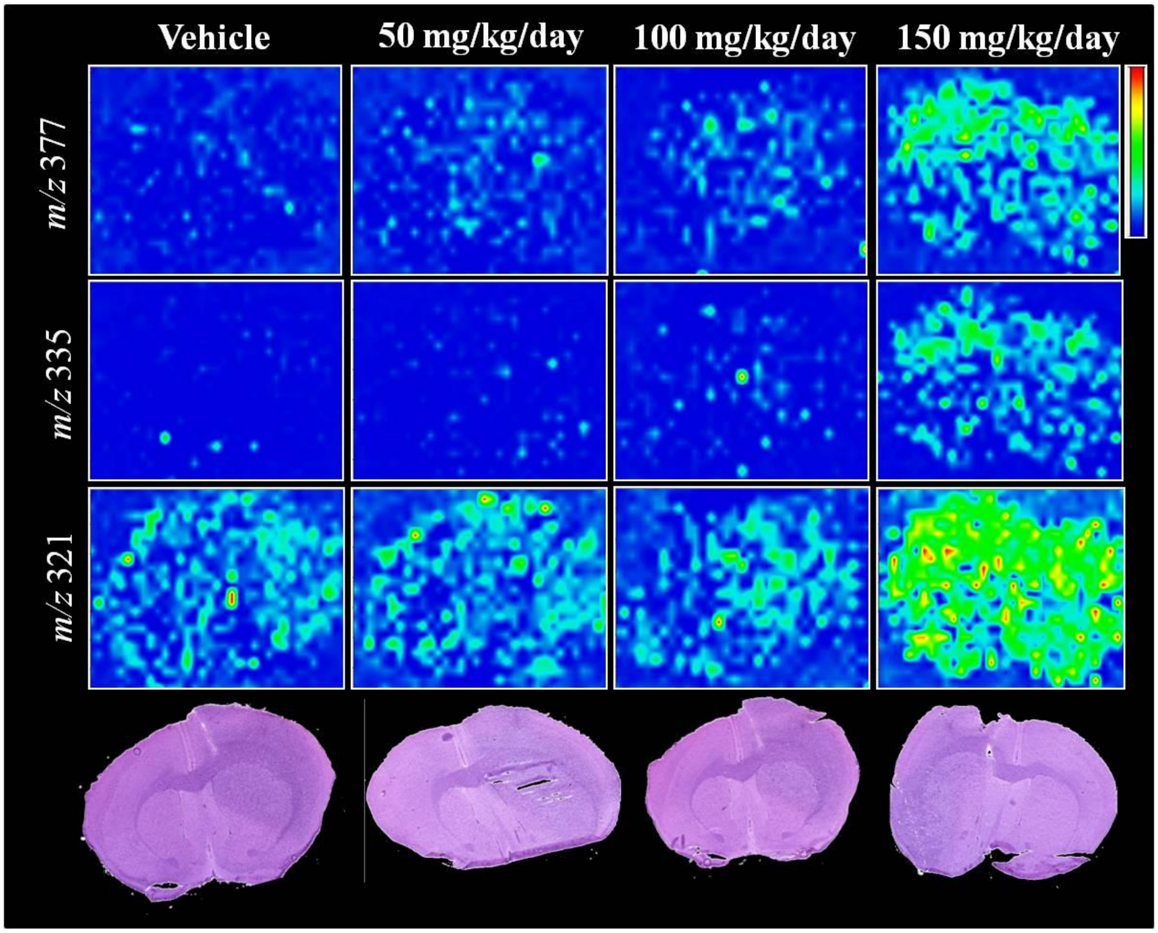

Figure 27: Images of cyclopamine distribution in the dosed X-302-AG brain sections at each dosing level. *m/z* values 377, 335 and 321 were monitored. Background signal can be seen in the Veh brains and the signal in the 50mg/kg/day dosed brains is below the LOD. Some signal is visible above the LOD in the 100 mg/kg/day brains and there is distinct CYC signal in the 150 mg/kg/day samples. The bottom row shows a representative H&E stained brain section for each dosing group.

Responder versus Non-Responder Proteome Study

In a study parallel to this one, the operational status of the Hh pathway in the malignant glioma specimens used for the xenografts was determined. Gliomaspheres (GS) were generated for two of the three specimens (GS-312-HGA and GS-406-GBM) under culture conditions required for eliciting a Hh pathway response in glioma primary cell cultures.[130] It was found that an operational Hh pathway was present in the 312-

HGA primary tumors but that the 406-GBM tumor lacks an operational Hh pathway. In order to determine the effect of in vivo Hh pathway inhibition by cyclopamine X-312-HGA and X-406-GBM mice were treated and assayed for survival. It was found that continuous treatment with CYC (50mg/kg twice daily) showed a median survival difference of 11.5 days (P=0.0062, Logrank test) in X-312-HGA mice but no difference in survival was measured in the X-406-GBM mice receiving the same CYC treatment (Figure 28).[130]

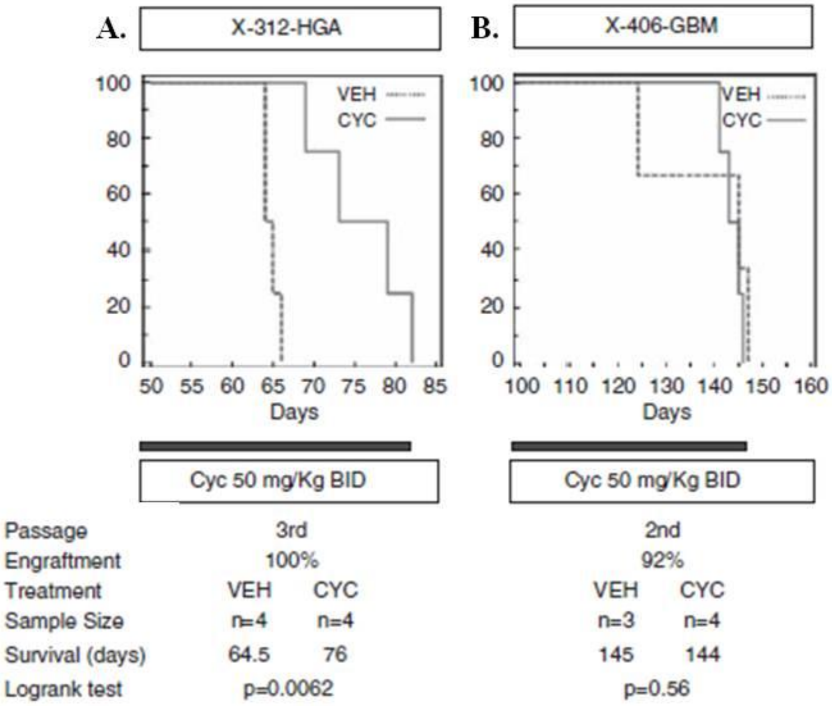

	A. X-312-HGA		B. X-406-GBM	
Passage	3rd		2nd	
Engraftment	100%		92%	
Treatment	VEH	CYC	VEH	CYC
Sample Size	n=4	n=4	n=3	n=4
Survival (days)	64.5	76	145	144
Logrank test	p=0.0062		p=0.56	

Figure 28: Hedgehog pathway inhibition confers a survival advantage. A) Treatment was initiated in X-312-HGA mice 50 days after xenotransplantation and continued for the duration of the survival study. Cyclopamine-treated mice (50 mg/kg twice daily) had a median survival of 11.5 days longer than vehicle-treated mice (*P* =0.0062, Logrank test). B) Continuous cyclopamine treatment of X-406-GBM mice (50 mg/kg twice daily starting 100 days after xenotransplantation) did not enhance survival (*P* =0.56, Logrank test). Solid grey bars indicate duration of treatment. (Figure adapted from A. Sarangi *et.al*)[130]

To further investigate the differences between the CYC responder (X-312-HGA) and non-responder (X-406-GBM) xenografts, protein images were taken from the brains using MALDI TOF IMS. Standard MALDI imaging preparation techniques were employed to get the samples ready for analysis. The CYC treated and control brains were cut on a cryostat and sections were thaw mounted onto target slides, dried and then matrix was applied using a Portrait™ 630 spotter before imaging on a Bruker Autoflex TOF MS. Three sections were analyzed for each brain and sample acquisition was randomized to eliminate bias. Serial sections were cut for each brain and stained with anti-human nuclear immunohistochemistry. The stained sections were scanned on a Mirax Scanner (Carl Zeiss MicroImaging) and the images were saved. All sections were evaluated by a trained neuropathologist to mark areas of tumor invaded and non-invaded regions. Eight regions were marked using the Mirax software; striatum, invaded striatum, lateral ventricle (LV), invaded lateral ventricle, grey matter, invaded grey matter, corpus collosum (CC) and invaded corpus collosum (Figure 29). The X-406-GBM brains were so infiltrated with tumor cells that there was no non-invaded tissue to be marked by the pathologist and there was no invaded grey region in the X-312-HGA samples.

After acquisition of the MALDI images, it was then possible to co-register and overlay the marked brain images using Flex Imaging software (Bruker Daltonics). These overlays allowed for the visualization of all the MALDI images and align which spectra came from within the specific regions of brain tissue marked by the neuropathologist. The spectra were then selected, choosing approximately ten spectra per region for each

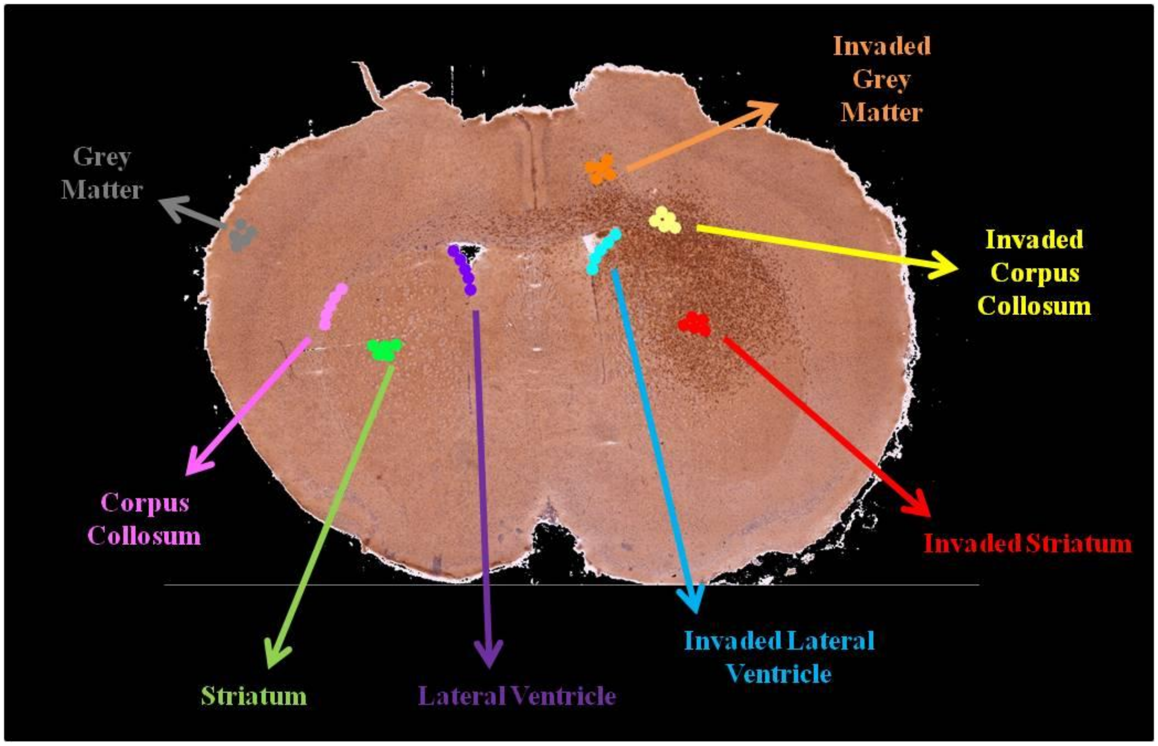

Figure 29: Anti-human nuclear stained brain tissue section from a primary tumor xenograft (X-312-HGA). The section was scanned on a Mirax scanner and then various histological regions were marked by a neuropathologist. Each color represents a different area of the brain: grey matter (grey), invaded grey matter (orange), corpus collosum (pink), invaded corpus collosum (yellow), striatum (green), invaded striatum (red), lateral ventricle (purple) and invaded lateral ventricle (teal).

brain section analyzed, and placed in separate folders for further processing and statistical analysis.

All spectra were processed using ClinPro Tools, commercially available software from Bruker Daltonics. Once the spectra had undergone baseline subtraction, smoothing, normalization, realignment and peak picking, the data for each spectrum was exported collectively into a feature table, which is a list of each *m/z* value and its corresponding intensity value for each spectrum. The mass region evaluated was from *m/z* 3000-30,000 and there was an average of 240 peaks found for each brain region. Using these feature tables, various analyses and statistical tests were performed to evaluate the protein changes that occurred with respect to the cyclopamine treatment.

Comparisons were made for each area of the brain, comparing CYC dosed versus non-dosed samples for both the X-312-HGA and X-406-GBM mouse brains. SAM analysis was performed for each region and resulted in lists of *m/z* values that show a significant difference between the dosed and non-dosed brains. The SAM used a two class unpaired test and significant peaks were identified that had a fold change > 1.25. There were a number of peaks that were changed as a result of the CYC treatment. For the X-312-HGA samples, the invaded CC had 49 (21%), the invaded LV had 121 (48%) and the invaded striatum had 61 (25%) significant peak changes (Table 8). For the X-406-GBM samples, the invaded CC had 54 (23%), the invaded grey had 54 (22%), the invaded LV had 91 (36%) and the invaded striatum had 99 (41%) significant peak changes (Table 8).

Table 8: Significant peak change statistics for the X-312-HGA and X-406-GBM xenograft mice.

NonDosed Versus Dosed							
Fold Change > 1.25		**X-312-HGA**			**X-406-GBM**		
	Total # Peaks	**# Affected Peaks**	**% of peaks changed**	**FDR***	**# Affected Peaks**	**% of peaks changed**	**FDR***
Invaded CC	234	49	21	16.5	54	23	5.2
Invaded Grey	247	N/A	N/A	N/A	54	22	12.1
Invaded LV	254	121	48	22.1	91	36	22.7
Invaded Striatum	244	61	25	14.3	99	41	1.6
CC	230	144	63	9.7	N/A	N/A	N/A
Grey	257	32	12	11.7	N/A	N/A	N/A
LV	229	79	34	26.5	N/A	N/A	N/A
Striatum	228	51	22	8.7	N/A	N/A	N/A

*FDR- False Discovery Rate

There are various ways to look at the significant peak changes when comparing the X-312-HGA (CYC responsive) and X-406-GBM (CYC non-response) xenografts. Appendix B shows that there are some significant features that go up in both xenografts and some that go down in both xenografts. There are also some significant features that go up in one xenograft and down in the other and there are unique significant features to each xenograft. An example of this is displayed in Figure 30 which shows a graphical representation showing the percent change for each *m/z* in a signature of response found for the X-312-HGA responder xenograft tumors in the invaded striatum region. The signals are arranged from greatest negative percent change to greatest positive percent change in the responder profiles. The X-406-GBM non-responder graph displays the same order of features, showing that the majority of the signals do not display a significant change in intensity and some features display an opposite response to the CYC than the X-312-HGA tissues.

Protein identifications were found for 40 of the significant features that were affected by cyclopamine dosing in the X-312-HGA xenografts which showed a survival advantage as a result of treatment. Protein identification was achieved through protein separation/isolation, proteolytic digestion, sequencing of peptides by LC-MS/MS, and matching the peptides to genome-based protein databases. The MALDI peaks identified using these strategies are shown in Table 9. The MW and corresponding identifications are listed along with the percent coverage, modifications, SwissProt Identification number, the number of peptides identified, the intensity trend as a result of CYC dosing and the regions in the brain the features were found.

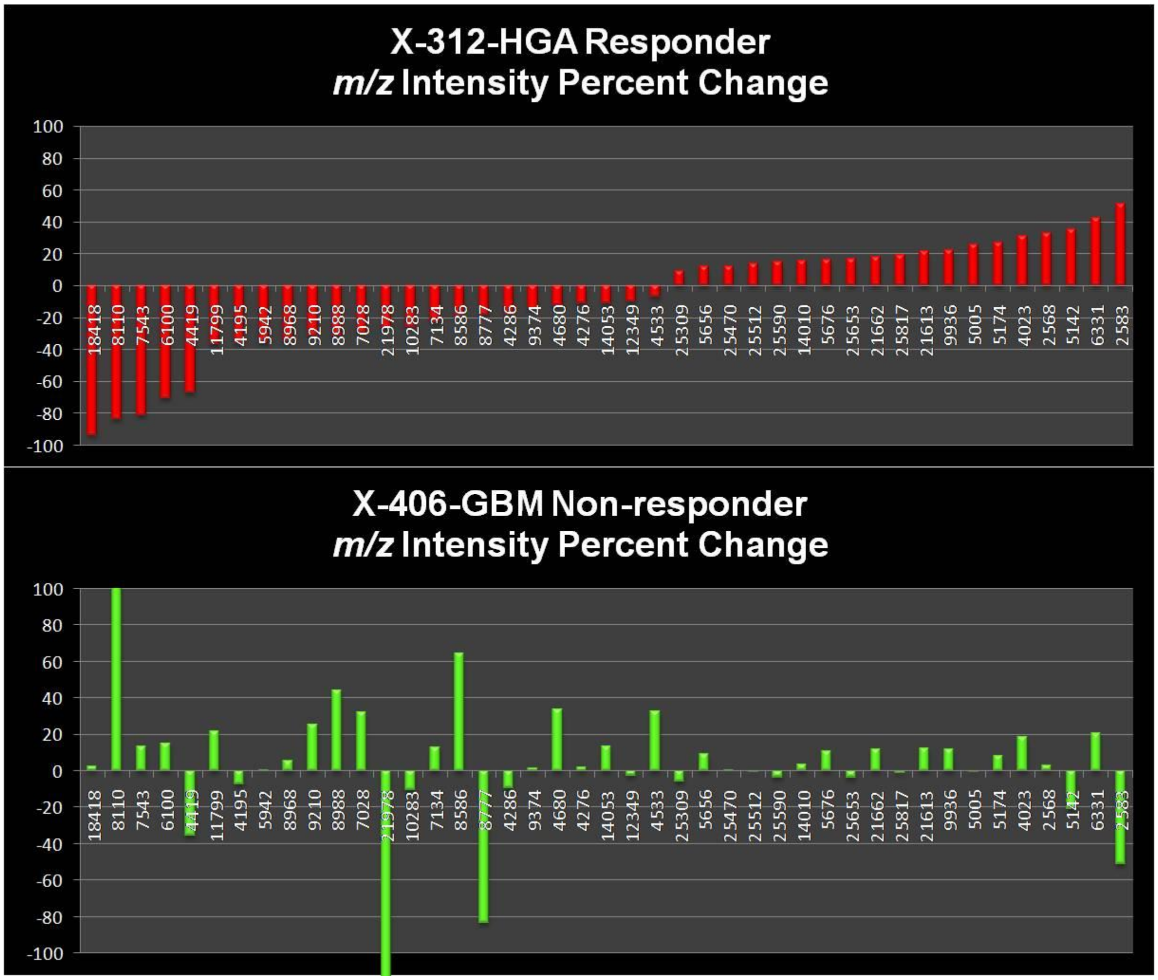

Figure 30: SAM results displayed as bar graphs for the Invaded Striatum of the xenografts comparing CYC dosed versus non-dosed tissues. In the top graph each bar represents the percent change for each *m/z* in a signature of response found for the X-12-HGG responder xenograft tumors. The signals are arranged from greatest negative percent change to greatest positive percent change in the responder profiles. The bottom graph displays the same order of features as the top graph, with each bar representing the percent change for each *m/z* in the X-406-GBM samples. The majority of the signals do not display a significant change in intensity, however, some *m/z* signals display an opposite trend between the responder and non-responder samples. Spectra used in the comparison of treated to non-treated were isolated from the tumor invaded striatum of the brains, as determined by a neuropathologist. Before SAM analysis the spectra were processed (baseline-subtracted, smoothed, normalized and re-aligned).

Table 9: Protein Identifications for Significant Features in the X-312-HGA xenografts (CYC responsive)

m/z	MW (Da)	Protein Name	% Coverage of unprocessed precursor	Modifications (amino acid chain)	Swissprot Primary Accession Number	Number of Peptides	Trend	Brain Region
6722	6807	**Purkinje cell protein 4**	39	*(2-62)	P63054	2	Down^	Invaded Striatum Invaded LV
7342	7338	**Copper transport protein ATOX1**	44	(1-68)	O08997	3	Down^	Invaded Striatum Invaded LV
7359	7446	**Cytochrome b-c1 complex subunit 9**	34	*(2-64)	Q8R1I1	2	Down^	Invaded Striatum Invaded LV
7543	7498	**Myelin basic protein (Isoform 3)**	41	*(1-69)	P04370	5	Down	Invaded Striatum Invaded LV
7960	7960	**cAMP-dependent protein kinase inhibitor alpha**	48	(1-76)	P63248	2	Down^	Invaded LV
8026	7979	**Guanine nucleotide-binding protein G(I)/G(S)/G(O) subunit gamma-13**	13	*(1-67)	Q9JMF3	2	Up	Invaded CC
8110	8236	**ATP synthase subunit e, mitochondrial**	51	(2-71)	Q06185	6	Down	Invaded Striatum Invaded LV
8675	8761	**Probable protein BRICK1**	29	*(2-75)	Q91VR8	2	Down	Invaded LV
9330	9327	**NADH dehydrogenase [ubiquinone] 1 alpha subcomplex subunit 4**	43	(2-82)	Q62425	4	Down^	Invaded Striatum Invaded LV
9639	9768	**Cytochrome b-c1 complex subunit 8**	54	(2-82)	Q9CQ69	3	Down^	Invaded Striatum Invaded LV
9980	10071	**Cytochrome c oxidase subunit 6B1**	38	*(2-86)	P56391	4	Down	Invaded LV
10522	10477	**SH3 domain-binding glutamic acid-rich-like protein 3**	25	*(1-93)	Q91VW3	2	Up	Invaded Striatum Invaded LV
10724	10855	**LYR motif-containing protein 4**	34	(2-91)	Q8K215	3	Up	Invaded CC
10834	10963	**Heat shock protein 1 (Chaperonin 10)**	57	(2-102)	Q4KL76	6	Up^	Invaded Striatum
11086	11083	**Protein S100-A11**	16	(1-98)	P50543	2	Down	Invaded LV
11517	11605	**Cytochrome c, somatic**	32	*(2-105)	P62897	5	Up	Invaded Striatum Invaded LV
11652	11651	**60S acidic ribosomal protein P2**	66	(1-115)	P99027	4	Up^	Invaded Striatum Invaded LV
11545	11675	**Thioredoxin**	38	*(2-105)	P10639	4	Up	Invaded Striatum Invaded LV
11799	11923	**Peptidyl-prolyl cis-trans isomerase FKBP1A**	43	(2-108)	P26883	3	Down	Invaded LV
12137	12136	**Tumor suppressor candidate 2**	32	(1-110)	Q9WVF8	2	Down^	Invaded Striatum Invaded LV

*acetylated N-terminus (+42)

^opposite trend seen in X-406-GBM xenograft samples

Table 9 (continued): Protein Identification for Significant Features in the X-312-HGA xenografts (CYC responsive)

m/z	**MW (Da)**	**Protein Name**	**% Coverage of unprocessed precursor**	**Modifications (amino acid chain)**	**Swissprot Primary Accession Number**	**Number of Peptides**	**Trend**	**Brain Region**
12375	12504	Macrophage migration inhibitory factor	39	(2-115)	P34884	3	Down^	Invaded Striatum Invaded LV
12437	12576	NADH dehydrogenase [ubiquinone] 1 alpha subcomplex subunit 7	19	(2-113)	Q9Z1P6	2	Down^	Invaded LV
13249	13244	UPF0366 protein C11orf67 homolog	21	(1-122)	Q8R0P4	3	Down	Invaded LV
13281	13370	V-type proton ATPase subunit F	39	*(2-119)	Q9D1K2	5	Down^	Invaded LV
13474	13480	Endosomal adaptor protein p14	22	(1-125)	Q9JHS3	2	Down^	Invaded LV
13565	13527	Cytochrome b-c1 complex subunit 7	39	*(1-111)	Q9CQB4	5	Down^	Invaded Striatum Invaded LV
13641	13777	Histidine triad nucleotide-binding protein 1	26	(2-126)	P70349	2	Down^	Invaded LV
14208	14164	NADH dehydrogenase [ubiquinone] 1 subunit C2	24	*(1-120)	Q9CQ54	4	Down^	Invaded CC
14053	14188	Iron-sulfur cluster assembly 1 homolog, mitochondrial	19	(2-129)	Q9D924	2	Down^	Invaded CC
14163	14255	Ribonuclease UK114	65	*(2-135)	P52760	6	Down^	Invaded LV
14136	14275	Programmed cell death protein 5	34	(2-126)	P56812	4	Down^	Invaded CC
15345	15344	FK506-binding protein 2	27	(1-140)	P45878	2	Up	Invaded Striatum Invaded LV Invaded CC
15836	15792	Golgin subfamily A member 7	18	*(1-137)	Q91W53	2	Up^	Invaded Striatum Invaded CC
16230	16228	Actin-related protein 2/3 complex subunit 5	21	(1-151)	Q3TKM9	4	Down	Invaded CC
16299	16301	Ribosomal protein S14	26	(1-151)	O70569	3	Down^	Invaded CC
16396	16353	Vesicle-associated membrane protein 4	22	*(1-141)	O70480	2	Down^	Invaded Striatum Invaded CC
17003	16958	Microsomal glutathione S-transferase 3	21	*(1-153)	Q9CPU4	3	Down^	Invaded LV
18418	18505	Transmembrane protein 35	13	*(2-167)	Q9D328	2	Down	Invaded Striatum Invaded LV Invaded CC
18654	18612	CB1 cannabinoid receptor-interacting protein 1	45	*(1-164)	Q3UFR2	5	Down	Invaded LV
19376	19462	Translationally-controlled tumor protein	21	*(2-172)	P63028	3	Up^	Invaded LV

*acetylated N-terminus (+42)

^opposite trend seen in X-406-GBM xenograft samples

Discussion

Most previously reported methodologies for CYC quantitation involved the use of LC-MS/MS and was shown for concentration in plasma and cultured cells. This study extends on that work to include a methodology to quantify CYC in tissues while maintaining spatial integrity using MALDI and demonstrates for the first time the concentration of CYC in brain tumor xenografts (Table 7). Comparing the concentration values found by the MALDI with the LC-MS/MS method developed for CYC quantitation from tissue shows close similarity. The percent difference in the samples was approximately 35% for the CYC 150 samples and was only 2% for the CYC100 samples. The CYC 50 and Veh samples had CYC concentration below the LOD for the MALDI method and with the LC-MS/MS the CYC 50 cyclopamine concentration was only determined to be 688 ng/g. The low concentration could be due to the fact that the half life of the CYC has been shown to be 4h and the samples were taken 5h post dose. It has been shown that administration of cyclopamine by ip injection caused minimal toxicity at doses of 10 mg/kg and 50 mg/kg while a high dose tested (160 mg/kg) demonstrated toxicity.[142] This study also showed maximum serum concentration (C_{max}) was reached 20 min (T_{max}) following injection of 10 or 50 mg/kg doses with corresponding C_{max} values of 2.58 and 19.9µM, respectively. The terminal elimination half-life of cyclopamine administered ip was 4h.[142]

Cyclopamine has been shown to inhibit the Shh pathway in brain tumor xenografts and confers a survival advantage.[130] By studying the proteomic affects of the CYC dosing on these xenografts, it is possible to see what affects related to the Shh pathway are seen as well as point to other possible biological pathways that are affected. Statistical analysis found numerous protein signals that were affected by the cyclopamine treatment in both the responder X-312-HGA and non-responder X-406-GBM xenografts (Table 8). By focusing on the signals that were altered in the responder xenograft (Table 9), it can help shed insight into how the CYC is inhibiting tumor growth and increasing survival.

Purkinje cell protein 4 was decreased in the CYC dosed X-312-HGA xenograft mice. Shh is produced by Purkinje cells from late embryonic stages of development through to adulthood. The loss of Shh activity influences Purkinje cell development.[143] The inhibition of the Shh pathway would thus affect the expression of the purkinje cell proteins.

Endosomal adaptor protein p14 was found to have a decreased intensity in the treated X-312-HGA samples as compared to the non-treated samples. Endosomal adaptor protein p14 is a regulator of the mTOR pathway, a signaling cascade that regulates both cell growth and cell cycle progression through its ability to integrate signals from amino acids and energy.[144] As part of the Ragulator complex, it recruits the Rag GTPases and the mTORC1 complex to lysosomes, a necessary key step in activation of the TOR signaling cascade by amino acids.[145] The antiproliferative effects of mTOR inhibition has been observed in multiple cancerous cell lines also including inhibition of protein synthesis and induction of apoptosis. The decrease in intensity of the endosomal adaptor protein p14 in the responder xenograft could indicate that cyclopamine serves to inhibit the mTOR pathway and this could be another way that cyclopamine inhibits cell proliferation and reduces tumor size in addition to its Hh inhibiting properties.[146]

Treatment with CYC in the X-312-HGA drug responsive xenograft shows a decrease in S100A11 (Calgizzarin), which is a calcium-binding protein implicated in a variety of biologic functions such as cytoskeleton organization, proliferation and differentiation. Overexpression of S100A11 has been shown in a number of cancers such as prostate,[147] colorectal,[148] pancreatic,[149] and breast[150] suggesting that it may be involved with cancer development and progression. It has been demonstrated that suppression of S100A11 by small interfering RNA (siRNA) led to apoptosis, and that the overexpression of S100A11 inhibited apoptosis in human uterine smooth muscle tumor cells.[151] The proapoptotic effect of calgizzarin downregulation was also shown with TSA treatments antitumoral effect suggested by another study.[152] This indicates that the CYC treatment could be inducing apoptotic pathways in the drug responsive xenografts.

Numerous proteins involved in the electron transport chain were affected by cyclopamine treatment in the X-312-HGA CYC responder xenografts. NADH dehydrogenase [ubiquinone] 1 alpha subcomplex subunit 4 along with subcomplex subunits 4 and 7 are all a part of Complex I. Cytochrome b-c1 complex subunits 7,8 and 9 are a part of Complex III, cytochrome c oxidase subunit 6B1 is a part of Complex IV and ATP synthase subunit 3 is part of Complex V. All of the above mentioned proteins showed a decrease in intensity in the X-312-HGA CYC treated xenografts versus the non-treated xenograft samples. Cytochrome *c*, however, showed an increase in intensity.

As described in Chapter III, the electron transport chain, which is embedded in the inner membrane of the mitochondria, consists of five multi-protein complexes. Complexes I and II oxidize the energy-rich molecules NADH and FADH2, respectively, and transfer the resulting electrons to ubiquinol, which carries it to complex III. Complex

III, in turn, shuttles the electrons across the inner mitochondrial membrane to cytochrome *c*, which carries them to complex IV. Complex IV uses the electrons to reduce oxygen to water. Each electron carrying step uses the resulting energy to pump hydrogen ions into the intermembrane space. This generates a proton gradient, the dissipation of which is used by complex V, or ATPase, to power the phosphorylation of ADP to ATP. Along with carrying electrons, complexes I, II, and III generate reactive oxygen species (ROS), namely superoxide, at low levels.[153]

By inhibiting the electron transport chain, there is a greater generation of ROS which occurs at the tumor mitochondrial membrane.[154] This activates apoptosis by facilitating the release of cytochrome *c* from the inner mitochondrial membrane. Bcl-2 proteins are layered on the surface of the mitochondria, detect damage, and activate a class of proteins called Bax, which punch holes in the mitochondrial membrane, causing cytochrome *c* to leak out. This cytochrome *c* binds to Apaf-1, or apoptotic protease activating factor-1, which is free-floating in the cell's cytoplasm. Using energy from the ATPs in the mitochondrion, the Apaf-1 and cytochrome *c* bind together to form apoptosomes. The apoptosomes bind to and activate caspase-9, another free-floating protein. The caspase-9 then cleaves the proteins of the mitochondrial membrane, causing it to break down and start a chain reaction of protein denaturation and eventually phagocytosis of the cell.[155]

Numerous studies have shown that by inhibiting the complexes of the mitochondrial electron transport chain (most documented for Complex I and III) there is an increase in ROS production and subsequent cell death.[156-158] Recently, several studies have also indicated that ROS may be also involved in induction of autophagy.[159, 160]

Autophagy is a self-digestion process important for cell survival during starvation. It has also been described as a form of programmed cell death. Mitochondria are important regulators of autophagy-induced cell death and damaged mitochondria are often degraded by autophagosomes. The decrease in the ETC complex proteins indicates that CYC is suppressing the ETC system which could be resulting in increased ROS production. This ROS increase is most likely facilitating the increase in cytochrome *c* and subsequent apoptotic mechanisms.

As is evidenced, a number of vital biological processes were affected by the administration of CYC in the X-312-HGA xenografts including ETC function, the mTOR pathway and apoptosis mechanisms. Most of the effects were seen in multiple regions of the invaded brain indicating that the CYC administration has a ubiquitous effect on the tumor cells regardless of their location. Further work is needed to identify all of the molecular features that were altered and fully elucidate what this could mean biologically as well as validate the proteins as viable markers of CYC efficacy. Additional evaluation should also be done to investigate the molecular features that were affected solely in the X-406-GBM samples. These changes could be indicative of affects that are nonspecific to the CYC tumor reducing activity.

MALDI IMS has shown to be a very powerful discovery technique for investigating the molecular effects that cyclopamine administration has in direct human glioma xenografts. The data provides not only information as to the pharmacological response of the CYC but also provides a means to directly correlate drug distribution with these molecular changes and obtain drug concentration information all while maintaining spatial information in the tissue samples.

Materials and Methods

Materials

The MALDI matrices, sinapinic acid and 2,5-dihydroxybenzoic acid, hemotoxylin, cyclopamine, and jervine, normal horse serum, mouse raised anti-human primary antibody, horse raised anti-mouse secondary antibody, DAB solution and DAB buffer, and Avidin and Biotin and Avidin HRP were purchased from Sigma Chemical Co. (St. Louis, MO). Acetic acid, HPLC grade acetonitrile, ethanol, and methanol, Xylene, Para formaldehyde, Triton X100, PBS and Hydrogen Peroxide were purchased from Fisher Scientific (Suwanee, GA).

Tissue Preparation and MALDI Imaging

Tissue was obtained from Dr. Michael Cooper's laboratory (Vanderbilt University, Nashville, TN). CD133-enriched cells (10^4–10^5) were transplanted into the striatum of NOD/SCID mice according to a protocol approved by the Vanderbilt Medical Center IACUC. Mice were anesthetized with ketamine and xylazine, and securely placed on a stereotactic frame. Using aseptic surgical procedures, an incision was made in the scalp and a small burr hole was drilled 2.5 mm lateral to the bregma. CD133-enriched cells were implanted 2.5 mm into the right striatum using a Hamilton syringe. Mice were maintained until development of neurological symptoms or signs of distress.[130] After sacrifice the brains were removed and a sagittal section at Interaural 10.6 mm, Bregma 1.6 mm was cut and flash frozen in liquid nitrogen and stored at -80 °C until further use.

Frozen brain tissues were mounted onto a cryostat chuck with OTC. Tissue was trimmed until an even sagittal section was acquired. From this position sections (12 µm) were collected, one for protein analysis, a serial section for CYC analysis, and another serial section for anti-human nuclear immunohistochemical staining. Sections for protein and CYC analysis were mounted onto gold-coated MALDI targets while the sections for staining were thaw mounted onto glass microscope slides.

Slides were immediately stained, or stored at -20 °C until staining. Slides were put into 4% Paraformaldehyde for 60 minutes at 4 °C before being removed and dried for two minutes at room temperature. Slides were then put into 1x PBS for five minutes then quenched with 1% hydrogen peroxide for 20 minutes. The slides were washed in phosphate buffer solution with triton X (PBST) twice for five minutes before adding a normal blocking horse serum (10% in 0.1% PBST) for 30 minutes. Again the slides were washed in PBST twice for five minutes each wash. An avidin biotin block was done, the slides were washed in PBST before the antibodies were applied. Primary antibody (mouse raised, anti-human) was applied for 8-12 hours at 4 °C, slides were washed in PBST then secondary antibody (horse raised, anti-mouse) was added for two hours at room temperature. Again the slides were washed in PBST. Avidin/HRP was added for one hour, slides were washed in PBST then DAB was added in the dark for 8 minutes. The slides were briefly dipped in water and then Hemotoxylin counterstained before undergoing a series of ethanol washes to dehydrate the slides before rinsing in xylene and then coverslipping.

MALDI targets were placed into a desiccator for at least an hour to dry. To prepare sections for CYC analysis, a matrix solution of CHCA (20 mg/ml, 50%

acetonitrile) was prepared with 2 µM JERV internal standard. Sections were spotted on the Portrait (Flyby 1 drop 20 passes x2) at 300 µm x 300 µm spatial resolution. All CYC images were acquired on a MALDI-LTQ XL (Thermo Scientific Inc.). The MALDI target with sections designated for protein analysis was reagent washed and seeded with finely ground SA. Fresh SA matrix solution was made 60% acetonitrile 40% water 0.02% TFA. The sections were spotted using the Portrait (Flyby 1 drop 30 repeats) in a 300 µm x 300 µm array. Higher spatial resolution images were spotted at 150 µm x 150 µm. The MALDI target was scanned and sections were imaged on an Autoflex (Bruker Daltoniks).

The immunohistochemically stained sections stained were scanned on a Mirax Scanner and .jpeg images were exported. Histological markings were made by a trained neuropathologist (Tye Able) using Mirax Software (Carl Zeiss International). Eight regions were marked, striatum, invaded striatum, lateral ventricle, invaded lateral ventricle, grey matter, invaded grey matter, corpus collosum and invaded corpus collosum. The marked images were then co-registered with the images acquired to extract spectra from isolated histological areas for comparisons and further statistics.

Data Processing

Spectra from each section were kept together in separate folders. These folders were then input into ClinPro Tools where the imported spectra were processed with the following parameters; 1200 Resolution, data reduction factor of 5, Top Hat baselining with 10% Minimal Baseline Width, Savitsky Golay Smoothing enabled at 2 width 10 cycles, recalibration 2000 ppm max peak shift with 20% match to calibrate peaks excluded not re-calibratable spectra, from *m/z* range 3000-20,000, and null spectra exclusion. Once Spectra have been imported into ClinPro Tools and processed peak selection was performed (peak picking on total average spectrum, SN=2, 0% relative threshold to the base peak) and peak list feature tables were output.

Statistical Analysis

SAM was performed to assign a score to each feature on the basis of change in its spectral intensity relative to the standard deviation of repeated measurements. For features with a score greater than a predetermined threshold, SAM uses permutations of the repeated measurements to estimate the percentage of features identified by chance, the false discovery rate [91]. Two by two comparisons were made for each brain region comparing dosed versus non-dosed tissue sections. Both the X-312-HGA (responder) and X-406-GBM (non-responder) xenograft spectra were analyzed.

Drug Quantitation Using LC-MS/MS

The extraction and chromatographic LC-MS/MS protocols used here for were adapted from previous methodologies used for CYC quantitation.[142, 161-163] Cyclopamine and jervine stock solutions were made in MeOH and stored at -20 °C until use. Calibration curves standards were made in control mouse brain homogenate to yield final concentrations of 1000, 100, 10, 1, 0.1, 0.01 ng/ml of CYC. A minimum of 20 mg of tissue was weighed out for sample analysis. The tissue was homogenized with PBS in a 10:1 (ml/mg) ratio until uniform upon visual inspection. The homogenate was sonicated for ten minutes and then centrifuged at 3500 g for 15 minutes and then 4000 g for 15 minutes. Fifty µl of the supernatant was taken and mixed with 25 µl of internal standard (jervine, 1000 ng/ml). For protein precipitation, 250 µl of acetonitrile /ethanol/acetic acid (90/10/0.1) was added and vortex mixed for 20 minutes. The solution was then centrifuged for 15 minutes at 4000 g. Supernatant was transferred to a glass autosampler tube and dried in a vacuum centrifuge (two hours, 40 °C) and then reconstituted in 50% methanol with 0.1% formic acid.

Samples were analyzed on an ESI TSQ Quantum triple-quadrupole system (Thermo Scientific, Waltham, MA) equipped with an autosampler (set at 4 ºC) column oven (50 °C) and HPLC system. A Waters XTerra RP® C18 reverse phase column (2.1 x 100 mm, 5 µm particle) was used with a fast gradient run of mobile phase A (0.1% acetic acid in water) to mobile phase B (0.1% acetic acid in methanol). Ten microliters of sample was injected onto a PEEK loop at a flow rate of 0.3 ml/min at 5% mobile phase B and held for one minute. Over 5 minutes a linear gradient was run from 5%-95% mobile phase B and then held at 95% for one minute. The column was then eluted from 95%-5% over one minute and then held at 5% mobile phase B for two minutes before injection of the next sample. The total run time was ten minutes.

Acknowledgements

Dr. Annurag Sarangi and Dr. Michael Cooper performed the mouse implantation and dosing with cyclopamine. All mice samples and survival study data provided by Dr. Michael Cooper's Lab. All histological markings were made by Dr. Tye Able.

CHAPTER V

CONCLUSIONS AND PERSPECTIVES

The Value of MALDI Imaging in Drug Discovery and Development

Despite the dramatic increase in drug development expenditures over the last decade, the number of new chemical entities has actually decreased. The industry has been troubled by high late-stage attrition rates and safety issues, creating a major problem not only for drug developers, but also for regulatory agencies, patients, and society in general. Current methodologies involved with drug discovery and development are clearly in need of assistance. New approaches and new science are needed to transform drug development.

It has been shown that MS plays a role in all aspects of the drug discovery and development process. Current mass spectrometry technologies are applied in ADME screening for lead compound optimization, drug quantification in PK studies, drug metabolite identification in animals and humans, as well as PD bioanalysis in both clinical and toxicology studies.[164] The technology's value spans the entire drug pipeline. It has been said that MS has become almost a cornerstone of modern drug discovery and development, from target identification and validation up to combinatorial chemistry and parallel synthesis chemistry. MS is seen in everything from new chemical entities to formula determination to target profiling and preclinical studies. It is even seen at the far end, in manufacturing and many researchers are working to bring mass spectrometry into diagnostics.[10, 164]

Throughout the course of this research it has been demonstrated how MALDI IMS can extend the use of MS in drug discovery and development even further by introducing a new method for sample analysis. A MALDI IMS protocol was developed for absolute quantitation of small molecules directly from tissue sections (Chapter II). This protocol allows for MALDI based imaging technologies to correlate absolute drug concentration with pharmacological response in tissues while still maintaining spatial information in rapid, high-throughput molecularly specific experiments as demonstrated in Chapters III and IV.

Imaging experiments performed by MALDI were able to provide the individual, label-free temporal distributions of OLZ, IMAT and CYC from brain tissue sections with high sensitivity and reproducibility. Highly-accurate absolute quantities of each compound were also obtained directly from tissue sections without the need for homogenization or extraction procedures. This proves advantageous over LC-MS/MS techniques in that spatial information is retained, sample preparation as well as sample analysis is quicker and there is less chance of losing quantities of the small molecule being investigated during the preparation or analysis processes. The use of this technology could be implemented in early phases of pre-clinical trials to assist with PK studies in animal models.

Using the calculated drug concentrations of IMAT and CYC, it was possible to study the proteome affects that the drug presence had on primary brain tumor xenografts in mice. With the ultimate goal of PD studies being to relate the pharmacological response to dose-concentration or concentration-effect relationships of a therapeutic compound, MALDI IMS proved to be an invaluable tool to rapidly and reproducibly relate the tissue distribution of the IMAT and CYC to the observed pharmacological response within the same tissue sample while maintaining spatial resolution.

Altered proteins were identified that are involved in a number of different biological pathways, such as the ETC, apoptosis mechanisms, proliferation, cell cycle regulation and pre-mRNA splicing. Future studies about the biological implications of the perturbation in expression of these proteins may also facilitate the discovery of additional molecular pathways that are altered by IMAT and CYC in primary brain tumors. This may contribute to an improved understanding of the IMAT and CYC mechanisms of action within the tumors or provide new possible drug targets for the development of additional therapies. Taken together, the pharmacoproteomic profiling could constitute a valuable tool for the identification of drug-responsive biomarkers and for the establishment of a molecular basis for developing novel and more effective approaches for therapeutic intervention. The biological information obtained could also help gain a deeper understanding of the mechanisms involved in primary brain tumor function.

Future Research Directions

As is important to all new technologic methods to be used in clinical research, issues related to quality control, standardization, specimen choice and collection, result interpretation and validation all need to be taken into consideration. Publication is only the first step in acceptance and utilization of a new approach. A key hurdle in this process is the ability to bridge the pre-clinical trials into a positive clinical trial outcome.

With the push towards personalized medicine, the requirement for accurate molecular diagnostics for the characterization of human disease to deliver the most effective therapies is driving research towards developing more and novel biomarkers.[165] Typical approaches towards the discovery and validation of these biomarkers involve initial studies *in vitro*, followed by *in vivo* studies with small animal molecules before progressing to clinical studies in humans.[165] MALDI IMS technologies and methods have become key in the discovery and utilization of biomarkers for disease diagnosis, prognosis and compound efficacy determination that are relevant to human disease.

Pairing the analysis of mouse model samples with patient samples of the same disease will improve the ability to find viable and accurate biomarkers. As described in Chapter IV, the mouse xenografts used were developed directly from patient biopsy samples. Recapitulation of the malignant glioma pathological features was observed and gliomaspheres generated from the tissues demonstrated active biological activity that was also seen in the xenograft models[130] This shows that the xenografts are very good representations of the brain tumor diseases that were present in the patients.

MALDI IMS techniques were used to analyze sections of the patient biopsies that were used to develop the xenografts. Frozen biopsy tissues were sectioned on a cryostat at 12 µm, mounted onto target slides, washed, dried, spotted using the Portrait with SA and analyzed using a MALDI TOF. Images were visualized using Flex Imaging software (Bruker Daltoniks). Significant features found in the xenografts (Chapter IV) were looked for in the biopsy samples. Multiple signals were found that corresponded to both a CYC response in the xenograft mice and presence in the patient biopsies. As is seen in Figure 31, the *m/z* signal 7008 is visualized in the xenograft tissue sections as well as the patient biopsy that the xenografts were derived from for the 312-HGA sample. This signal shows a decrease in intensity as a result of CYC treatment in the X-312-HGA tissues. These preliminary results point to the usefulness of MALDI IMS in helping correlate potential biomarkers from preclinical mouse models to use in patient trials.

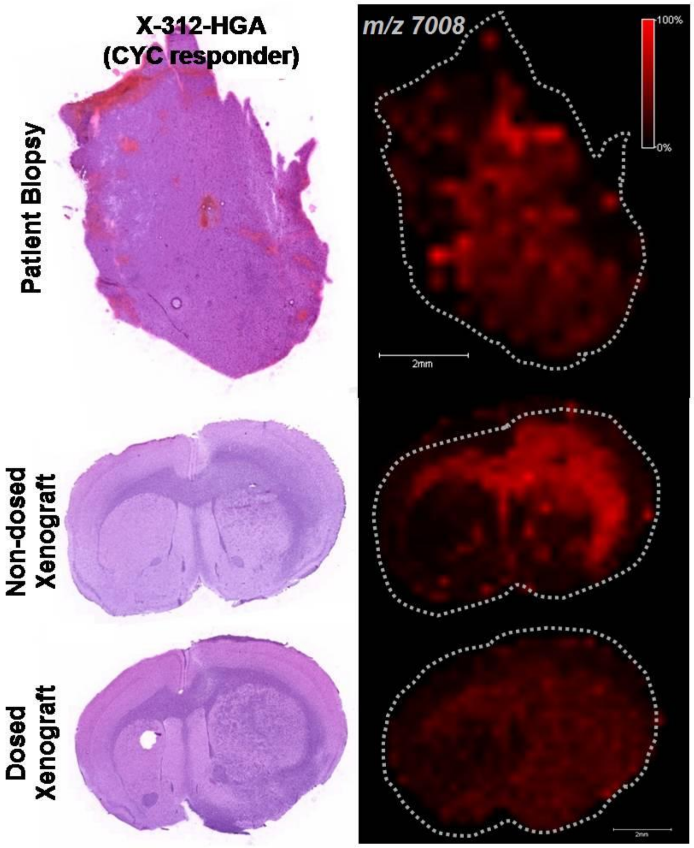

Figure 31: Correlation of *m/z* features in biopsy and xenograft tissues. The H&E stains on the left correspond to the patient biopsy and CYC treated and non-treated xenograft brain sections of 312-HGA (CYC responder). The right-hand MALDI images show *m/z* 7008 spatial distribution. As a result of drug treatment this signal intensity is decreased in the xenograft mouse models.

Future work in pursuing the validation of biomarkers discovered by MALDI IMS and elucidating the biological implications these biomarkers have will provide invaluable information for the progression of drug development and discovery advances. The MALDI IMS methodology developed in this study for the direct quantitation of small molecules from tissue sections and evaluation for markers of drug response is a significant step towards improving the productivity of pharmaceutical research. With a more focused understanding of the molecular events that lead to a drug candidate’s efficacy or potential side effects that can be gained by an IMS analysis, the pharmaceutical industry will have the capacity to deliver valuable new therapies to the public, extending and improving patients’ lives safely and more effectively.

APPENDIX A:

PROTOCOL: QUANTITATION OF SMALL MOLECULES WITH MALDI IMS

1.0 Scope:

This procedure describes the steps used to achieve small molecule quantitation directly from tissue sections using MALDI IMS without the need for additional sample treatment or separation techniques. Briefly, the protocol involves the preparation of a calibration curve, calculation of the amount of sampled tissue, robotic sample preparation combined with automated MALDI-TOF mass spectrometry and ultimately determination of small molecule concentration in the tissue.

2.0 Definitions:

N/A

3.0 Health and Safety

Wear gloves, safety glasses, and buttoned lab coat. Precaution should be taken when handling tissue, especially human, and when making solutions. The Portrait and MALDI LTQ have moving parts and care should be taken during sample loading and unloading.

4.0 Equipment and Materials

4.1 Instruments

4.1.1 Portrait 630™ (Labcyte Inc.)

4.1.2 Leica CM3050s cryomicrotome (Leica Microsystems, Inc., Germany)

4.1.3 Flatbed Scanner (Epson)

4.1.4 Olympus BX50 microscope (Olympus Optical Co, LTD. Tokyo, Japan,) fitted with a Micropublisher 3.3 camera (QImaging, Canada)

4.1.5 MALDI LTQ XL (Thermo Scientific Inc.)

4.1.6 Microbalance

4.2 Reagents

4.2.1 Water: (H2O), Milli-Q System water (18 mega-ohm, TOC < 10 ppb)

4.2.2 Methanol, HPLC grade

4.2.3 2,5-dihydodroxybenzoic acid (DHB)

4.3 Supplies

4.3.1 *Eppendorf* tubes: Safe-Lock microcentrifuge tube, 1.5 ml

4.3.2 Pipette and tips

4.3.3 Vortex mixer

4.3.4 Weigh paper

4.3.5 Gold-coated MALDI targets

4.3.6 Microscope slides and coverslips

4.3.7 Dessicator

5.0 Procedure

5.1 Calibration Standard Preparation

5.1.1 Prepare standards as stock solutions (1mg/ml) in methanol. Store at -20 °C.

5.1.2 From the 1 mg/ml stock, prepare a dilution series in methanol spanning six orders of magnitude:

1 ng/ml, 10 ng/ml, 100 ng/ml, 1000 ng/ml, 10,000 ng/ml, 100,000 ng/ml

5.1.3 Prepare 10 ml of DHB matrix solution: 40 mg/ml, 50 % methanol: 50% water.

5.1.4. Add 100 µl of the appropriate dilution series stock to 900 µl of the matrix to generate the following calibration curve of standard in matrix:

0.1 ng/ml, 1 ng/ml, 10 ng/ml, 100 ng/ml, 1,000 ng/ml and 10,000 ng/ml.

5.1.5 Add the internal standard to each calibration curve solution to result in a 2 µM concentration.

5.2 Spotting the Calibration Curve

5.2.1 Cut control fresh frozen tissue sections at 12 µm thickness at -20 ºC using a Leica CM3050s cryomicrotome (Leica Microsystems, Inc., Germany). Thaw-mount the sections onto gold-coated MALDI target plates.

5.2.2 Place plates into dessicator for 60 minutes to allow drying.

5.2.3 Spot calibration curve standard matrices on an acoustic reagent multi-spotter (Portrait™ 630, Labcyte Inc). Spot each standard in a in a 300 µm x 300 µm spatial array resulting in a 20 x 10 spot grid on the tissue. Use the conditions 40 passes, 1 drop/pass, 90 sec between pass wait-time, resulting in a total of 6.8 nl deposited per spot.

5.2.4 Knowing the volume of matrix standard deposited it is possible to calculate the amount of drug compound that was deposited onto the tissue within the matrix spot. For the standard curve the amount of drug within the matrix spots is 68000, 6800, 680, 68, 6.8 and 0.68 femtograms (fg) and a blank standard.

5.3 Calibration Curve Acquisition

5.3.1 Allow plates to dry for a minimum of 15 minutes before introducing them into a MALDI LTQ XL (Thermo Scientific Inc.).

5.3.2 For each standard a minimum of 10 spots need to be analyzed. Acquisition parameters for each spot use a 50 µm raster at 14 different positions across the matrix spot, 2 scan events per position (one for the drug, one for the internal standard) alternated for a total of 40 scan events per position, 3 µscans per scan event, 5 laser shots per µscan at a laser power of 20 µJ. This results in a total of 600 laser shots per position. The intensities of the major SRM fragment for both the drug and the internal standard are monitored.

5.3.3 For each matrix spot the sum of the intensities for the drug signal is divided by the sum of the intensities for the internal standard signal. (Spectral intensities are exported using in-house software developed by Surendra Dasari)

5.3.4 Plot the calibration curve using signal ratios vs. amount of drug. A line or curve is fit to the data.

5.4 Tissue Area Determination

5.4.1 Section tissue to be analyzed at 12 µm on a cryomicrotome. Thaw mount sections onto glass slides.

5.4.2 Stain tissue sections using the Hemotoxylin and Eosin staining protocol. (Protocol MSRC-R-004)

5.4.3 Using a flatbed scanner, scan an image of the slide with the stained tissue sections along with an object of known dimensions (for example a measurement slide with various shapes of known area) within the same image.

5.4.4 Import image into Adobe Photoshop and calculate the area of the tissue section.

5.4.4 Repeat with multiple tissue sections. Take the average of the results.

5.5 Tissue Mass Determination

5.5.1 Obtain the mass for a piece of weigh paper on a microbalance.

5.5.2 Cut ten sections at 12 µm thickness of the tissue to be analyzed and place onto the weigh paper.

5.5.3 Immediately obtain the mass for the weigh paper with tissue sections on a microbalance.

5.5.4 Subtract the mass of the weigh paper alone from the mass of the weigh paper with the tissue sections. Divide this number by ten. This results in the mass for one 12 µm thick tissue section.

5.5.5 Repeat this process five times. Take the average of the results.

5.6 Laser Spot Size Determination

5.6.1 Coat a MALDI target with DHB matrix by sublimation (Protocol MSRC-R-025).

5.6.2 Insert plate into instrument to MALDI LTQ XL (Thermo Scientific Inc.).

5.6.3 Using the acquisition parameters to be used for the experiment, fire the laser at areas of the sublimed matrix to create multiple burn patterns for laser spot size measurement. (40 scan events per position, 3 µscans per scan event, 5 laser shots per µscan at a laser power of 20 µJ resulting in 600 laser shots per position).

5.6.4 Take the plate to an Olympus BX50 microscope (Olympus Optical Co, LTD. Tokyo, Japan,) fitted with a Micropublisher 3.3 camera (QImaging, Canada) at 10x magnification. Acquire pictures of the laser spot burn patterns at 10x magnification.

5.6.5 Use the Image Pro Plus software to measure the area of the laser spot burn patterns. This represents the area of the acquisition spot during the tissue analysis.

5.7 Calculate the Amount of Tissue Sampled

5.7.1 To calculate the amount of tissue that is sampled within one area of acquisition, use the following equation:

Area of tissue section/Mass of tissue section = Area of Acquisition spot/Mass of Acquisition spot

5.8 Dosed Tissue Analysis

5.8.1 Section dosed tissues at 12 µm thickness at -20 ºC using a Leica CM3050s cryomicrotome (Leica Microsystems, Inc., Germany) and thaw mounted onto gold-coated MALDI plates.

5.8.2 Place plates into a dessicator for an hour to dry.

5.8.3 Spot tissue sections with DHB matrix spiked with 2 µM of internal standard using the acoustic reagent multi-spotter (Portrait™ 630, Labcyte Inc.) A total of 6.8 nl of matrix deposited per spot (40 passes, 1 drop/pass, 170 pl/drop, 90 sec between pass wait time) in a 300 µm x 300 µm spatial array resulting in a 20 x 10 spot array.

5.8.4 Allow plates to dry for a minimum of 15 minutes before introducing them into a MALDI LTQ XL (Thermo Scientific Inc.).

5.8.5 Analyze a minimum of 10 matrix spots. Acquisition parameters for each spot use a 50 µm raster at 14 different positions across the matrix spot, 2 scan events per position (one for the drug, one for the internal standard) alternated for a total of 40 scan events per position, 3 µscans per scan event, 5 laser shots per µscan at a laser power of 20 µJ resulting in 600 laser shots per position. The intensities of the major SRM fragment for both the drug and the internal standard are monitored.

5.8.6 For each matrix spot the sum of the intensities for the drug signal is divided by the sum of the intensities for the internal standard signal. (Spectral intensities are exported using in-house software developed by Surendra Dasari)

5.9 Calculate the Drug Concentration in the Dosed Tissue

5.9.1 Use the calibration curves linear equation and plug in the signal intensity ratios to obtain the amount of drug present at each location.

5.9.2 Divide the amount of drug present at the location by the mass of the tissue at the location resulting in the concentration of drug within the tissue analyzed.

6.0 References:

Protocol MSRC-R-004

Protocol MSRC-R-025

APPENDIX B:

SIGNIFICANT FEATURE CHANGES AS A RESULT OF CYCLOPAMINE TREATMENT IN THE X-312-HGA AND X-402-GBM XENOGRAFTS

Up in X-312-HGA only

Invaded CC	Invaded Grey	Invaded LV	Invaded Striatum
3289		3826	3271
4620		5132	3391
4941		6177	4532
5027		7655	7654
5045		7683	7683
5065		10345	9406
5211		10522	11517
6684		10630	11545
6762		10662	11733
6802		10744	15345
7420		11388	15619
7654		11472	
7683		11517	
7797		11545	
7837		11652	
7897		15618	
7918			
7939			
7960			
7984			
8026			
10420			
10724			
10744			
15016			
15345			
15621			

Down in X-312-HGA only

Invaded CC	Invaded Grey	Invaded LV	Invaded Striatum
7008		4251	4180
7134		4284	7542
9212		4303	8108
12225		4418	8949
16230		4901	8986
18417		5330	13565
		5400	18417
		5598	
		5694	
		5899	
		6225	
		6278	
		6291	
		6650	
		6683	
		6783	
		6800	
		6826	
		7342	
		7359	
		7418	
		7542	
		7859	
		7937	
		8108	
		8605	
		8659	
		8675	
		8774	
		8791	
		8949	
		8986	
		9193	
		9980	
		11086	
		11794	
		12514	
		13249	
		13443	
		18417	
		18654	

Up in X-406-GBM only

Invaded CC	Invaded Grey	Invaded LV	Invaded Striatum
4964	5062		4940
5448	9914		4964
5484	9960		5005
6576	10017		5756
7008	10054		5794
7028	10165		6050
7342	10185		6070
7359	10204		6254
8383	11308		6312
8480	12437		6651
8494	13690		7382
8568	13909		7755
9914	14010		7797
9960	14052		7835
11195	14136		8027
11312	14208		8298
12137	15011		8606
12179	15617		9914
16794	15840		12179
17003	16299		12437
	16396		12602
			12645
			14049
			15014
			16794
			17003

Down in X-406-GBM only

Invaded CC	Invaded Grey	Invaded LV	Invaded Striatum
3042	3752	3238	3215
4458	3826	3438	4052
4771	3877	3934	4304
5320	3898	4474	4329
5600	5317	4767	4338
5900	5756	5045	4388
6444	6312	5268	4419
6704	7654	6444	4769
7246	7683	6951	5046
7506	7754	7069	5062
8647	7797	10185	5269
8776	8026	10203	5317
8840	8107	15012	6369
9081	8143	15849	6443
9781	8198		7198
10095	8237		7506
10844	8297		8774
12772	8339		10055
	8494		10163
	8774		10185
	8985		10203
	9081		10299
	9244		10375
	10469		10469
	10630		12772
	12601		
	17203		

Up in X-312-HGA and Down in X-406-GBM

Invaded CC	Invaded Grey	Invaded LV	Invaded Striatum
7668		3898	7179
10469		6121	7246
10630		7506	10095
15836		7668	10132
		7754	10345
		8289	10522
		9914	10630
		10055	10744
		10095	10834
		10133	11652
		10163	15843
		12000	
		12644	
		13693	
		13905	
		14129	
		14163	
		15345	
		17203	
		19376	

Down in X-312-HGA and Up in X-406-GBM

Invaded CC	**Invaded Grey**	**Invaded LV**	**Invaded Striatum**
7071		3877	5448
13909		5448	5484
14010		5484	5522
14052		5504	6542
14136		5522	6576
14208		5734	6614
16299		5756	6684
16396		5794	6702
16611		6050	6722
		6070	6760
		6254	6783
		6312	6800
		6542	6826
		6576	7319
		6614	7342
		6702	7359
		6722	7418
		6760	8340
		7319	8383
		7797	8398
		7835	8455
		7960	8480
		7980	8494
		8027	8527
		8064	8568
		8340	9330
		8383	9623
		8398	9639
		8494	12135
		8527	12375
		8568	14136
		9330	16396
		9535	
		9623	
		9639	
		12135	
		12172	
		12375	
		12437	
		12485	
		12581	
		12602	
		13281	
		13474	
		13565	
		13641	
		16794	
		17003	

Up in Both

Invaded CC	Invaded Grey	Invaded LV	Invaded Striatum
5006			

Down in Both

		9081	8792

LITERATURE CITED

1. Kennedy, T., Managing the drug discovery/development interface. *Drug Discovery Today* **1997,** *2* (10), 436-444.

2. *Drug Discovery Handbook*. John Wiley & Sons, Inc.: 2005.

3. Fee, R., The Cost of Clinical Trials. *Drug Discovery and Development* 2007.

4. Novartis www.novartis.com/research/drug-discovery.shtml. (accessed 9/17/2010).

5. Canavan, N., Warning!...Warning! *Drug Discovery and Development* 2007.

6. FDA Investigational New Drug (IND) Application. (accessed 9-17-2010).

7. Health, U. S. N. I. o. ClinicalTrials.gov. (accessed 9/17/2010).

8. FDA New Drug Application. (accessed 9-17-2010).

9. Rieke, G. H., Detection of Light: From the Ultraviolet to the Submillimeter. 2nd edition ed.; NY Cambridge University Press: New York, 2003. http://www.netlibrary.com.proxy.library.vanderbilt.edu/Reader/.

10. Gwynne, P.; Heebner, G., Mass Spectrometry in Drug Discovery and Development: From Physics to Pharma. *Science* 2006.

11. Cox, K. A.; White, R. E.; Korfmacher, W. A., Rapid determination of pharmacokinetic properties of new chemical entities: In vivo approaches. *Combinatorial Chemistry & High Throughput Screening* **2002,** *5* (1), 29-37.

12. Poon, G. K.; Kwei, G.; Wang, R.; Lyons, K.; Chen, Q.; Didolkar, V.; Hop, C., Integrating qualitative and quantitative liquid chromatography/tandem mass spectrometric analysis to support drug discovery. *Rapid Communications in Mass Spectrometry* **1999,** *13* (19), 1943-1950.

13. Ma, S. G.; Chowdhury, S. K.; Alton, K. B., Application of mass spectrometry for metabolite identification. *Current Drug Metabolism* **2006,** *7* (5), 503-523.

14. Chen, Y.; Monshouwer, M.; Fitch, W. L., Analytical tools and approaches for metabolite identification in early drug discovery. *Pharmaceutical Research* **2007,** *24* (2), 248-257.

15. Briggs, D.; Hearn, M. J., Sub-micron molecular imaging-A viability study by Time-of-Flight SIMS. *Surface and Interface Analysis* **1988,** *13* (4), 181-&.

16. Levisetti, R., Recent Applications of High-Resolution Secondary-Ion-Mass-Spectrometry Imaging Microanalysis *Vacuum* **1990,** *41* (7-9), 1598-1600.

17. Matsuo, J.; Ninomiya, S.; Yamada, H.; Ichiki, K.; Wakamatsu, Y.; Hada, M.; Seki, T.; Aoki, T., SIMS with highly excited primary beams for molecular depth profiling and imaging of organic and biological materials. *Surface and Interface Analysis 42* (10-11), 1612-1615.

18. Dass, C., Principles and Practice of Biological Mass Spectrometry. **2001**.

19. Schwartz, S. A.; Reyzer, M. L.; Caprioli, R. M., Direct tissue analysis using matrix-assisted laser desorption/ionization mass spectrometry: practical aspects of sample preparation. *Journal of Mass Spectrometry* **2003,** *38* (7), 699-708.

20. Chaurand, P.; Schwartz, S. A.; Caprioli, R. M., Profiling and imaging proteins in tissue sections by MS. *Analytical Chemistry* **2004,** *76* (5), 86A-93A.

21. Chaurand, P.; Schwartz, S. A.; Billheimer, D.; Xu, B. G. J.; Crecelius, A.; Caprioli, R. M., Integrating histology and imaging mass spectrometry. *Analytical Chemistry* **2004,** *76* (4), 1145-1155.

22. Aerni, H. R.; Cornett, D. S.; Caprioli, R. M., Automated acoustic matrix deposition for MALDI sample preparation. *Analytical Chemistry* **2006,** *78* (3), 827-834.

23. Groseclose, M. R.; Andersson, M.; Hardesty, W. M.; Caprioli, R. M., Identification of proteins directly from tissue: in situ tryptic digestions coupled with imaging mass spectrometry. *Journal of Mass Spectrometry* **2007,** *42* (2), 254-262.

24. Baluya, D. L.; Garrett, T. J.; Yost, R. A., Automated MALDI matrix deposition method with inkjet printing for imaging mass spectrometry. *Analytical Chemistry* **2007,** *79* (17), 6862-6867.

25. Guo, J. In *Discovery of Biomarkers for Endometria Carcinoma by Direct Profiling of Proteins in Tissue Sections*, ASMS, San Antonio, TX, San Antonio, TX, 2005.

26. Schuerenberg, M.; Luebbert, C.; Deininger, S.-O.; Ketterlinus, R.; Detlev; Suckau, D., MALDI tissue imaging: mass spectrometric localization of biomarkers in tissue slices. *Nature Methods* **2007,** *4* (5), iii.

27. Nye, G. J.; Norris, J. L.; Nickerson, S. In *Optimization of the Performance of Automated Matrix Spraying for MALDI Imaging Mass Spectrometry*, ASMS, Seattle, WA, Seattle, WA, 2006.

28. Mamyrin, B. A., Laser assisted reflectron time-of-flight mass spectrometry. *International Journal of Mass Spectrometry and Ion Processes* **1994,** *131*, 1-19.

29. Khatib-Shahidi, S.; Andersson, M.; Herman, J. L.; Gillespie, T. A.; Caprioli, R. M., Direct molecular analysis of whole-body animal tissue sections by imaging MALDI mass spectrometry. *Analytical Chemistry* **2006,** *78* (18), 6448-6456.

30. Li, Y.; Shrestha, B.; Vertes, A., Atmospheric pressure molecular imaging by infrared MALDI mass spectrometry. *Analytical Chemistry* **2007,** *79* (2), 523-532.

31. McLean, J. A.; Ridenour, W. B.; Caprioli, R. M., Profiling and imaging of tissues by imaging ion mobility-mass spectrometry. *Journal of Mass Spectrometry* **2007,** *42* (8), 1099-1105.

32. Taban, I. M.; Altelaar, A. F. M.; Van der Burgt, Y. E. M.; McDonnell, L. A.; Heeren, R. M. A.; Fuchser, J.; Baykut, G., Imaging of peptides in the rat brain using MALDI-FTICR mass spectrometry. *Journal of the American Society for Mass Spectrometry* **2007,** *18* (1), 145-151.

33. Altelaar, A. F. M.; Taban, I. M.; McDonnell, L. A.; Verhaert, P.; de Lange, R. P. J.; Adan, R. A. H.; Mooi, W. J.; Heeren, R. M. A.; Piersma, S. R., High-resolution MALDI imaging mass spectrometry allows localization of peptide distributions at cellular length scales in pituitary tissue sections. *International Journal of Mass Spectrometry* **2007,** *260* (2-3), 203-211.

34. Verhaert, P. D.; Conaway, M. C. P.; Pekar, T. M.; Miller, K., Neuropeptide imaging on an LTQ with vMALDI source: The complete 'all-in-one' peptidome analysis. *International Journal of Mass Spectrometry* **2007,** *260* (2-3), 177-184.

35. DeKeyser, S. S.; Kutz-Naber, K. K.; Schmidt, J. J.; Barrett-Wilt, G. A.; Li, L. J., Imaging mass spectrometry of neuropeptides in decapod crustacean neuronal tissues. *Journal of Proteome Research* **2007,** *6* (5), 1782-1791.

36. Hanahan, D.; Weinberg, R. A., The hallmarks of cancer. *Cell* **2000,** *100* (1), 57-70.

37. Stoeckli, M.; Chaurand, P.; Hallahan, D. E.; Caprioli, R. M., Imaging mass spectrometry: A new technology for the analysis of protein expression in mammalian tissues. *Nature Medicine* **2001,** *7* (4), 493-496.

38. Reyzer, M. L.; Caldwell, R. L.; Dugger, T. C.; Forbes, J. T.; Ritter, C. A.; Guix, M.; Arteaga, C. L.; Caprioli, R. M., Early changes in protein expression detected by mass spectrometry predict tumor response to molecular therapeutics. *Cancer Research* **2004,** *64* (24), 9093-9100.

39. Chaurand, P.; Sanders, M. E.; Jensen, R. A.; Caprioli, R. M., Proteomics in diagnostic pathology - Profiling and imaging proteins directly in tissue sections. *American Journal of Pathology* **2004,** *165* (4), 1057-1068.

40. Johnson, M. D.; Floyd, J. L.; Caprioli, R. M., Proteomics in Diagnostic Neuropathology. *Journal of Neuropathology and Experimental Neurology* **2006,** *65* (9), 837-845.

41. Schwamborn, K.; Krieg, R. C.; Reska, M.; Jakse, G.; Knuechel, R.; Wellmann, A., Identifying prostate carcinoma by MALDI-Imaging. *International Journal of Molecular Medicine* **2007,** *20,* 155-159.

42. Walgren, J. L.; Thompson, D. C., Application of proteomic technologies in the drug development process. *Toxicology Letters* **2004,** *149* (1-3), 377-385.

43. Lewin, D. A.; Weiner, M. P., Molecular biomarkers in drug development. *Drug Discovery Today* **2004,** *9* (22), 976-983.

44. Rudin, M.; Rausch, M.; Stoeckli, M., Molecular imaging in drug discovery and development: Potential and limitations of nonnuclear methods. *Molecular Imaging and Biology* **2005,** *7* (1), 5-13.

45. Hsieh, Y.; Chen, J.; Korfmacher, W. A., Mapping pharmaceuticals in tissues using MALDI imaging mass spectrometry. *Journal of Pharmacological and Toxicological Methods* **2007,** *55* (2), 193-200.

46. Meistermann, H.; Norris, J. L.; Aerni, H.-R.; Cornett, D. S.; Friedlein, A.; Erskine, A. R.; Augustin, A.; De Vera Mudry, M. C.; Ruepp, S.; Suter, L.; Langen, H.; Caprioli, R. M.; Ducret, A., Biomarker discovery by imaging mass spectrometry: Transthyretin is a biomarker for gentamicin-induced nephrotoxicity in rat. *Mol Cell Proteomics* **2006**, M500399-MCP200.

47. Chandana, S.; Movva, S.; Arora, M.; Singh, T., Primary Brain Tumors in Adults. *American Family Physician* **2008,** *77* (10), 1423-1430.

48. Laerum, O. D.; Bjerkvig, R.; Steinsvag, S. K.; Ridder, L. d., Invasiveness of primary brain tumors. *Cancer Metastasis Reviews* **1984,** *3,* 223-236.

49. Cunliffe, C. H.; Fischer, I.; Parag, Y.; Fowkes, M. E., State-of-the-Art Pathology: New WHO Classification, Implications, and New Developments. *Neuroimaging Clinics of North America 20* (3), 259-271.

50. Janny, P.; Cure, H.; Mohr, M.; Heldt, N.; Kwiatkowski, F.; Lemaire, J. J.; Plagne, R.; Rozan, R., Low grade supratentorial astrocytomas. Management and prognostic factors. Wiley Subscription Services, Inc., A Wiley Company: 1994; Vol. 73, pp 1937-1945.

51. Piepmeier, J.; Christopher, S.; Spencer, D.; Byrne, T.; Kim, J.; Knisel, J. P.; Lacy, J.; Tsukerman, L.; Makuch, R., Variations in the Natural History and Survival of Patients with Supratentorial Low-grade Astrocytomas. *Neurosurgery* **1996,** *38* (5), 872-879.

52. Frueh, F. W., A New Approach for Clinical Trials. *Drug discovery and Development* 2010.

53. Atkinson Jr, A. J.; Colburn, W. A.; DeGruttola, V. G.; DeMets, D. L.; Downing, G. J.; Hoth, D. F.; Oates, J. A.; Peck, C. C.; Schooley, R. T.; Spilker, B. A.; Woodcock, J.; Zeger, S. L., Biomarkers and surrogate endpoints: preferred definitions and conceptual framework. *Clincial Pharmacology & Therapeutics* **2001,** *69*, 89-95.

54. Zhang, H.; Chan, D. W., Cancer biomarker discovery in plasma using a tissue-targeted proteomic approach. *Cancer Epidemiol Biomarkers Prev* **2007,** *16* (10), 1915-7.

55. Simpson, R. J.; Bernhard, O. K.; Greening, D. W.; Moritz, R. L., Proteomics-driven cancer biomarker discovery: looking to the future. *Curr Opin Chem Biol* **2008,** *12* (1), 72-7.

56. Etzioni, R.; Urban, N.; Ramsey, S.; McIntosh, M.; Schwartz, S.; Reid, B.; Radich, J.; Anderson, G.; Hartwell, L., The case for early detection. *Nat Rev Cancer* **2003,** *3* (4), 243-52.

57. Nolen, B. M.; Marks, J. R.; Ta'san, S.; Rand, A.; Luong, T. M.; Wang, Y.; Blackwell, K.; Lokshin, A. E., Serum biomarker profiles and response to neoadjuvant chemotherapy for locally advanced breast cancer. *Breast Cancer Res* **2008,** *10* (3), R45.

58. Schuerenberg, M.; Luebbert, C.; Deininger, S. O.; Ketterlinus, R.; Suckau, D., MALDI tissue imaging: mass spectrometric localization of biomarkers in tissue slices. *Nature Methods* **2007,** *4* (5), iii-iv.

59. Zhang, H.; Wu, G.; Tu, H.; Huang, F., Discovery of serum biomarkers in astrocytoma by SELDI–TOF MS and proteinchip technology. *Journal of Neuro-Oncology* **2007,** *84* (3), 315-323.

60. Ilyin, S. E.; Belkowski, S. M.; Plata-Salamán, C. R., Biomarker discovery and validation: technologies and integrative approaches. *Trends in Biotechnology* **2004,** *22* (8), 411-416.

61. *MALDI MS: A Practical Guide to Instrumentation, Methods and Applications*. Weily-VCH: Munster Germany, 2007.

62. ProteomeDigest The Internal Standard.
http://www.ionsource.com/tutorial/msquan/is.htm (accessed 10/6/2010).

63. MacDougall, D.; Crummett, W. B., Guidelines for data acquisition and data quality evaluation in environmental chemistry. *Analytical Chemistry* **1980,** *52* (14), 2242-2249.

64. Armbruster, D.; Tillman, M.; Hubbs, L., Limit of detection (LQD)/limit of quantitation (LOQ): comparison of the empirical and the statistical methods exemplified with GC-MS assays of abused drugs. *Clin Chem* **1994,** *40* (7), 1233-1238.

65. Aravagiri, M.; Teper, Y.; Marder, S. R., Pharmacokinetics and tissue distribution of olanzapine in rats. John Wiley & Sons, Ltd.: 1999; Vol. 20, pp 369-377.

66. Bogusz, M. J.; Krüger, K. D.; Maier, R. D.; Erkwoh, R.; Tuchtenhagen, F., Monitoring of olanzapine in serum by liquid chromatography-atmospheric pressure chemical ionization mass spectrometry. *Journal of Chromatography B: Biomedical Sciences and Applications* **1999,** *732* (2), 257-269.

67. Bao, J.; Potts, B. D., Quantitative determination of olanzapine in rat brain tissue by high-performance liquid chromatography with electrochemical detection. *Journal of Chromatography B: Biomedical Sciences and Applications* **2001,** *752* (1), 61-67.

68. Central Brain Tumor Registry of the United States. Statistical report: primary brain tumors in the United States, 2000-2004. http://www.cbtrus.org/reports//2007-2008/2007report.pdf (accessed September 26, 2010).

69. Wen, P. Y.; Kesari, S., Malignant Gliomas in Adults. *New England Journal of Medicine* **2008,** *359* (5), 492-507.

70. Croom, K. F.; Perry, C. M., Imatinib Mesylate: In the Treatment of Gastrointestinal Stromal Tumours. *Drugs* **2003,** *63* (5), 513-522.

71. Druker, B. J., Perspectives on the development of a molecularly targeted agent. *Cancer Cell* **2002,** *1* (1), 31-36.

72. DiRocco, F.; Carroll, R. S.; Zhang, J.; Black, P., Platelet-derived Growth Factor and Its Receptor Expression in Human Oligodendrogliomas. *Neurosurgery* **1998,** *42* (2), 341-346.

73. Deuel, T. F.; Huang, J. S., Platelet-derived growth factor. Structure, function, and roles in normal and transformed cells. *The Journal of Clinical Investigation* **1984,** *74* (3), 669-676.

74. Hermanson, M.; Funa, K.; Hartman, M.; Claesson-Welsh, L.; Heldin, C.-H.; Westermark, B.; Nister, M., Platelet-derived Growth Factor and Its Receptors in Human Glioma Tissue: Expression of Messenger RNA and Protein Suggests the Presence of Autocrine and Paracrine Loops. *Cancer Research* **1992,** *52* (11), 3213-3219.

75. Lokker, N. A.; Sullivan, C. M.; Hollenbach, S. J.; Israel, M. A.; Giese, N. A., Platelet-derived Growth Factor (PDGF) Autocrine Signaling Regulates Survival and Mitogenic Pathways in Glioblastoma Cells. *Cancer Research* **2002,** *62* (13), 3729-3735.

76. Kilic, T.; Alberta, J. A.; Zdunek, P. R.; Acar, M.; Iannarelli, P.; Oâ€™Reilly, T.; Buchdunger, E.; Black, P. M.; Stiles, C. D., Intracranial Inhibition of Platelet-derived Growth Factor-mediated Glioblastoma Cell Growth by an Orally Active Kinase Inhibitor of the 2-Phenylaminopyrimidine Class. *Cancer Research* **2000,** *60* (18), 5143-5150.

77. Hagerstrand, D.; Hesselager, G.; Achterberg, S.; Wickenberg Bolin, U.; Kowanetz, M.; Kastemar, M.; Heldin, C. H.; Isaksson, A.; Nister, M.; Ostman, A., Characterization of an imatinib-sensitive subset of high-grade human glioma cultures. *Oncogene* **2006,** *25* (35), 4913-4922.

78. Cao, R.; Rakenhielm, E.; Li, X.; Pietras, K.; Widenfalk, J.; Ostman, A.; Eriksson, U.; Cao, Y., Angiogenesis stimulated by PDGF-CC, a novel member in the PDGF family, involves activation of PDGFR-{alpha}{alpha} and -{alpha}{beta} receptors. *FASEB J.* **2002,** *16* (12), 1575-1583.

79. Geng, L.; Shinohara, E. T.; Kim, D.; Tan, J.; Osusky, K.; Shyr, Y.; Hallahan, D. E., STI571 (Gleevec) improves tumor growth delay and survival in irradiated mouse models of glioblastoma. *Int J Radiat Oncol Biol Phys* **2006,** *64* (1), 263-71.

80. United States Department of Agriculture, Transportation, Sale and Handling of Certain Animals. . AAPHI, Ed. 2010.

81. Online Ethics Center for Engineering and Research, The Ethics of Using Animals in Research. http://www.onlineethics.org/CMS/2963/modindex/animalres.aspx (accessed September 26, 2010).

82. OLAW Applied Research Ethics National Association, Institutional Animal Care and Use Committee Guidebook. Pitts, M., Ed. 1992. http://grants.nih.gov/grants/olaw/GuideBook.pdf.

83. *Handbook of Laboratory Animal Science, Second Edition*. CRC Press LLC: 2003; Vol. II.

84. Candolfi, M.; Curtin, J.; King, G. D.; Pluhar, E.; McNiel, E.; Ohlfest, J. R.; Freese, A. B.; Moore, P. F.; Nichols, S. W.; Lowenstein, P. R.; Castro, M. G., Glioblastoma multiforme (GBM): a comparative histological analysis of gliomas in mice, rats, dogs and humans. *AACR Meeting Abstracts* **2006,** *2006* (1), 642.

85. Kamphorst, W.; deBoer, A. G.; Gaillard, P. J., *Brain Drug Targeting: The Future of Brain Drug Development*. University Press: Cambridge, 2001.

86. Denysenko, T.; Gennero, L.; Roos, M. A.; Melcarne, A.; Juenemann, C.; Faccani, G.; Morra, I.; Cavallo, G.; Reguzzi, S.; Pescarmona, G.; Ponzetto, A., Glioblastoma cancer stem cells: heterogeneity, microenvironment and related therapeutic strategies. John Wiley & Sons, Ltd.: Vol. 28, pp 343-351.

87. Inda, M. D.; Bonavia, R.; Mukasa, A.; Narita, Y.; Sah, D. W. Y.; Vandenberg, S.; Brennan, C.; Johns, T. G.; Bachoo, R.; Hadwiger, P.; Tan, P.; DePinho, R. A.; Cavenee, W.; Furnari, F., Tumor heterogeneity is an active process maintained by a mutant EGFR-induced cytokine circuit in glioblastoma. *Genes Dev. 24* (16), 1731-1745.

88. Park, D. M.; Rich, J. N., Biology of glioma cancer stem cells. *Mol. Cells* **2009,** *28* (1), 7-12.

89. Teoh, M.; Narayanan, P.; Moo, K.; Radhakrisman, S.; Pillappan, R.; Bukhari, N.; Segarra, I., HPLC Determination Of Imatinib In Plasma And Tissues After Multiple Oral DoseAdministration To Mice. *Pakistan Journal of Pharmaceutical Sciences* **2010,** *23* (1), 35-41.

90. Parise, R. A.; Ramanathan, R. K.; Hayes, M. J.; Egorin, M. J., Liquid chromatographic-mass spectrometric assay for quantitation of imatinib and its main metabolite (CGP 74588) in plasma. *Journal of Chromatography B* **2003,** *791* (1-2), 39-44.

91. Tusher, V. G.; Tibshirani, R.; Chu, G., Significance analysis of microarrays applied to the ionizing radiation response. *Proceedings of the National Academy of Sciences* **2001,** *98* (9), 5116-5121.

92. Asotra, K.; Ningaraj, N.; Black, K., The Blood-Brain Barrier: Measurement of Blood-Brain and Blood-Tumor Barrier Permeabilities with [14C]-Labeled Tracers. *Methods in Molecular Medicine* **2003,** *89* (11), 177-190.

93. Lockman, P. R.; Mittapalli, R. K.; Taskar, K. S.; Rudraraju, V.; Gril, B.; Bohn, K. A.; Adkins, C. E.; Roberts, A.; Thorsheim, H. R.; Gaasch, J. A.; Huang, S.; Palmieri, D.; Steeg, P. S.; Smith, Q. R., Heterogeneous Bloodâ€"Tumor Barrier Permeability Determines Drug Efficacy in Experimental Brain Metastases of Breast Cancer. *Clinical Cancer Research 16* (23), 5664-5678.

94. Stewart, D. J., A critique of the role of the blood-brain barrier in the chemotherapy of human brain tumors. *Journal of Neuro-Oncology* **1994,** *20* (2), 121-139.

95. Holdhoff, M.; Supko, J.; Gallia, G.; Hann, C.; Bonekamp, D.; Ye, X.; Cao, B.; Olivi, A.; Grossman, S., Intratumoral concentrations of imatinib after oral administration in patients with glioblastoma multiforme. *Journal of Neuro-Oncology 97* (2), 241-245.

96. Gschwind, H.-P.; Pfaar, U.; Waldmeier, F.; Zollinger, M.; Sayer, C.; Zbinden, P.; Hayes, M.; Pokorny, R.; Seiberling, M.; Ben-Am, M.; Peng, B.; Gross, G., METABOLISM AND DISPOSITION OF IMATINIB MESYLATE IN HEALTHY VOLUNTEERS. *Drug Metabolism and Disposition* **2005,** *33* (10), 1503-1512.

97. Van Erp, N. P.; Gelderblom, H.; Guchelaar, H.-J., Clinical pharmacokinetics of tyrosine kinase inhibitors. *Cancer Treatment Reviews* **2009,** *35* (8), 692-706.

98. Kramer, T., Side Effects and Therapeutic Effects: Half-life and Steady State. *Medscape General Medicine* **2003,** *5* (1).

99. Landriscina, M.; Maddalena, F.; Laudiero, G.; Esposito, F., Adaptation to Oxidative Stress, Chemoresistance, and Cell Survival. *Antioxid. Redox Signal.* **2009,** *11* (11), 2701-2716.

100. Voet, D.; Voet, J. G., *Biochemistry, Second Edition*. John Wiley & Sons, Inc: New York, 1995.

101. Chakravarti, A.; Chakladar, A.; Delaney, M. A.; Latham, D. E.; Loeffler, J. S., The Epidermal Growth Factor Receptor Pathway Mediates Resistance to Sequential Administration of Radiation and Chemotherapy in Primary Human Glioblastoma Cells in a RAS-dependent Manner. *Cancer Research* **2002,** *62* (15), 4307-4315.

102. Servidei, T.; Riccardi, A.; Sanguinetti, M.; Dominici, C.; Riccardi, R., Increased sensitivity to the platelet-derived growth factor (PDGF) receptor inhibitor STI571 in chemoresistant glioma cells is associated with enhanced PDGF-BB-mediated signaling and STI571-induced Akt inactivation. Wiley Subscription Services, Inc., A Wiley Company: 2006; Vol. 208, pp 220-228.

103. Ziegler, D. S.; Wright, R. D.; Kesari, S.; Lemieux, M. E.; Tran, M. A.; Jain, M.; Zawel, L.; Kung, A. L., Resistance of human glioblastoma multiforme cells to growth factor inhibitors is overcome by blockade of inhibitor of apoptosis proteins. *The Journal of Clinical Investigation* **2008,** *118* (9), 3109-3122.

104. Oliva, C. R.; Nozell, S. E.; Diers, A.; McClugage, S. G.; Sarkaria, J. N.; Markert, J. M.; Darley-Usmar, V. M.; Bailey, S. M.; Gillespie, G. Y.; Landar, A.; Griguer, C. E., Acquisition of Temozolomide Chemoresistance in Gliomas Leads to Remodeling of Mitochondrial Electron Transport Chain. *J. Biol. Chem. 285* (51), 39759-39767.

105. Kennedy, F. G.; Jones, D. P., Oxygen Dependence of Mitochondrial-Function in Isolated Rat Cardiac Myocytes. *American Journal of Physiology* **1986,** *250* (3), C374-C383.

106. Villani, G.; Greco, M.; Papa, S.; Attardi, G., Low Reserve of Cytochrome c Oxidase Capacity in Vivo in the Respiratory Chain of a Variety of Human Cell Types. *J. Biol. Chem.* **1998,** *273* (48), 31829-31836.

107. Brozzi, F.; Arcuri, C.; Giambanco, I.; Donato, R., S100B Protein Regulates Astrocyte Shape and Migration via Interaction with Src Kinase: Implications for Astrocyte Development, Activation and Tumor Growth *J. Biol. Chem.* **2009,** *284* (13), 8788-8802.

108. Vos, M. J.; Postma, T. J.; Martens, F.; Uitdehaag, B. M. J.; Blankenstein, M. A.; Vandertop, W. P.; Slotman, B. J.; Heimans, J. J., Serum Levels of S-100B Protein and

Neuron-specific Enolase in Glioma Patients: A Pilot Study. *Anticancer Research* **2004,** *24* (4), 2511-2514.

109. Selinfreund, R. H.; Barger, S. W.; Welsh, M. J.; Van Eldik, L. J., Antisense inhibition of glial S100 beta production results in alterations in cell morphology, cytoskeletal organization, and cell proliferation. *The Journal of Cell Biology* **1990,** *111* (5), 2021-2028.

110. George, J. M., The synucleins. *Genome Biology* **2001,** *3* (1).

111. Liu, H.; Liu, W.; Wu, Y.; Zhou, Y.; Xue, R.; Luo, C.; Wang, L.; Zhao, W.; Jiang, J.-D.; Liu, J., Loss of Epigenetic Control of Synuclein-Î³ Gene as a Molecular Indicator of Metastasis in a Wide Range of Human Cancers. *Cancer Research* **2005,** *65* (17), 7635-7643.

112. Crews, L.; Tsigelny, I.; Hashimoto, M.; Masliah, E., Role of Synucleins in Alzheimer's Disease. *Neurotox. Res.* **2009,** *16* (3), 306-317.

113. Fung, K.-M.; Rorke, L. B.; Giasson, B.; Lee, V. M. Y.; Trojanowski, J. Q., Expression of a-, ß-, and gamma-synuclein in glial tumors and medulloblastomas. *Acta Neuropathologica* **2003,** *106* (2), 167-175.

114. Surguchov, A., Focus on Molecules: The synucleins: "When friends become foes". *Experimental Eye Research* **2008,** *86* (1), 1-2.

115. Maniatis, T.; Reed, R., The role of small nuclear ribonucleoprotein particles in pre-mRNA splicing. *Nature* **1987,** *325* (6106), 673-678.

116. Cheung, H.; Baggerly, K.; Tsavachidis, S.; Bachinski, L.; Neubauer, V.; Nixon, T.; Aldape, K.; Cote, G.; Krahe, R., Global analysis of aberrant pre-mRNA splicing in glioblastoma using exon expression arrays. *BMC Genomics* **2008,** *9* (1), 216.

117. Kasai, T.; Inoue, M.; Koshiba, S.; Yabuki, T.; Aoki, M.; Nunokawa, E.; Seki, E.; Matsuda, T.; Matsuda, N.; Tomo, Y.; Shirouzu, M.; Terada, T.; Obayashi, N.; Hamana, H.; Shinya, N.; Tatsuguchi, A.; Yasuda, S.; Yoshida, M.; Hirota, H.; Matsuo, Y.; Tani, K.; Suzuki, H.; Arakawa, T.; Carninci, P.; Kawai, J.; Hayashizaki, Y.; Kigawa, T.; Yokoyama, S., Solution structure of a BolA-like protein from Mus musculus. Cold Spring Harbor Laboratory Press: 2004; Vol. 13, pp 545-548.

118. Burton, M.; Rose, T. M.; Faergeman, N. J.; Knudsen, J., Evolution of the acyl-CoA binding protein (ACBP). *Biochem. J.* **2005,** *392*, 299-307.

119. Coté, R. J., *Aseptic Technique for Cell Culture*. John Wiley & Sons, Inc.: 2001.

120. Norris, J. L.; Cornett, D. S.; Mobley, J. A.; Andersson, M.; Seeley, E. H.; Chaurand, P.; Caprioli, R. M., Processing MALDI mass spectra to improve mass spectral

direct tissue analysis. *International Journal of Mass Spectrometry* **2007,** *260* (2-3), 212-221.

121. Clement, V.; Sanchez, P.; de Tribolet, N.; Radovanovic, I.; Ruiz i Altaba, A., HEDGEHOG-GLI1 Signaling Regulates Human Glioma Growth, Cancer Stem Cell Self-Renewal, and Tumorigenicity. *Current biology : CB* **2007,** *17* (2), 165-172.

122. Ruiz i Altaba, A.; Sanchez, P.; Dahmane, N., Gli and hedgehog in cancer: tumours, embryos and stem cells. *Nat Rev Cancer* **2002,** *2* (5), 361-372.

123. Jessell, T. M., Neuronal specification in the spinal cord: inductive signals and transcriptional codes. *Nat Rev Genet* **2000,** *1* (1), 20-29.

124. Ruiz i Altaba, A.; Palma, V.; Dahmane, N., Hedgehog-GLI signaling and the growth of the brain. *Nat Rev Neurosci* **2002,** *3* (1), 24-33.

125. Ruiz i Altaba, A.; Stecca, B.; Sánchez, P., Hedgehog-Gli signaling in brain tumors: stem cells and paradevelopmental programs in cancer. *Cancer Letters* **2004,** *204* (2), 145-157.

126. Xu, Q.; Yuan, X.; Liu, G.; Black, K. L.; Yu, J. S., Hedgehog Signaling Regulates Brain Tumor-Initiating Cell Proliferation and Portends Shorter Survival for Patients with PTEN-Coexpressing Glioblastomas. John Wiley & Sons, Ltd.: 2008; Vol. 26, pp 3018-3026.

127. Becher, O. J.; Hambardzumyan, D.; Fomchenko, E. I.; Momota, H.; Mainwaring, L.; Bleau, A.-M.; Katz, A. M.; Edgar, M.; Kenney, A. M.; Cordon-Cardo, C.; Blasberg, R. G.; Holland, E. C., Gli Activity Correlates with Tumor Grade in Platelet-Derived Growth Factor-Induced Gliomas. *Cancer Res* **2008,** *68* (7), 2241-2249.

128. Wang, k.; Pan, L.; Che, X.; Cui, D.; Li, C., Sonic Hedgehog/GLI1 signaling pathway inhibition restricts cell migration and invasion in human gliomas. *Neurological Research* **2010,** *32* (9), 975-980.

129. Wang, K.; Pan, L.; Che, X.; Cui, D.; Li, C., Gli1 inhibition induces cell-cycle arrest and enhanced apoptosis in brain glioma cell lines. *Journal of Neuro-Oncology* **2010,** *98* (3), 319-327.

130. Sarangi, A.; Valadez, J. G.; Rush, S.; Abel, T. W.; Thompson, R. C.; Cooper, M. K., Targeted inhibition of the Hedgehog pathway in established malignant glioma xenografts enhances survival. *Oncogene* **2009,** *28* (39), 3468-3476.

131. Bar, E. E.; Chaudhry, A.; Lin, A.; Fan, X.; Schreck, K.; Matsui, W.; Piccirillo, S.; Vescovi, A. L.; DiMeco, F.; Olivi, A.; Eberhart, C. G., Cyclopamine-Mediated Hedgehog Pathway Inhibition Depletes Stem-Like Cancer Cells in Glioblastoma. John Wiley & Sons, Ltd.: 2007; Vol. 25, pp 2524-2533.

132. UCDavis Mouse in Science Cancer Research. http://www.vetmed.ucdavis.edu/Animal_alternatives/cancer.htm (accessed September 26, 2010).

133. Candolfi, M.; Curtin, J.; Nichols, W.; Muhammad, A. K. M.; King, G.; Pluhar, G.; McNiel, E.; Ohlfest, J.; Freese, A.; Moore, P.; Lerner, J.; Lowenstein, P.; Castro, M., Intracranial glioblastoma models in preclinical neuro-oncology: neuropathological characterization and tumor progression. *Journal of Neuro-Oncology* **2007,** *85* (2), 133-148.

134. Zheng, X.; Cui, X.-X.; Avila, G. E.; Huang, M.-T.; Liu, Y.; Patel, J.; Kong, A. N. T.; Paulino, R.; Shih, W. J.; Lin, Y.; Rabson, A. B.; Reddy, B. S.; Conney, A. H., Atorvastatin and Celecoxib Inhibit Prostate PC-3 Tumors in Immunodeficient Mice. *Clinical Cancer Research* **2007,** *13* (18), 5480-5487.

135. Heikkila, J. E.; Vaha-Koskela, M. J. V.; Ruotsalainen, J. J.; Martikainen, M. W.; Stanford, M. M.; McCart, J. A.; Bell, J. C.; Hinkkanen, A. E., Intravenously Administered Alphavirus Vector VA7 Eradicates Orthotopic Human Glioma Xenografts in Nude Mice. *PLoS ONE 5* (1), e8603.

136. Niclou, S. P.; Danzeisen, C.; Eikesdal, H. P.; Wiig, H.; Brons, N. H. C.; Poli, A. M. F.; Svendsen, A.; Torsvik, A.; Enger, P. O.; Terzis, J. A.; Bjerkvig, R., A novel eGFP-expressing immunodeficient mouse model to study tumor-host interactions. *FASEB J.* **2008,** *22* (9), 3120-3128.

137. O/'Brien, C. A.; Pollett, A.; Gallinger, S.; Dick, J. E., A human colon cancer cell capable of initiating tumour growth in immunodeficient mice. *Nature* **2007,** *445* (7123), 106-110.

138. Charafe-Jauffret, E.; Ginestier, C.; Birnbaum, D., Breast cancer stem cells: tools and models to rely on. *BMC Cancer* **2009,** *9* (1), 202.

139. Yang, Z. F.; Ho, D. W.; Ng, M. N.; Lau, C. K.; Yu, W. C.; Ngai, P.; Chu, P. W. K.; Lam, C. T.; Poon, R. T. P.; Fan, S. T., Significance of CD90+ Cancer Stem Cells in Human Liver Cancer. *Cancer Cell* **2008,** *13* (2), 153-166.

140. Dong, X.; Guan, J.; English, J. C.; Flint, J.; Yee, J.; Evans, K.; Murray, N.; MacAulay, C.; Ng, R. T.; Gout, P. W.; Lam, W. L.; Laskin, J.; Ling, V.; Lam, S.; Wang, Y., Patient-Derived First Generation Xenografts of Nonâ€“Small Cell Lung Cancers: Promising Tools for Predicting Drug Responses for Personalized Chemotherapy. *Clinical Cancer Research 16* (5), 1442-1451.

141. Lee, J.; Kotliarova, S.; Kotliarov, Y.; Li, A.; Su, Q.; Donin, N. M.; Pastorino, S.; Purow, B. W.; Christopher, N.; Zhang, W.; Park, J. K.; Fine, H. A., Tumor stem cells derived from glioblastomas cultured in bFGF and EGF more closely mirror the

phenotype and genotype of primary tumors than do serum-cultured cell lines. *Cancer Cell* **2006,** *9* (5), 391-403.

142. Lipinski, R. J.; Hutson, P. R.; Hannam, P. W.; Nydza, R. J.; Washington, I. M.; Moore, R. W.; Girdaukas, G. G.; Peterson, R. E.; Bushman, W., Dose- and route-dependent teratogenicity, toxicity, and pharmacokinetic profiles of the Hedgehog signaling antagonist cyclopamine in the mouse. *Toxicological Sciences* **2008,** *104* (1), 189-197.

143. Lewis, P. M.; Gritli-Linde, A.; Smeyne, R.; Kottmann, A.; McMahon, A. P., Sonic hedgehog signaling is required for expansion of granule neuron precursors and patterning of the mouse cerebellum. *Developmental Biology* **2004,** *270* (2), 393-410.

144. Fingar, D. C.; Blenis, J., Target of rapamycin (TOR): an integrator of nutrient and growth factor signals and coordinator of cell growth and cell cycle progression. *Oncogene 23* (18), 3151-3171.

145. Sancak, Y.; Bar-Peled, L.; Zoncu, R.; Markhard, A. L.; Nada, S.; Sabatini, D. M., Ragulator-Rag Complex Targets mTORC1 to the Lysosomal Surface and Is Necessary for Its Activation by Amino Acids. *Cell 141* (2), 290-303.

146. Sanchez, P.; Ruiz i Altaba, A., In vivo inhibition of endogenous brain tumors through systemic interference of Hedgehog signaling in mice. *Mechanisms of Development* **2005,** *122* (2), 223-230.

147. Rehman, I.; Azzouzi, A. R.; Cross, S. S.; Deloulme, J. C.; Catto, J. W. F.; Wylde, N.; Larre, S.; Champigneuille, J.; Hamdy, F. C., Dysregulated expression of S100A11 (Calgizzarin) in prostate cancer and precursor lesions. *Hum. Pathol.* **2004,** *35* (11), 1385-1391.

148. Melle, C.; Ernst, G.; Schimmel, B.; Bleul, A.; Mothes, H.; Kaufmann, R.; Settmacher, U.; von Eggeling, F., Different expression of calgizzarin (S100A11) in normal colonic epithelium, adenoma and colorectal carcinoma. *Int. J. Oncol.* **2006,** *28* (1), 195-200.

149. Ohuchida, K.; Mizumoto, K.; Ohhashi, S.; Yamaguchi, H.; Konomi, H.; Nagai, E.; Yamaguchi, K.; Tsuneyoshi, M.; Tanaka, M., S100A11, a putative tumor suppressor gene, is overexpressed in pancreatic carcinogenesis. *Clinical Cancer Research* **2006,** *12* (18), 5417-5422.

150. Liu, X. G.; Wang, X. P.; Li, W. F.; Yang, S.; Zhou, X.; Li, S. J.; Li, X. J.; Hao, D. Y.; Fan, Z. M., Ca2+-binding protein S100A11: A novel diagnostic marker for breast carcinoma. *Oncol. Rep. 23* (5), 1301-1308.

151. Kanamori, T.; Takakura, K.; Mandai, M.; Kariya, M.; Fukuhara, K.; Sakaguchi, M.; Huh, N.-h.; Saito, K.; Sakurai, T.; Fujita, J.; Fujii, S., Increased expression of

calcium-binding protein S100 in human uterine smooth muscle tumours. *Molecular Human Reproduction* **2004,** *10* (10), 735-742.

152. Cecconi, D.; Donadelli, M.; Rinalducci, S.; Zolla, L.; Scupoli, M. T.; Scarpa, A.; Palmieri, M.; Righetti, P. G., Proteomic analysis of pancreatic endocrine tumor cell lines treated with the histone deacetylase inhibitor trichostatin A. Wiley-vch Verlag: 2007; Vol. 7, pp 1644-1653.

153. Turrens, J. F., Mitochondrial formation of reactive oxygen species. *The Journal of Physiology* **2003,** *552* (2), 335-344.

154. Wang, Y.; Fang, J.; Leonard, S. S.; Krishna Rao, K. M., Cadmium inhibits the electron transfer chain and induces Reactive Oxygen Species. *Free Radical Biology and Medicine* **2004,** *36* (11), 1434-1443.

155. McClintock, D. S.; Santore, M. T.; Lee, V. Y.; Brunelle, J.; Budinger, G. R. S.; Zong, W.-X.; Thompson, C. B.; Hay, N.; Chandel, N. S., Bcl-2 Family Members and Functional Electron Transport Chain Regulate Oxygen Deprivation-Induced Cell Death. *Mol. Cell. Biol.* **2002,** *22* (1), 94-104.

156. Chen, Y.; McMillan-Ward, E.; Kong, J.; Israels, S. J.; Gibson, S. B., Mitochondrial electron-transport-chain inhibitors of complexes I and II induce autophagic cell death mediated by reactive oxygen species. *J Cell Sci* **2007,** *120* (23), 4155-4166.

157. Azad, M. B.; Chen, Y.; Gibson, S. B., Regulation of autophagy by reactive oxygen species (ROS): implications for cancer progression and treatment. *Antioxidants & Redox Signaling* **2009,** *11* (4), 777(14).

158. Ruy, F.; Vercesi, A.; Kowaltowski, A., Inhibition of specific electron transport pathways leads to oxidative stress and decreased proliferation. *Journal of Bioenergetics and Biomembranes* **2006,** *38* (2), 129-135.

159. Chen, Y. Q.; Gibson, S. B., Is mitochondrial generation of reactive oxygen species a trigger for autophagy? *Autophagy* **2008,** *4* (2), 246-248.

160. Chen, Y.; Azad, M. B.; Gibson, S. B., Superoxide is the major reactive oxygen species regulating autophagy. *Cell Death Differ.* **2009,** *16* (7), 1040-1052.

161. Welch, K. D.; Panter, K. E.; Lee, S. T.; Gardner, D. R.; Stegelmeier, B. L.; Cook, D., Cyclopamine-induced synophthalmia in sheep: defining a critical window and toxicokinetic evaluation. John Wiley & Sons, Ltd.: 2009; Vol. 29, pp 414-421.

162. Li, H.-Y.; Xu, W.; Li, H.-L.; Zhang, W.-D.; Hu, L.-W., LC-MS-MS Method for the Determination of Protoveratrine A in Rat Plasma. *Chromatographia* **2009,** *69* (5), 523-529.

163. Tremblay, M. R.; Lescarbeau, A.; Grogan, M. J.; Tan, E.; Lin, G.; Austad, B. C.; Yu, L.-C.; Behnke, M. L.; Nair, S. J.; Hagel, M.; White, K.; Conley, J.; Manna, J. D.; Alvarez-Diez, T. M.; Hoyt, J.; Woodward, C. N.; Sydor, J. R.; Pink, M.; MacDougall, J.; Campbell, M. J.; Cushing, J.; Ferguson, J.; Curtis, M. S.; McGovern, K.; Read, M. A.; Palombella, V. J.; Adams, J.; Castro, A. C., Discovery of a Potent and Orally Active Hedgehog Pathway Antagonist (IPI-926). *Journal of Medicinal Chemistry* **2009,** *52* (14), 4400-4418.

164. Rossi, D. T.; Sinz, M. W., *Mass Spectrometry in Drug Discovery*. Marcel Dekker, Inc.: New York, 2002.

165. Contag, P. R., The Development of Biomarkers to Bridge Preclinical and Clinical Studies. *Parma DD* **2006,** *1* (2).